AQUIFER COMPACTION AT DIFFERENT DEPTHS: OBSERVATIONS FROM A VERTICAL GPS ARRAY AT THE UNIVERSITY OF HOUSTON COASTAL CENTER, TEXAS

A Thesis Presented to

the Faculty of the Department of Earth and Atmospheric Sciences

University of Houston

In Partial Fulfillment

of the Requirements for the Degree

Master of Science

By

Dongje Lee

December 2016

AQUIFER COMPACTION AT DIFFERENT DEPTHS: OBSERVATIONS FROM A VERTICAL GPS ARRAY AT THE UNIVERSITY OF HOUSTON COASTAL CENTER, TEXAS

Dongje Lee

APPROVED:

Chairperson Dr. Guoquan Wang

Dr. Alex Robinson

Dr. Hyongki Lee

Dean, College of Natural Sciences and Mathematics

ACKNOWLEDGEMENTS

I would like to express my sincerest gratitude and thanks to multiple people who made this study and thus my graduate career possible. The unwavering patience and unerring guidance of my graduate advisor, Dr. Guoquan Wang, was instrumental to the development and final stages of this conducted project. Specifically, his insistence on using UHC0 as the reference point was well-founded and did not realize the purpose until much later in my study. It is because of this that I am even able to bring this thesis to term at this time.

I would like to thank my labmates who came from varied backgrounds and are now on different paths to their future careers. Special thanks to Timothy "Jak" Kearns, Xueyi Jia, Linqiang Yang, Jiangbo Yu, Xin Zhou, Lin Xiong, Hanlin Liu, Xinxiang Zhu, Jiajun Jiang, Dr. Yan Bao, and Rebecca Neill. In addition, I would like to thank Dr. Hyongki Lee and Dr. Alex Robinson for their patient participation in my thesis committee, with Dr. Wang as chairperson.

I would also like to thank the Harris Galveston Subsidence District for their cooperation and coordination of GPS data gathered and shared for this project. The collective wealth of knowledge, expertise, and experience of everyone involved is what made this study much for successful than it would have been otherwise.

Finally, I am thankful of my wonderful friends and family. To those I may have forgotten to thank that have contributed to my love of this science: Thank You.

Aquifer Compaction at Different Depths: Observations from a Vertical GPS Array at the University of Houston Coastal Center, Texas

---

An Abstract of a Thesis

Presented to

the Faculty of the Department of Earth and Atmospheric Sciences

University of Houston

In Partial Fulfillment

of the Requirements for the Degree

Master of Science

By

Dongje Lee

December 2016

ABSTRACT

Observed GPS data shows that the University of Houston Coastal Center (UHCC) in the La Marque, TX area currently experiences localized subsidence at a steady-surficial rate of 0.5 to 1 cm/year. This study aims to understand the contribution of shallow (<10 m) sediments to the overall subsidence of the study area. GPS data, precipitation data, and groundwater head measurements were collected at the UHCC for two years (02/2014-02/2016). Ground deformation at 10, 20, 30, and 0 feet below the land surface (bls) were measured from four GPS stations and compared to rainfall and groundwater depth. This was done in order to identify possible correlations that may indicate different rates of ground deformation associated with each shallow subsurface layer.

Over the two year observational period at the UHCC, there was an overall vertical lowering trend of 3 to 4 mm/yr of the localized top aquifer, with surficial inflation mitigating this vertical fall to 1 to 2 mm/yr. GPS-weather data comparisons indicated that rainfall of over two centimeters per day can cause abrupt changes in ground layer vertical displacement. Pressure, humidity, and temperature changes of the air were not good indicators of ground movement. GPS-well data comparisons also indicated that about 200 mm of groundwater-level fall is correlated to about 1 mm of vertical drop in the same top aquifer. In general, groundwater movement has been found to dominate ground deformation of the shallow subsurface (<10 m).

Contents

Figures

Tables

1 Introduction

1.1 Subsidence in the Houston-Galveston Area

The University of Houston Coastal Center (UHCC) is a research station located in the La Marque area near Texas City, Texas, directly southeast of Houston and 10 miles northwest and inland from Galveston (Figure 1.1.1) (Coplin and Galloway 1999). The La Marque area is significant in its own right due to the accumulated land subsidence of about 4 meters that has been reported by the U.S. Geological Survey (USGS) in the local area from 1900 to 2001 (Bawden et al. 2012; Kasmarek et al. 2009a).

Subsidence is both a natural- and manmade-gradual lowering of the ground-surface level. It notably occurs where inhabitants and businesses extract fluids, usually groundwater, from aquifers beneath the surface (Galloway et al. 2011; Gabrysch and Bonnet 1975). Generally, these areas are heavily populated urban centers. In the United States, 17,000 square miles (45,000 sq. km.) within 45 states are affected by subsidence. Texas has one of the higher rates of groundwater extraction in the country, withdrawing over 8.5 billion gallons/day (Kenny et al. 2009). An estimated 80% or more of identified subsidence in the United States is consequent to groundwater pumping (Galloway et al. 1999; Coplin and Galloway 1999). In 1991, the National Research Council estimated over $125 million in annual costs nationwide as the result from flooding and structural damage caused by land subsidence.

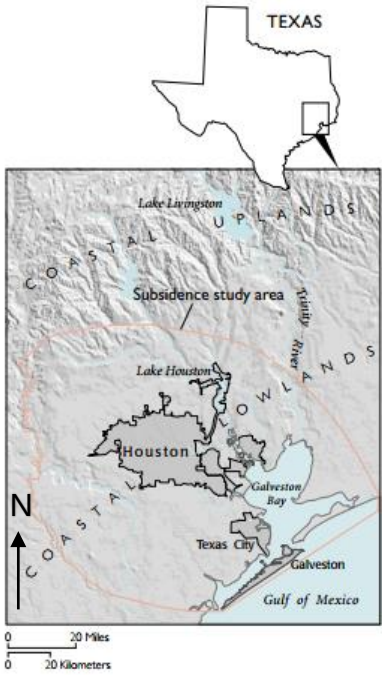

Figure 1.1.1: The Harris-Galveston County Subsidence study area, with Houston city proper, Texas City (in which La Marque is located), and Galveston as bold-bordered (Coplin and Galloway 1999).

Subsidence has both direct and indirect effects on human lives. Directly, subsidence causes damage to the infrastructure; indirectly, it amplifies the damage dealt by other natural disasters and hazards in low-elevation coastal regions such as Harris County and Galveston County (Ortega 2013). The predominant land surface hazard is flooding (Coplin et al. 1999), which becomes more likely with a lowering of the land surface due to differential subsidence across the coastal plain; this subsidence is responsible for blocking natural drainage basins and for impeding runoff dispersal (Galloway et al. 2011).

Historically, the development of the Houston-Galveston area began in the middle of the 19th century. The inauguration of the Houston Ship Channel in 1915 resulted in large-scale urban and industrial development along the ship channel

and nearby areas in the following decades. The industrial facilities were mostly located in Baytown, La Porte, Pasadena, downtown Houston, and Texas City—last of which is adjacent to La Marque, the focus area of this study. Groundwater was the primary source of water for industrial and civilian use in the early 1920s through the 1970s (Kearns et al. 2015).

A need for conducted studies was apparent early in the 20th century. Subsidence in the Houston area was first reported at the Goose Creek oil field by Pratt and Johnson (1926). According to a subsidence investigation conducted in (Holzer and Bluntzer 1984) that studied 29 oil and gas fields in the Houston area, local-land subsidence related to petroleum withdrawal was considered small. High petroleum production did not yield increased subsidence at most oil fields (Kearns et al. 2015). A 2014 study by Yu et al. indicated that compaction in the Houston area is limited to shallow sediments within 600 m below the land surface, wherein all of the Chicot aquifer and a portion of the Evangeline aquifer fall within that depth (Kearns et al. 2015). The USGS reported that from 1943 to 1977, groundwater withdrawals in the Houston-Galveston area caused a 76 m decline of the Chicot water level and a 91 m decline of the Evangeline water table (Gabrysch 1984a). The excessive withdrawals of groundwater created rapid, regional subsidence along the Houston Ship Channel. By the mid-70's, more than two meters of subsidence occurred along the Ship Channel (Coplin and Galloway 1999).

The growing awareness of groundwater pumping and problems related to subsidence compelled local bodies of government to enact legal prohibitions

against excessive groundwater extraction. The Texas State Legislature established the Houston Galveston Subsidence District (HGSD) in 1975 to regulate groundwater withdrawal in the eponymous region (Kearns et al. 2015). The HGSD was given the authorization of issuing (or refusing) well permits to businesses to promote water conservation and education, and also industrial conversion from the use of ground water to surface water (HGSD 1999 2013). To steward groundwater resources and lessen subsidence hazards in counties surrounding the HGSD jurisprudence, the Texas State Legislature established the Fort Bend Subsidence District (FBSD 2013) in 1989 and two groundwater conservation districts: the Lone Star Groundwater Conservation District (LSGCD 2003) and the Brazoria County Groundwater Conservation District (BCGCD 2012), in 2001 and 2003, respectively. The purpose of the LSGCD is to conserve, protect, and enhance the groundwater resources of Montgomery County (LSGCD 2003).

Figure 1.1.2 shows a comprehensive map with locations of GPS and borehole extensometers used outside of this study (Yu et al. 2014). Within this large observational area, subsidence rates have already been catalogued and mapped (Figure 1.1.3) (Yu et al. 2014). The La Marque focus area lies near stations TXLM and PA34, south of NASA and northwest of Galveston in the town of La Marque near Texas City. The scope of this study is limited to UHCC, but takes into account the context of nearby stations' geoscientific information.

Most of the relatively "rapid" subsidence of the La Marque area was observed at two stations, PA34 and TXLM (Figure 1.1.3), with data taken from

2005.0 to 2012.99, which are in decimal years. The overall subsidence rates of PA34 at 11 mm/year and of TXLM at 5 mm/year (Figure 1.1.4) left and right, respectively) are noticeably more rapid than with other nearby stations; for exam-

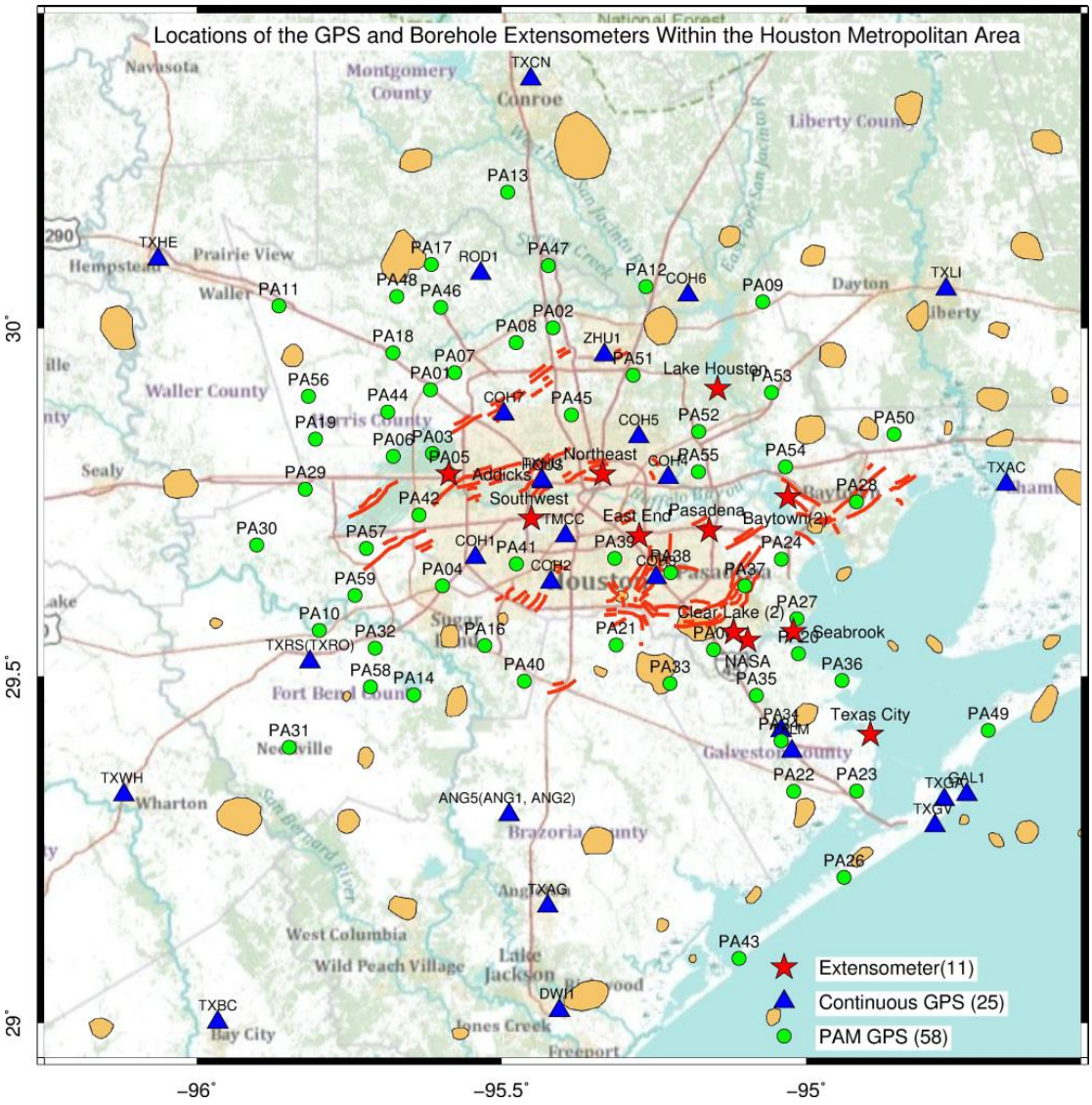

Figure 1.1.2: Map with locations of GPS and borehole extensometers used outside of this study (Yu et al. 2014). Red lines symbolize 150 principle faults mapped by the USGS (Shah & Lanning-Rush 2005). Orange blotches indicate salt domes (AAPG 2011).

ple, PA28, PA20, PA23, and PA26 (Fig 1.1.5) consistently did not show considerable vertical displacements.

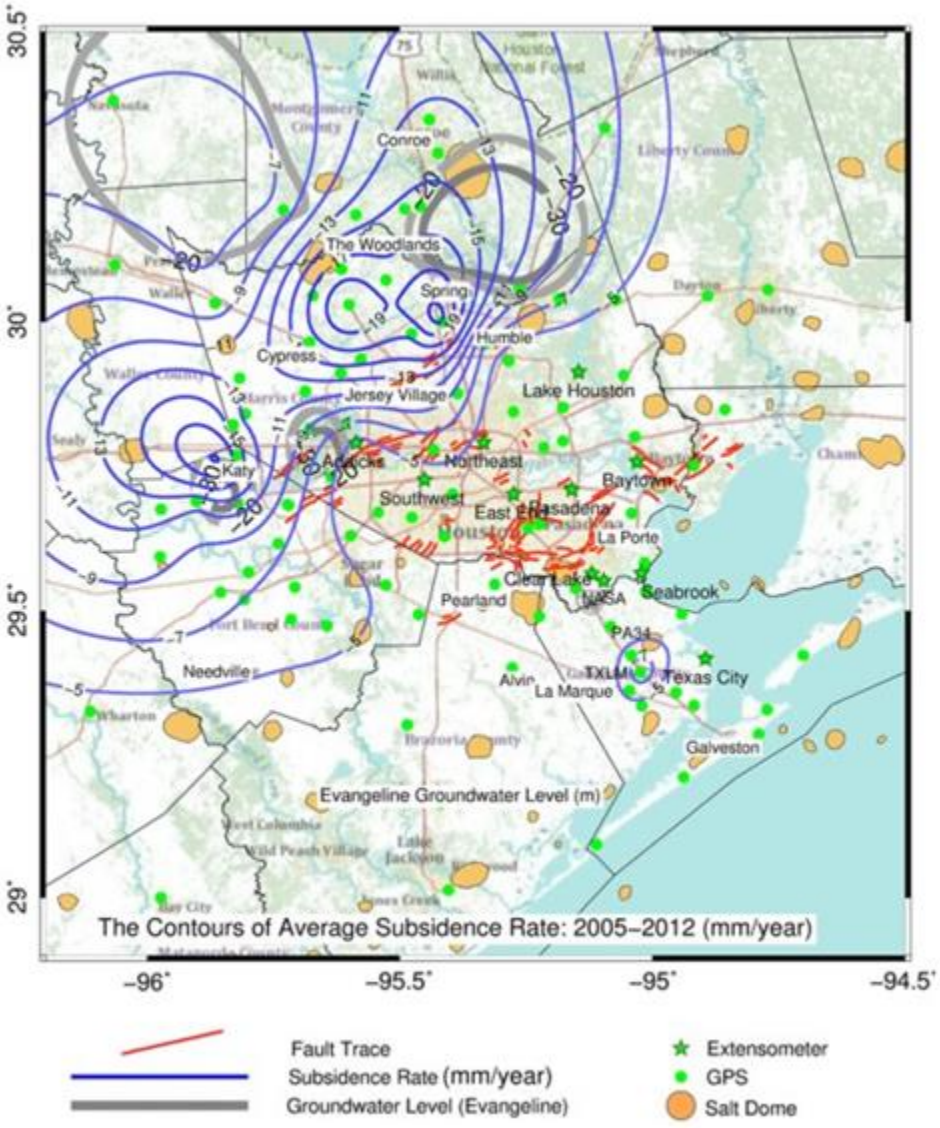

Figure 1.1.3: Contour map of the average subsidence rate in the Houston-Galveston County area, 2005 - 2012; contour labels are measured in mm/yr (Yu et al. 2014).

Subsidence has logistical and pecuniary threats as well. The financial losses related to subsidence are difficult to track in general because identifying

and mapping the affected areas and establishing causality linked to subsidence have proven difficult (Kearns et al. 2015). Subsidence may be considered a “silent hazard” since its damage goes unnoticed until an extensive area is affected and considerable ancillary hazards have been found. Quantifying the damage indirectly related to subsidence is also difficult, such as that caused by flooding and aquifer storage decrease, both of which substantially impact human habitation of an affected area.

Fortunately, anthropogenic countermeasures have been moderately effective. Land subsidence has begun to cease and has slowed considerably in a large part of southeast Harris County and Galveston County due to the strict groundwater control policy implemented by the Harris and Galveston Subsidence District (HGSD) over the last forty years (Wang et al. 2013). However, a localized subsidence bowl within the La Marque area has been observed in GPS data in this area, experiencing 0.5 to 1 cm per year of steady subsidence (Figure 1.1.6) (Kearns et al. 2015).

Currently, no significant subsidence is occurring in this area because groundwater levels are close to the preconsolidation head (about -20 to -30 m) in this region. Four contour maps of the areal subsidence districts outlining the Chicot aquifer and its underlying sister aquifer, the Evangeline, are shown (Figure 1.1.7) (Wang et al. 2015). The top pair shows absolute (negative) altitudes of groundwater levels, where near the southeastern coastal area the water levels can be seen to be above -35 m. At the bottom two graphs of Figure

5.1.4, a general increase of the groundwater level height can be seen in the study area near Galveston.

The experience of the HGSD in regulating land subsidence in the southeastern region of the Houston metropolitan area has shown that water head levels rise very slowly (Kearns et al. 2015). For instance, it took around 30 years (1975–2005) for groundwater heads to recover to preconsolidation levels and for subsidence to cease at Seabrook, Pasadena, Clear Lake, and Baytown.

Sites showing horizontal ground positional velocities of more than 5 mm/yr were mostly caused by horizontal displacements unrelated to fault movement. Fault traces which cross subsidence contours of the area exhibit no apparent control of the former over the latter. As noted earlier, deep-seated subsidence is unlikely to be the case in the Harris-Galveston county area (Yu et al. 2014), and thusly this study aimed to fill the niche for studying shallow, *depth-varying* subsidence in this location.

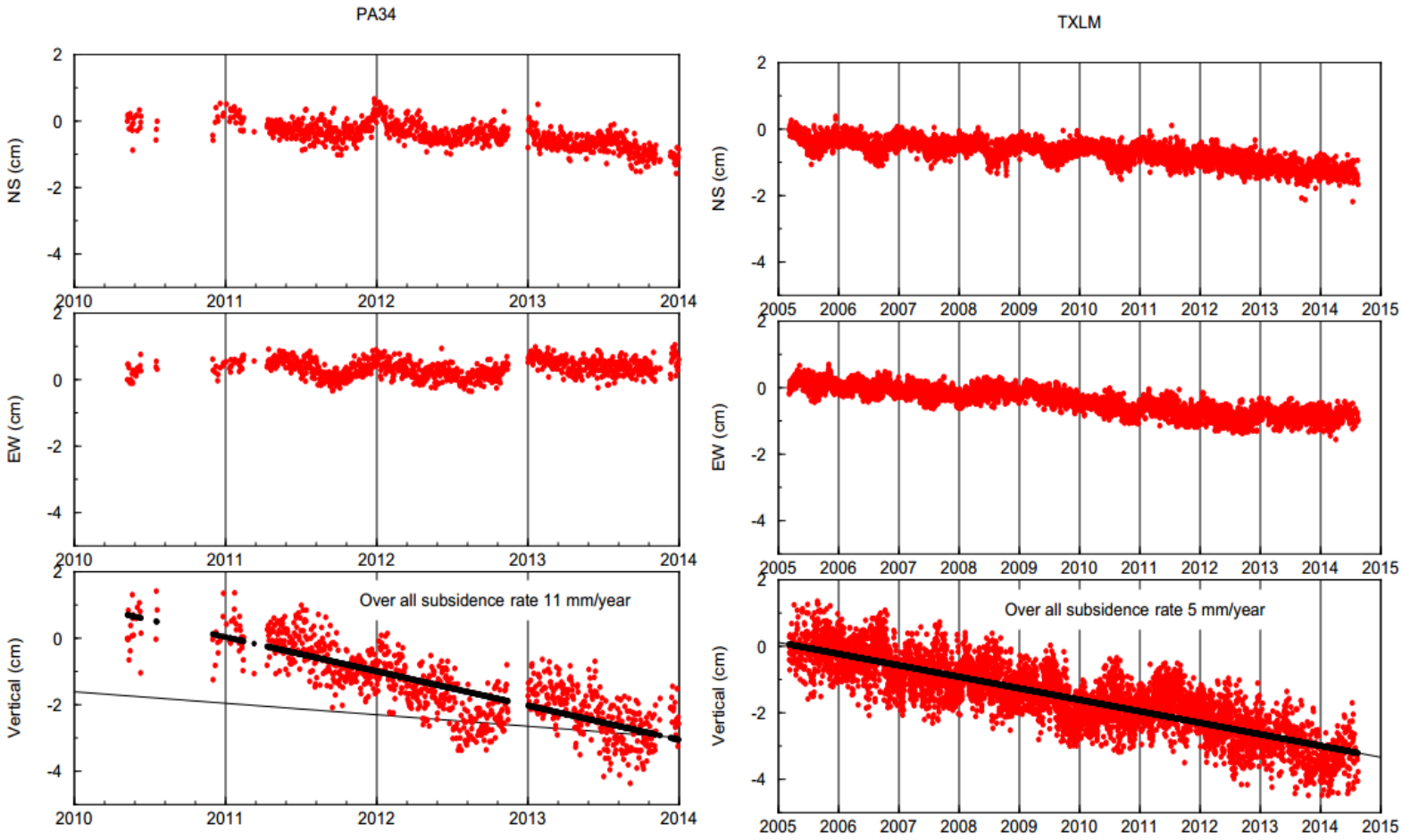

Figure 1.1.4: (left) PA34 station's northing (NS), easting (EW), and height (Vertical) displacements over the 2010-2014 4-year period of measurement (Yu et al. 2014). The vertical subsidence trend showed a consistent 11 mm/yr rate. (right) TXLM station's northing, easting, and height displacements over a 10 year span, 2005-2015. The consistent vertical subsidence rate was 5 mm/yr.

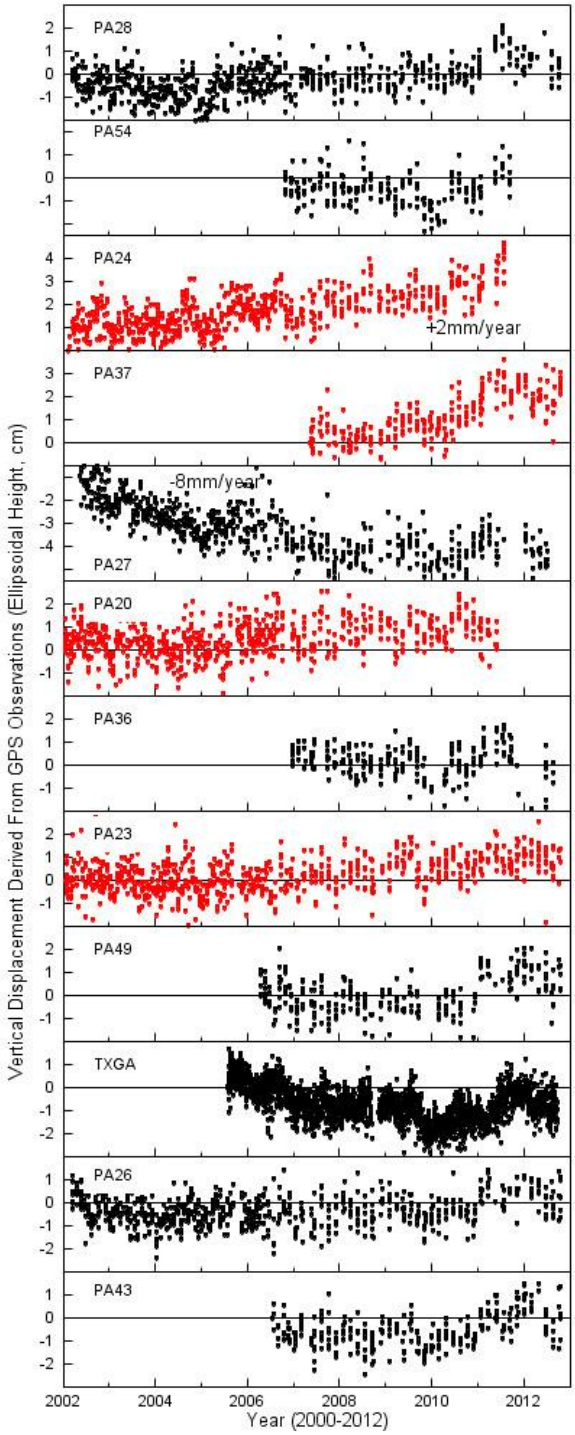

Figure 1.1.5: The height displacement time series, from 2002 to 2012, of 12 GPS stations along the Houston Ship Channel and the coastal areas of Galveston (Yu et al. 2014). Note that PA28, PA20, PA23, and PA26 consistently show negligible vertical displacements.

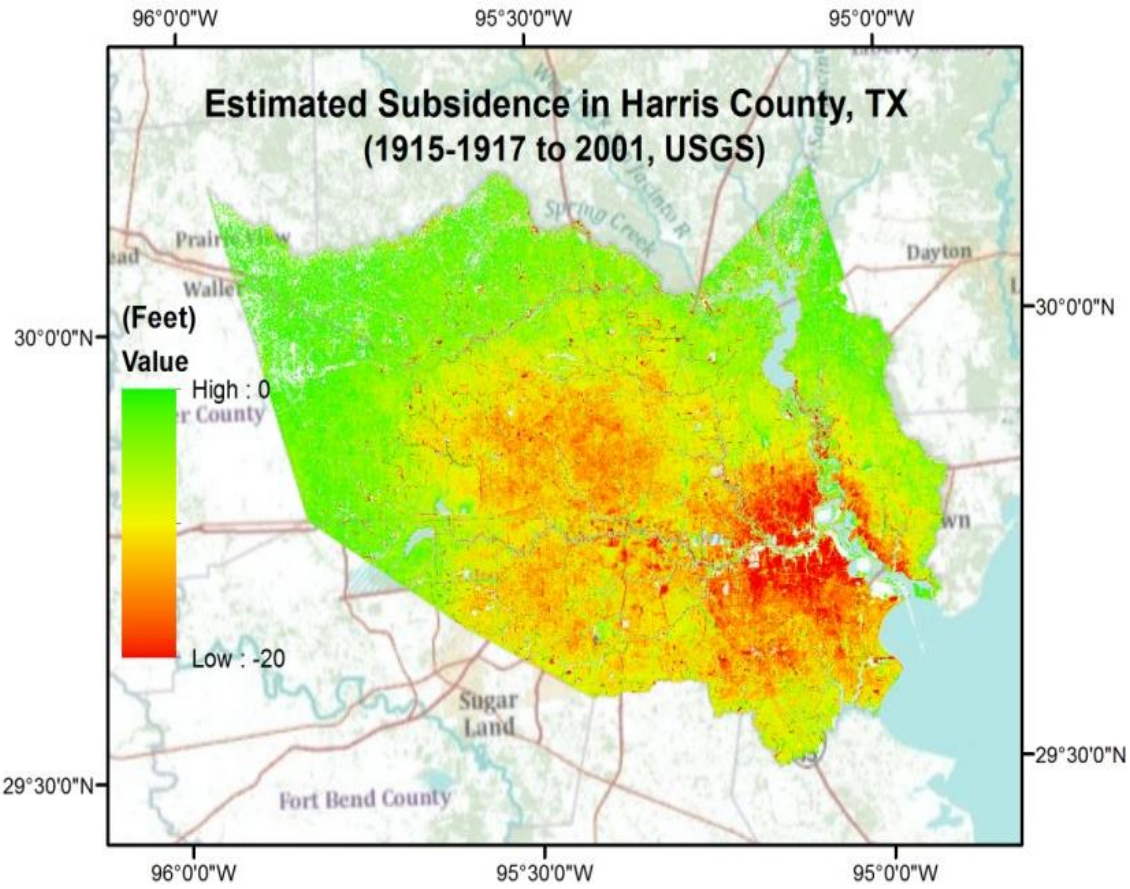

Figure 1.1.6: Long-term subsidence (1915–2001) in the Harris-Galveston region, mapped by the USGS (Kasmarek et al. 2009a). Color-mapped measurements were created from 1915 to 1917 land-surface elevation data and 2001 LiDAR data.

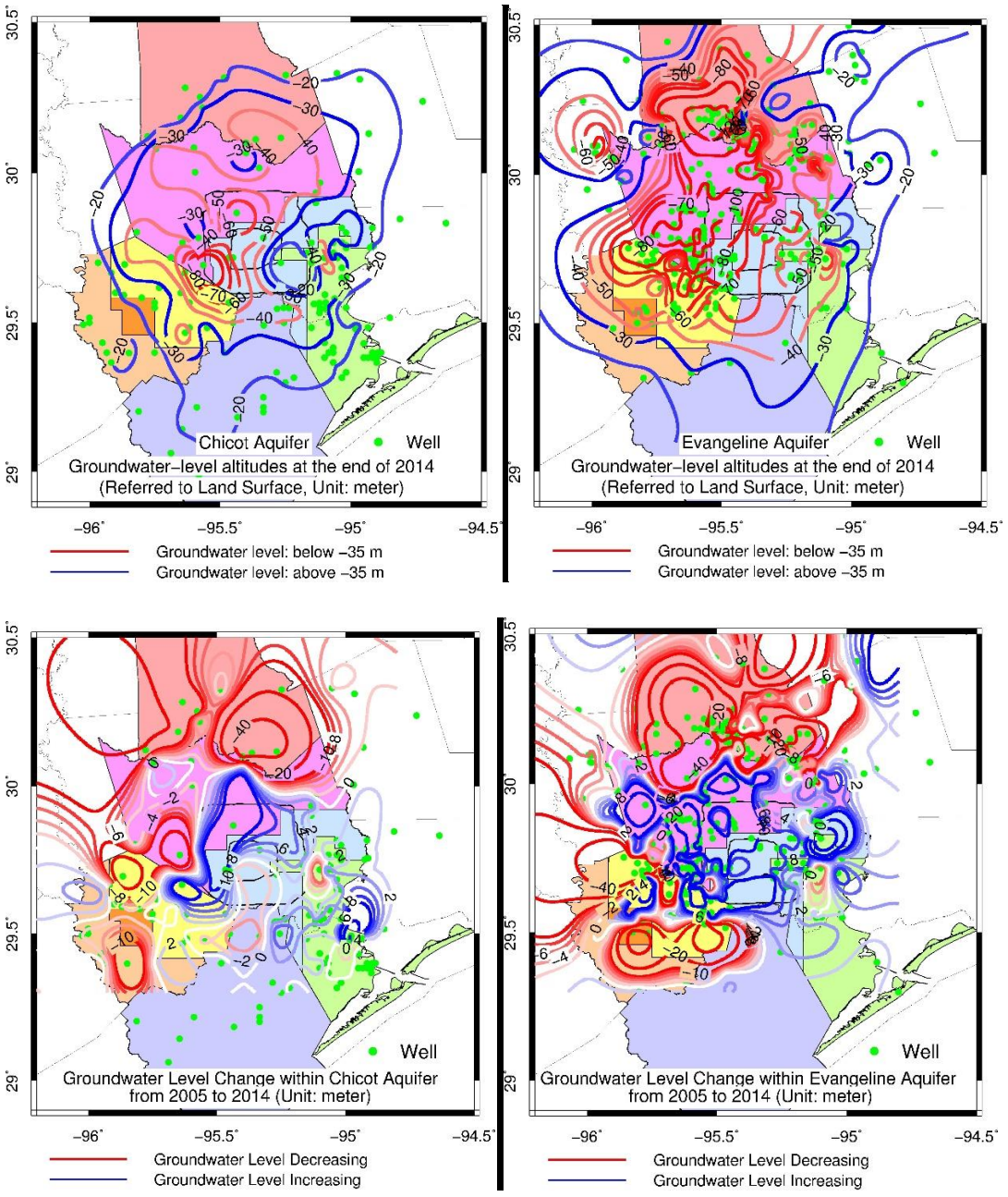

Figure 1.1.7: Contour maps showing groundwater-level altitudes within the Chicot and Evangeline aquifers at the end of 2014 and the changes of groundwater-level altitudes from 2005 to 2014 (Wang et al. 2015). The colored areas represent the groundwater-regulation zones.

1.2 Geology of the Houston-Galveston Area

1.2.1 Aquifers

An aquifer is a body of underground unconsolidated or non-lithified sediments with enough permeability to retain groundwater or permit its transmission to another body. The Chicot, Evangeline, and Jasper aquifers are the primary aquifers in the Houston metropolitan area as the surficial components of the Gulf Coast aquifer system (Kearns et al. 2015). The topmost substantial aquifers, the Chicot and the Evangeline, consist of alternating gravel, sand, silt, and clay layers. These layers dip gradually toward the shore of the Gulf of Mexico at greater inclination than that of the land surface. A detailed description of the aquifer system can be found (Baker 1979) and (Kasmarek et al. 2009b).

Our area of study is an unevenly distributed top aquifer at UHCC; it lies above the alluvium interface which runs between this top surface layer and the Chicot aquifer. The geology of this top aquifer can be described as a “homogenous heterogeneity” consisting of silts, sandstones, and clays—either in combination or exclusively by itself—throughout the focus area. Underneath it are the Chicot and Evangeline aquifers (Figure 1.2.1.1) (Wesselman 1972) which are the primary source of fresh water for many of the small towns and rural areas of the Texas Gulf Coast (Capuano and Lindsay 2012).

Generally, the Chicot aquifer includes all deposits from the land surface down to the head of the Evangeline aquifer. The Evangeline superimposes the

Burkeville Confining Unit and the Jasper aquifer (Figure 1.2.1.1, Wesselman 1972). The Burkeville Confining Unit is composed of mainly clay and restricts the flow of water from the Evangeline aquifer down to the Jasper aquifer. There is no confining unit between the Chicot and Evangeline aquifers; thus these two aquifers are hydraulically connected, allowing groundwater to flow between the aquifers (Ashworth and Hopkins 1995).

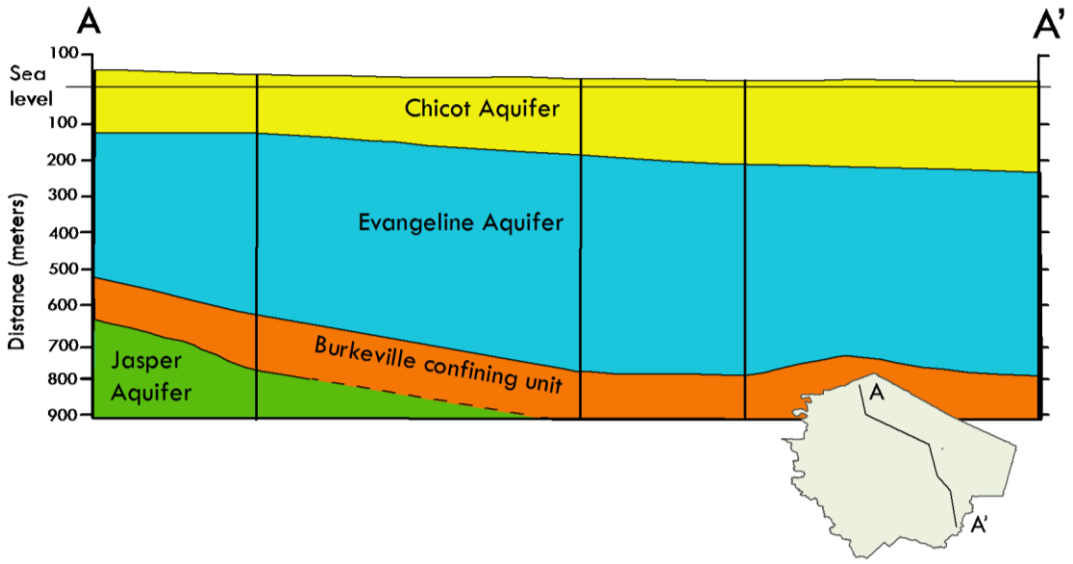

Figure 1.2.1.1: A-A' cross-section of Fort Bend County that depicts the Chicot, Evangeline and Jasper Aquifers and the Burkeville Confining Unit (Wesselman 1972). The vertical thickness of the aquifers and confining unit under Fort Bend County is exaggerated by a ratio of 1:10 (Neill 2015).

The Chicot aquifer is the shallowest major aquifer in the greater Houston area and is thus a frequent subject of research. The bottom of the Chicot ranges from less than 100 m from the ground surface in the north near Montgomery County to approximately 400 m below the land surface in the south near Galveston County, and near the La Marque study area (Shah and Lanning-Rush 2005). In this region, the Beaumont formation, a clay rich layer that overlies and

confines the Chicot, is thought to be relatively impermeable as it prevents recharge or contamination of the aquifer in the study area (Capuano and Lindsay 2012). It is believed that the specific study area in UHCC is not on the Beaumont formation, but a separate, local layer of unconsolidated clays and silts; however, there is evidence to believe that part of the UHCC study surface is the Chicot aquifer, especially when taking into consideration the observed groundwater level measurements.

The Evangeline, however, merits its own reasons for study. The Evangeline aquifer is the principal source of freshwater pumped in the Houston-Galveston area (Coplin and Galloway 1999). Figure 1.2.1.2 explains the overall recharge cycle in a geographic context. Groundwater comes from these two parts of a vast coastal aquifer system extending throughout the boundary of the coastal plain of Texas and Louisiana to Florida. The replacement of the Beaumont by the more permeable, incised valley fill and how it affects recharge had not yet been considered as of 2012 (Capuano and Lindsay 2012).

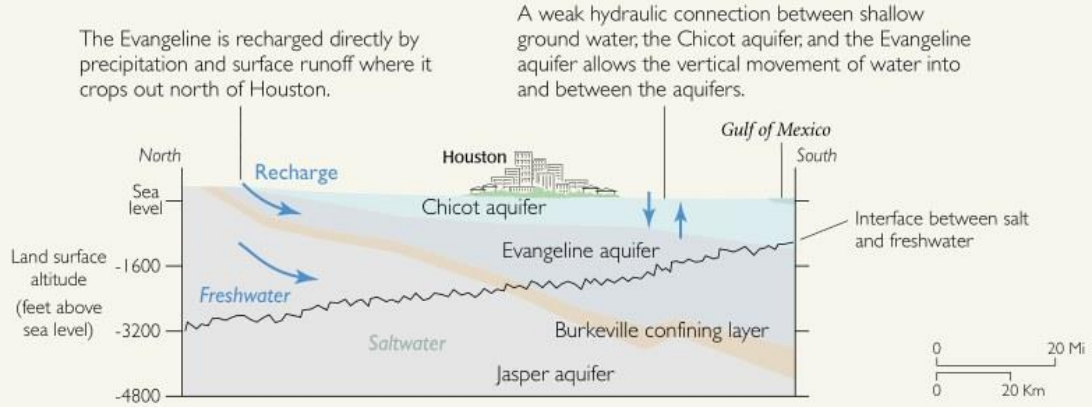

Figure 1.2.1.2: Cross-sectional diagram of the aquifers and their boundaries under Houston (Coplin and Galloway 1999). The recharging action to the north (left) and hydraulic connection between the Chicot and Evangeline aquifers in the south (right); the recharging action occurs throughout the greater Houston area.

Saline intrusion into aquifers are another issue. Historically, the encroachment of saltwater into both Chicot and Evangeline aquifers has been aggravated by lowered ground-water levels, especially near the coast (Coplin and Galloway 1999). Most water supply wells draw from in the upper 1-2 kilofeet of the uppermost aquifers where freshwater is available. The original saltwater in the aquifers was flushed out by freshwater following sea-level recession, though now seawater encroaches on deeper portions of the aquifers. The subterranean brackish interface, between the saltwater and the overlying freshwater, slopes upward to ground level at the Galveston coast. Groundwater quality, levels, and aquifer-system compaction are closely examined by the HGSD to ameliorate any detrimental effects related to over-draught of the groundwater supply.

1.2.2 Geologic History of the Houston-Galveston Area

Houston, Texas, is located in the Gulf Coastal Plain, which runs nearly fifty miles inward from the Gulf of Mexico. The entirety of the Gulf Coastal Plain begins from Mexico in the south out to Florida in the east (Kasmarek and Strom 2002), and logs several thousand meters of Cenozoic sediment deposits (Baker 1978). The complexity of the geology of the Texas Gulf Coast Plain is due to the spatial and temporal variability of the sediment layers which form the Texan coast and the motion of Jurassic salts beneath those varying sediments. Approximately 122-144 km wide, the Texas Gulf Coast comprises these Coast Plain deposits (Salvador 1991).

The Plain has been tectonically stable ever since the positioning of the Yucatan block at the end of the Jurassic, despite the storied tectonic past of the immediate region. Outside the Middle to Late Jurassic marine salts deposited coevally with rift sediments, the sedimentary levels that make up the Gulf of Mexico coastal plain are interbedded sequences of gravel, sands, silts, and clays (Kasmarek et al. 2009a). Strata for the earliest sediments of these interbedded sequences in the Gulf of Mexico developed when Pangaea split during the Late Triassic (Chowdhury and Turco 2006). In the Middle Jurassic, Gulf basin development permitted the deposition of clastic, non-marine sediments, including the Louann Salt, the most tectonically influential stratum of the Gulf of Mexico (Salvador 1991). Though the Gulf basin's seawater flow was restricted during the Middle Jurassic, the resulting movement of the Yucatan in the Late

Jurassic allowed for sporadic seawater incursion that effected massive salt deposition (Bird et al. 2005). Subsequently, a sediment convergence from the adjacent Appalachian and Ouachita Mountains to the north, the Llano and Marathon uplifts to the northwest, and the Chiapas Massif and Maya Mountains to the south caused rapid displacement within the region (McFarlan and Menes 1991; Salvador 1991). At the same time, structures related to salt mobilization, such as growth faults, diapirs, pillows, and sheets, began to form (Nelson 1991).

Next, a major tectonic event called the Laramide orogeny would continue to enormously influence the structure of the Gulf. Terrigenous clastic sediment was transported via varied river systems and deposited into the Gulf by mountain-building events (Coleman et al. 1991). Various sediment depositional regions caused rapid subsidence and extensive deformation, known as “sags” or “embayments.” In response to this depositional loading, isostatic subsidence of the crust developed on a large scale, inducing an enduring coastward tilting of sequentially older depositional sequences.

Approximately 35 to 55 million years ago the Laramide orogeny concluded, though sediment deposition continues to the present day. Within the Gulf Coastal Plain are alternating deltaic and interdeltaic regions wherein the latter consists predominantly of barrier islands, beach ridges, coastal mudflats, and marshes (Lohse 1955). Exposed formations (e.g. Lissie, Willis, and Beaumont) entwine with overlying alluvial deposits and comprise sand, silts, and clays (Reid 1973).

Salt structures would become a significant factor in the next geologic sequence of events. The sediment deposition above the Louann salt was influenced by underlying salt movement (Kasmarek and Strom 2002). This movement occurred at a low surface angle that asymptotically smoothed from the threshold of deposition to the bedding plane. This results in the initiation of a specific type of fault, conventionally referred to as a “listric fault,” which sometimes occurs concurrently with deposition (Serna 2015). Salt flow-structures and listric-fault growth contributed to surface deformation and basin structuring of the region, from the Early Cretaceous to the present day.

Gravity is the principle driving force associated to the Gulf’s listric fault activity. This was a result of coupled, differential movement of sediments toward the basin situated above salt, or abnormally pressured shale (Serna 2015). Significant salt flow preceded the formation of these salt structures, which implies that the salt was relatively pure without sediment (limestone), anhydrite, and poly-halite since these impurities inhibit flow. Within the Gulf Coast region, differential pressure gradients of sediments that overlie the salt can generate structures such as salt diapirs, pillows, and sheets (Jorgensen 1975).

Listric faults can be found in multiple environments. Listric growth faults in the Gulf can be associated with both salt and shale, down to the depositional stratum of the Louann salt (Nelson 1991). These growth fault displacements increase with depth as the fault angle grows shallower such that the growth itself indicates offset caused by rapid sedimentation along the failure plane during the period of deposition (Ewing 1991).

The Beaumont Formation has a distinctive accretion. It contains a relatively high-clay content and marked absence of gravels. The lithology of the Beaumont Formation includes calcareous, mottled clays, sand, and silt. The majority (80%) of the formation consists of colored clays (e.g. pink, red, blue, tan, and grey). The convergence of the Brazos, Trinity, Neches, and Sabine river-deltas comprise the Beaumont Formation (Meyer 1939; Waters et al. 1955; Van Siclen 1961). The sediment column here was deposited and restructured by sea-level change, long-shore currents, and fluvial-deltaic systems (Galloway et al. 2001). The young Rocky Mountains feed sediment-laden streams leading down to the Gulf of Mexico basin (Serna 2015). Fluvial-deltaic and shallow marine sediments are alternately deposited and reworked through sea-level change while the depositional function is that of sea level.

Recently (within 4 ka), the sea level has risen at a relatively slow rate, less than 3 mm/yr, to what is now the modern coastline. Rivers cutting normal into the coastline carried sediment directly into the Gulf of Mexico. A barrier island network arose from the cycle of sediment supply and long-shore currents. The sediment deposits that comprise the present day Texan coast show varying influences from fluvial-deltaic and shallow marine depositional environments. During a time of sea level decrease, shoreside deposits and their connected rivers that supplied sediment moved across the continental shelf. As the sea level rose again, rivers reworked these deposits as the shore migrated back to a high-standing position. This process resulted in the sequence of alternating

coarse, fluvial-deltaic (aquifer) and fine, brackish-marine (confining) sediments within the same area (Kasmarek and Strom 2002).

Both subsidence and faulting induced insidious, imperceptible harm to the infrastructure. They are both forms of surficial motion that cause damage to buildings and roads (Holzer and Gabrysch 1987). Pratt and Johnson (1926) first documented human-induced faulting in the Gulf region. Generally, Gulf Coast faults run parallel to the coastline (Ewing 1991). However, localized faults related to collapsed salt domes or oil and gas fields exhibit arced and radial patterns (Pratt and Johnson 1926; Van Siclen 1968).

Regional faults along the Gulf Coast show a unique history. They are aseismic; there is no dramatic release of stress and strain, but rather an apparent, slow creep (Serna 2015). Offset along faults is about 1 – 3 cm/yr making them difficult to identify since erosion can conceal the scarp (Holzer and Gabrysch 1987; Buckley et al. 2003; Shah and Lanning-Rush 2005).

Salt structures continue to play an important geologic role to the present day. Eight salt domes are present in Fort Bend County with depths ranging from 85 to >2800 m below land surface (Huffman et al. 2004). Six domes shallow enough to penetrate the Chicot and Evangeline aquifers can impede flow and affect groundwater quality (Serna 2015). Shelf-margin growth faults had developed before the salt domes reached their current configuration (Ewing 1983). Faulting within Tertiary deposits along the Gulf was due to a sediment differential in an unstable depositional environment (Ewing 1991). The Oligocene break in the continental shelf margin indicates a change in the

depositional environment, moving from coarse material deposited on the gently dipping shelf to finer materials deposited on the continental slope (Serna 2015).

1.3 Global Positioning System

The scientific tools used for this study generally fall under the area of the Global Positioning System (GPS). GPS is a navigational satellite system created by the US Department of Defense in the 1970's (El-Rabbany 2006). A system of 24 satellites orbit earth at an elevation of 20,200 km and allows worldwide coverage. Distance is calculated with an antenna at ground level to at least three of these satellites, and position is triangulated via a fourth satellite used to compensate for receiver clock offset. Clock offset is an important concern since the distances from surface to satellite are computed by synchronized clocks within both ground and space units. High-precision and high-accuracy displacement measurements (to the centimeter, millimeter, and sub-millimeter magnitudes) by GPS are increasingly used in geoscience applications to measure ground motions associated with landslides and subsidence (Wang 2013).

GPS has become a ubiquitous, useful tool for many sectors such as scientific inquiry and research. Vertical displacements derived from GPS observations are geometric quantities directly used to measure long-term subsidence without utilizing leveling techniques (Wang et al. 2014). Both Precise Point Positioning (PPP) and Online Positioning User Service (OPUS) software packages for GPS data postprocessing are suitable for tracking long-term land subsidence rates.

Though a relatively new technology, GPS has a proven track record for legitimate scientific empirical observation. For more than two decades, current GPS and extensometer observational technology has been applied to study subsidence in many places: Groningen, Netherlands, Rafsanjan Plain, Iran, Ojiya City, Japan, Jakarta, Indonesia, Mexico City, Mexico, Tuscon, Arizona, and New Orleans, Louisiana (Kearns et al. 2015). The HGSD collaborated with the USGS, the National Geodetic Survey (NGS), the city of Houston, the Texas DOT (TxDOT), and other local agencies to establish a dense GPS network in the Houston metropolitan area since 1993.

To provide stable reference frames for regional land surveying and subsidence monitoring, GPS was implemented in conventional surveying techniques by the late 80's. At that time, the full constellation of 24 GPS satellites had not yet been complete. There were only approximately 15 GPS satellites in orbit at the time. The HGSD established many benchmarks in the Houston area and conducted periodic leveling surveys by utilizing GPS techniques in the late 80's and early 90's.

By 1992, the earliest permanent GPS antennas were installed on the inner pipe of three borehole extensometer locales: Addicks (ADKS), Lake Houston (LKHU), and Northeast (NETH). The RMS for each site's ground movement was below 1 cm. The vertical positional time series trend indicated that no compaction occurred in sediments below the bottom of each borehole (at approximately -600 m) during the last 20 years (1993–2012).

The USGS has been operating a network of borehole extensometers consisting 13 stations at 11 sites in HGSD since 1974. Extensometer installation and groundwater regulation implementation commenced at around the same time in the mid-70's. The borehole extensometers in the HGSD area were designed as double-pipe wells drilled to preselected depths. There is an approximately 3 m-high opening screen at the bottom of the outer case on each borehole extensometer (Poland et al. 1984; Gabrysch 1984b); this screen facilitates groundwater flow both in and out. Thus, these extensometers also function as piezometers that can also monitor the groundwater level within the aquifer wherein the well was terminated.

The compaction rate differs at each borehole extensometer site due to the different groundwater withdrawal rates in the adjacent areas of each site, in addition to the varying clay-to-sand ratios of the subsurface sediments. A recent investigation at the Addicks site indicated that its compaction measurements compare very well with the subsidence measurements of a permanent GPS station (PA05) with closely-spaced antennae (50 m) over the last two decades (1994–2013) (Wang et al. 2014). Monthly compaction measurements had an accuracy of 2 mm (Kearns et al. 2015). The performance of other extensometers in the Houston area are also expected to be very reliable and retain the same level of accuracy since all extensometers were designed, constructed, and maintained to USGS regulation.

The height displacement time series recorded at shallowly anchored GPS antennae can assess the true accuracy of the subsidence time series of the

study area (Wang et al. 2014). The compaction rates derived from the borehole extensometer data represent the total subsidence, which should be approximately equivalent to the vertical displacement recorded by the shallowly anchored GPS antenna PA05. Continuous GPS data collected from the deeply anchored GPS antennae there indicate that the bottom of the borehole has been stable over the past 20 years (1993–2012).

The analysis indicates that the difference between the cumulative subsidence rates measured by the extensometer and by the corresponding GPS antenna is less than 5 mm from 1996–2012, a period of 17 years. The RMS of the residuals of the monthly subsidence time series derived from the extensometer data and GPS antenna data from 2000–2012 is 2 mm. This means that in relatively short-term studies not extending past two decades, both data collection methods via extensometers and via GPS antennae are viable and sufficiently accurate for analysis.

The Absolute Positioning Approach used for GPS displacement measurements solves for a single GPS station's position without using synchronous observation from other ground GPS stations, and instead uses precise satellite ephemeris data (i.e. data for the exact celestial location) and clock data (Wang 2013). The advantages and disadvantages of these two GPS data post-processing approaches have been carefully discussed in previous publications (Grinter et al. 2011; Rizos et al. 2012; Wang 2013). The typical absolute positioning approach uses the precise point positioning (PPP) method, which uses undifferenced dual-frequency, pseudo-range, and carrier-phase

observations alongside precise satellite orbit data and clock information to determine the position of a stand-alone GPS station (Goad 1985; Zumberge et al. 1997; Kouba and Springer 2001; Ray et al. 2004; Kouba 2005).

GPS subsidence and ground movement studies will at the least support and at most obviate traditional ground movement measuring methods (Gili et al. 2000; Bruckl et al. 2006; Tagliavini et al. 2007; Peyret et al. 2008; Hastaoglu and Sanli 2011; Wang et al. 2011; Wang 2012). The usual relative positioning approach uses the carrier-phase double difference method, which transforms station-differenced to satellite-differenced phase-bias ambiguities into integer values (Blewitt 1989; Dong and Bock 1989; Eckl et al. 2001; Herring et al. 2009; Wang et al. 2013). The double difference method requires observation by at least two GPS receivers, simultaneously.

Subsidence time series are fundamental for quantifying local aquifer compaction; therefore it is critical to track the long-term performance and assess the accuracy of the subsidence time series. Some accuracy concerns stem from slight flexing of pipes over time, which could cause friction that affects the performance of the system, and human interaction, which could accumulate because these measurements measure cumulative. For this reason, any overall trends noted by the GPS positional displacement data in this study under 2 mm were accounted for as systemic or user error and omitted from final results. For this reason and also for convenience, submillimeter displacement readings were rounded to millimeters.

1.4 Overview of the Thesis

Because the reasons for HGSD's localized, shallow-depth subsidence were unclear at the time, this study was opened in 2014 to investigate the nature of ground deformation in the UHCC. Firstly, the crux of the data to be considered is the GPS positional displacement dataset. This body of data consists of northing, easting, and height coordinates measured via coordination of the GPS satellite network and a ground-surface-level antenna array set in the University of Houston's Coastal Center (UHCC). These displacement measurements ran from February 18th, 2014, to February 1st, 2016.

Secondly, accumulated incremental rain measurements were gathered daily at the UHC0 weather antenna at the same exact site as the GPS satellite antenna array. These rain measurements run from April 17th, 2014, to February 1st, 2016. Both the GPS and Weather data are automated and continue to collect daily data at intervals of 15 and 60 seconds, respectively.

Lastly, groundwater level was measured manually by a water-level meter at two sites of the UHCC; one directly situated at UHC3 called the "Gray well" and two others, herein named "Red well" and "Blue well", situated on an adjacent, separate aquifer, just 100 meters northeast from the UHC antennae. The Gray well typically measures at around 10 feet, whereas the Red and Blue wells read head levels of around 80 feet. These water levels were measured from May 20th, 2014, to February 20th, 2016, on a near-monthly basis, albeit with a lack of data midway during parts of 2015.

The displacement vs rainfall and displacement vs well-depth analyses will address whether there are correlations between the three datasets, and what their quantitative relationships are. This thesis will expound upon the assumptions made in order to elicit correlations (or lack thereof) between the three data, explaining in detail: the background of this study in the introduction, the materials and methods needed to conduct this study, the three sets of data to be analyzed, namely GPS measurements of ground displacement, weather and precipitation, and groundwater wells, and finally a restatement of conclusions and discussions for further study.

1.5 Conventions

Lastly, there exist some key reference frames and naming conventions to keep in mind when understanding the overall data for ground deformation. When an antenna is mentioned just by its designation (e.g. UHC1, UHC2, UHC3, UHC0), this typically refers to the measurements of its plug base, not the antenna itself. UHC0's body of measurements (at 0 feet, ground level) itself is also in flux; thus, a positive height displacement of a ground layer (e.g. 10 feet below surface) may not be true uplift but a more pronounced compaction of UHC0. UHC1, UHC2, and UHC3 have their measurement foundations set at 10, 20, and 30 feet, respectively below the ground surface level of 0 feet as defined by UHC0's base.

In terms of GPS data, *northing* is the longitudinal position along the Earth's N-S surface axis, where north is positive and south is negative; *easting* is the latitudinal position along Earth's E-W surface axis, where east is positive and west is negative; and *height* is the radial position from Earth's center out, where out from the center and up on the surface is positive and in toward the center and down on the surface is negative. Both absolute and relative positions are measured by UHCC's antennae. In the document, "UHC antenna array" or "UHCC's antennae" refer to the same set of data-gathering instruments. "UHCC" refers to the coastal center's premises itself, wherein the four "UHC" antenna poles reside (e.g. UHC1, UHC2, UHC3, UHC0). These terms are used interchangeably unless otherwise specified. The GPS data from the UHC

antennae are gathered by their one-to-one corresponding GPS receivers, converted to RINEX data using TEQC, post-processed using TopCon Tools, tabulated in Microsoft Excel wherein they are differenced by a fixed, early value within their own set, and analyzed statistically on Excel and graphically on CoPlot.

These differenced values are considered the *displacement* set of measurements. The northing, easting, and height displacements are the primary set of data, to be analyzed and to be compared to the Weather and Well data. These two measurements of daily rainwater accumulation data and well water-level depth data are juxtaposed with displacement data to find any qualitative or quantifiable correlations. GPS position and rainfall data collection are automated, high-precision processes that work with higher quantities than the manually measured well depth data.

The designated depth differences between UHC1, UHC2, UHC3, and UHC0 are estimated and imprecise, but their absolute measurements and thus their displacements are accurate to the sub-micrometer level; therefore, when in the rest of this document, “positional”, “locational”, “height”, “elevation”, “GPS”, “ground layer” (as opposed to “ground level”, meaning at UHC0-defined “0 feet”), or any other unspecified type of measurement data, by default, mean the *dataset of calculated displacements of GPS elevation/Z-axis/height measurements, of individual depths denoted by the number at the end of the GPS antenna name in the tens of feet (e.g. “UHC2” measures the movement at “20 feet” below the*

surface level defined by UHC0 as "0 feet"), with respect to UHC0's GPS antenna data.

Otherwise, when expressly denoted as any combination of the words "northing-longitudinal Y-axis", "easting-latitudinal X-axis", "rain-fall precipitation accumulation weather", or "well-depth-head groundwater level" data, they refer to, respectively, the *north-south displacements of GPS locational data measured at UHCC's antenna array*, the *east-west displacements of GPS locational data measured at UHCC's antenna array*, the *daily rainfall accumulation weather data measured at UHCC's antenna array by the weather sensor located on UHC0's antenna*, and the *displacements of groundwater level data measured at UHCC's wells located at UHC0's foundation (Gray well), and at a pair of wells set on a nearby yet separate aquifer (Red and Blue wells)*.

Regarding the displayed magnitudes of graphed data: for graphical comparison to be feasible, GPS-northing, -easting, and -height displacements have been set to unit millimeter, daily-rainfall accumulation to unit centimeter per day, pressure change to unit 3 millibar, humidity change to unit 10%, dry temperature to unit 2 degrees Celsius, and well-groundwater-level displacements to unit 1 or 2 decimeters.

Finally, it may seem more intuitive to use UHC3's deepest 30 foot foundation as the control point for the other three layers above; however, not only are all four layers mobile, but also since the surface level spatial change is quite different from that of the also moving subsurface layers, that it is better to set UHC0 as control to emphasize the highly comparable UHC1, UHC2, and

UHC3 measurements. In other words, it is exactly because UHC0 is so dissimilar from UHC1, UHC2, and UHC3 that it is set as the reference point to more precisely distinguish between the closely trending movements of the latter three.

2 Materials and Methods

2.1 GPS Antenna Array - Design, Construction, and Data Processing

2.1.1 Design

One of the key questions posed on the issue of subsidence was: “What are the contributions from shallow sediments?” where “shallow” here means within ten meters from ground surface level. These concerns were addressed by installing a vertical GPS array and a weather sensor in UHCC, within the premises of which there are three groundwater wells with depths ranging from 5 to 100 m below the ground. GPS data, precipitation data, and groundwater head measurements have been collected for analysis from February 2014 to February 2016; the GPS and precipitation data are automated, whereas the well data were measured by hand.

The GPS array includes four permanent stations with the antenna poles anchored to concrete plugs at different depths below ground surface level. The names of said antennae are UHC1, UHC2, UHC3, and UHC0, with each numeral reflecting the rough measurement of its concrete plug depth in the tens of feet: UHC1’s base is at roughly 10 feet, UHC2’s base is at roughly 20 feet, UHC3’s base is at roughly 30 feet, and UHC0’s base is near surface level of 0 feet—actually at 1 foot below the surface. The array provides ground deformation data as a measure of compaction at different ranges of depth relative to the surface, which will indicate the level of compaction of the ground layers on which the antenna array is emplaced.

The concept of the four UHC antennae is seen in Figure 2.1.1.1, left. The yellow squares shown are concrete foundations set at ground level, with both antenna poles and their protective, outer PVC casing pipe dug into the ground ending at a concrete plug at the bottom. On the surface, the four look near identical, however (Figure 2.1.1.1, right).

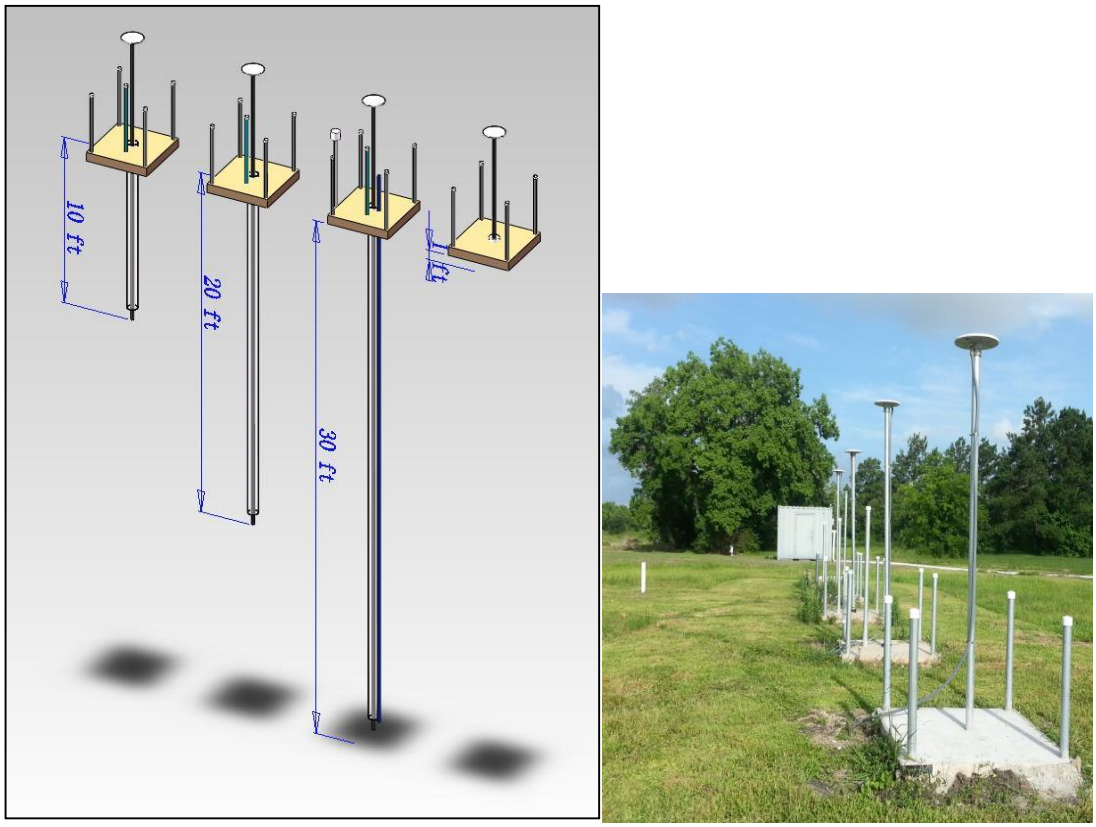

Figure 2.1.1.1: (left) Conceptual diagram of the UHCC vertical GPS array. From left to right: UHC1, UHC2, UHC3, UHC0. (right) Photo of UHCC vertical GPS array, this profile picture was taken from the west facing east. The GPS stations are arranged in the following order (from far back to near front): UHC1, UHC2, UHC3, UHC0.

The concrete slab is 4 foot by 4 foot, horizontally, and 4 inches high off the earth (Figure 2.1.1.2). Four, 4' corner posts are set halfway into the ground during concrete curing to stabilize and guard the antennae poles. The antenna poles are 2 inch

galvanized steel pipes inside a 2.5” protective PVC pipe that are coupled at the surface loosely for ground movement to be freely but accurately measured. At the bottoms, sand covers the concrete plugs at their bases to stabilize ground layer movement for better accuracy. Lastly, one 1” PVC pipe is set along UHC3’s antenna pole PVC pipe to measure the onsite groundwater level; the construction of the entire array is covered in Section 2.1.2, and the instrumentation and data processing is covered in Section 2.1.3.

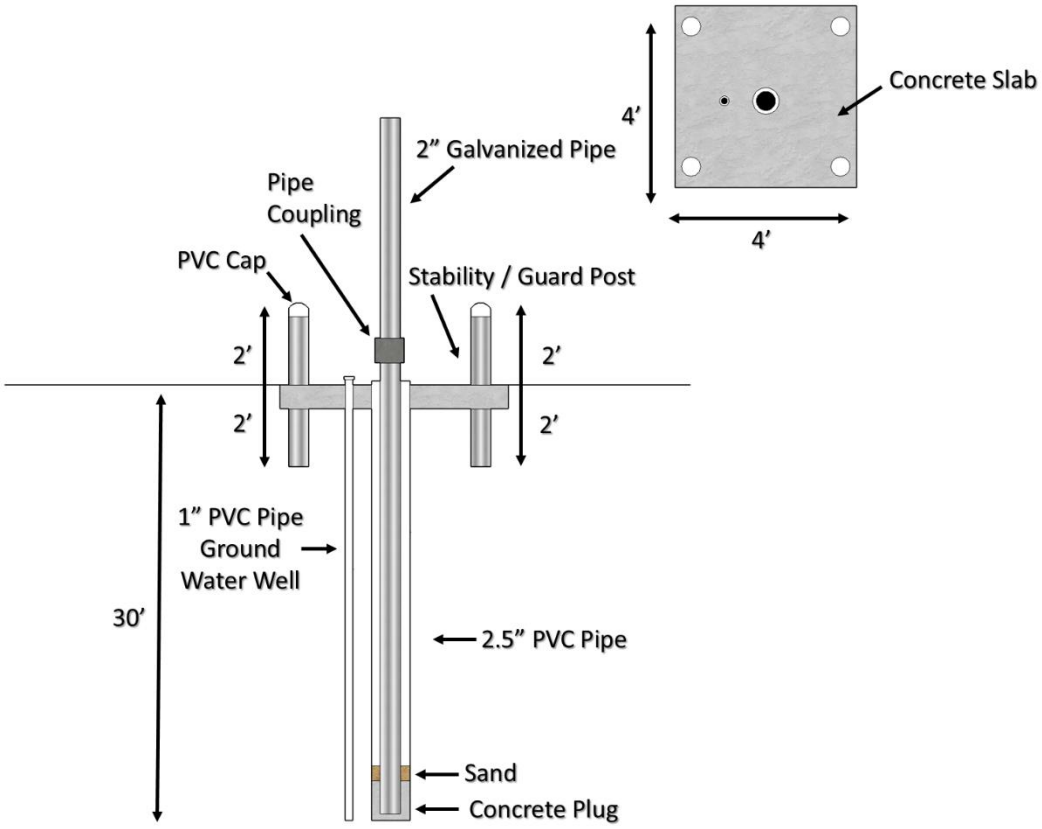

Figure 2.1.1.2: Monitor schematic of UHC3, from the surface to concrete plug located 30’ bls.

2.1.2 Construction

The construction of UHCC's antenna array began in January 2014, and the following month of February, right before actual GPS measurements were reported. The four antennae, UHC1, UHC2, UHC3, and UHC0 are in that respective order from west to east as shown in Figure 2.1.1.1. As mentioned earlier in Section 2.1.1, each antenna pole has a square concrete foundation, of 4 feet by 4 feet horizontal dimension, and 4 inches off the surrounding-earth level (Figure 2.1.2.1, left).

Among the many contracted heavy equipment needed for drilling the holes was a crane (Figure 2.1.2.1, right) whose drill was used simultaneously with a water pump to flush out the drilled sediments (cuttings) where the extensometer pipes were to be laid. A wooden box was framed to hold the flushed cuttings which were taken for further analysis by other researchers working this area (Figure 2.1.2.2, left). Doing so, the company can install the antenna poles to be placed at specified depth with a concrete plug (Figure 2.1.2.2, right).

A 2.5" outer PVC casing was overlaid around the 2" galvanized steel antenna pole, and a steel trough was used to divert flushed sludge and debris from the site (Figure 2.1.2.3). For UHC2 and UHC3, the PVC casing came in segments of around 10 feet in length, and needed to be adjoined during installation (Figure 2.1.2.4).

Figure 2.1.2.1: (left) Foundation for UHC3 concrete pad; the smaller white PVC pipe is for monitoring groundwater. This pipe is designated the “gray well” within this document. The dimensions for the concreate pad are 4’x4’x4.” (right) Crane drilling and flushing out cuttings (drilled rock shards) to be deposited on surface.

Figure 2.1.2.2: (left) A wooden box was used to hold cuttings for further analysis. (right) The water well company installed a 40 foot, galvanized steel pole to be placed at depth with a concrete plug. A GPS antenna is affixed at top of the pole.

Figure 2.1.2.3: The photo depicts the outer PVC being slid over the galvanized steel pole. The purpose of this is to reduce friction between the galvanized steel pole and subsurface. The photo also depicts substantial silt and clay flow within the steel trough. The subsurface largely consists of a clay-silt-sand matrix.

Figure 2.1.2.4: This photo depicts the 10 ft segmented PVC pipes used to construct a 30 ft section that is slid over the galvanized steel pole that is completed at depth with concrete plug and affixed at the top with a GPS antenna.

The thinnest pipe in the installation serves as the groundwater onsite well of the array. Slits were cut into the sides of the well to serve as a “well screen” that further facilitates water flow from neighboring ground layers into the well pipe, and vice versa (Figure 2.1.2.5, left). The 1 inch PVC well pipe is affixed to the outer casing PVC pipe of the UHC3 antenna pole (Figure 2.1.2.5, right), the outside of both being flushed with water to exhume debris and other cuttings.

Figure 2.1.2.5: (left) Slits cut into 1” diameter PVC “gray well” pipe in order to create a “well screen,” which enables water to flow more easily into and out of the well, but prevent soil from filing the well. (right) The co-located GPS antenna (UHC3) PVC pole casing.

Water was pumped into the “Gray well” to further flush out sediments, cuttings, and debris out of the piping (Figure 2.1.2.6, left). Sand was then dumped around both these PVC casing pipes for relative stability, and water pumped yet again to flush out remaining sludge (Figure 2.1.2.6, right). The cuttings were left to drain and dry, and were categorized according to what depth they were dug from (Figure 2.1.2.7).

Figure 2.1.2.6: (left) Water pumped into “Gray well” to further flush debris and cuttings. (right) Sand dumped around both PVC pipes for stability. Water again pumped into well to flush out debris.

Figure 2.1.2.7: Cuttings collected from the approximate depths of 6 ft (left), 12 ft (middle), and 21 ft (right).

A lattice of reinforced bars (rebar) was laid out in both horizontal directions to lay the framework for the concrete of the foundation (Figure 2.1.2.8). This rebar-guided concrete solidified and cured to become “reinforced concrete”.

Figure 2.1.2.8: A rebar lattice is placed within the wooden frame before pouring concrete in order to reinforce the foundation. Concrete reinforcement was added to slow degradation of the concreate pad and add stability to the structure.

Four bags of dry concrete were poured onto the lattice abovementioned at each quadrant (Figure 2.1.2.9, top). The concrete was mixed and cured over the rebar, four corner stability rods, and PVC casings (Figure 2.1.2.9, bottom left). The finished installation (Figure 2.1.2.9, bottom right) also had the original installation location of the Vaisala Weather Sensor Antenna on one of the stability poles that would later be moved onto the roof of the building instead (discussed in Section 2.2). The final complete array is shown in a cropped panorama shot in Figure 2.1.2.10.

Figure 2.1.2.9 (top): Dry concrete before mixing and curing. One bag each was poured near the four corner poles for in order to protect the galvanized steel pipe in the center. (bottom, left) Textured and smoothed concrete foundation. (bottom, right) The completed station contains a GPS antenna, a co-located groundwater well (gray well) and the Vaisala Weather Sensor Antenna. The weather sensor antenna has since been moved to proximal location near the station.

Figure 2.1.2.10: Panoramic view of finished UHCC antenna array, facing northward.

2.1.3 Data Processing

Each GPS antenna measures its base's total horizontal (N-S and E-W) and vertical (U-D) absolute position with respect to the IGS08 ellipsoid, and are recorded by four GPS receivers (Figure 2.1.2.1). The firmware for these receivers catalogs each 15 second data as \15sec\ and each 1 second data as \1HZ\; the latter has been discounted since 1 Hz data was less consistently gathered than the 15 second data—though these data would also have gaps, notably in February 2015 for UHC1.

Extraction of the data requires a USB cable and port with any modern operating system's file manager (e.g. Windows Explorer), or can be shared via file-transfer-protocol (FTP) with an Ethernet cable using an FTP program such as FileZilla. For ease of access and additional security redundancy, the receivers send their data up to UNAVCO's servers at the end of each day at midnight on a daily basis (UNAVCO 2013). These data are available for download by anyone with UNAVCO's Data Archive Interface v.2 (DAI) (Figure 2.1.3.2).

The DAI has Quality Control/Check (QC) information available for every station (Fig 2.1.3.3). QC shows the number of GPS satellite observations per day, multipath values for the first and second passes, and the frequency of skips for a given day of measurement. The MP1 and MP2 values are TEQC-computed values (in meters) of the root-mean-square moving-average values of the multipath combinations (Yang et al. 2015). MP1 and MP2 are linear combinations of the L1 and L2 pseudorange multipath observations for the

carrier-phase C/A or P-code observations. The MP1 and MP2 values can be acquired with the following formulas (Rocken et al. 1995):

$$MP1 \equiv p_1 - \left(1 + \frac{2}{\alpha - 1}\right)\Phi_1 + \left(\frac{2}{\alpha - 1}\right)\Phi_2$$

$$MP2 \equiv p_2 - \left(\frac{2\alpha}{\alpha - 1}\right)\Phi_1 + \left(\frac{2\alpha}{\alpha - 1} - 1\right)\Phi_2$$

where p_i = pseudorange measurements; U_i = phase measurements (i = observation frequency, $i = 1 \equiv$ L1; $i = 2 \equiv$ L2); and α = coefficient of relating the ionospheric delay for L1 and L2 and can be expressed as $\alpha \equiv (f_1/f_2)^2$, where $f_1 = 1.57542$ GHz is the frequency of L1, and $f_2 = 1.2276$ GHz is the frequency of L2.

GPS Data obtained from the sites within the monitoring network must be converted into useable data. This dataset should be able to provide geometric positional data (Wang and Soler 2013). The processing workflow begins with the conversion of the raw files into a more useful, standardized format. From UNAVCO's DAI, a compressed bulk download of .d files, .m files, and .n files is given; these are compressed Hatanaka observational, meteorological, and navigational files, respectively. The Hatanaka to RINEX software (crx2rnx) converts Hatanaka .d files into RINEX format .o files (SOPAC 2015). These RINEX files are then processed with Topcon Tools, a processing and analysis software (Topcon Totalcare 2016), and the precise relative displacement can be calculated (Wang and Soler 2013).

Figure 2.1.3.1: GPS receivers for UHC1, UHC2, UHC3, and UHC0. Each is connected via USB 2.0 cable and has its data extracted via a file manager on any computer device.

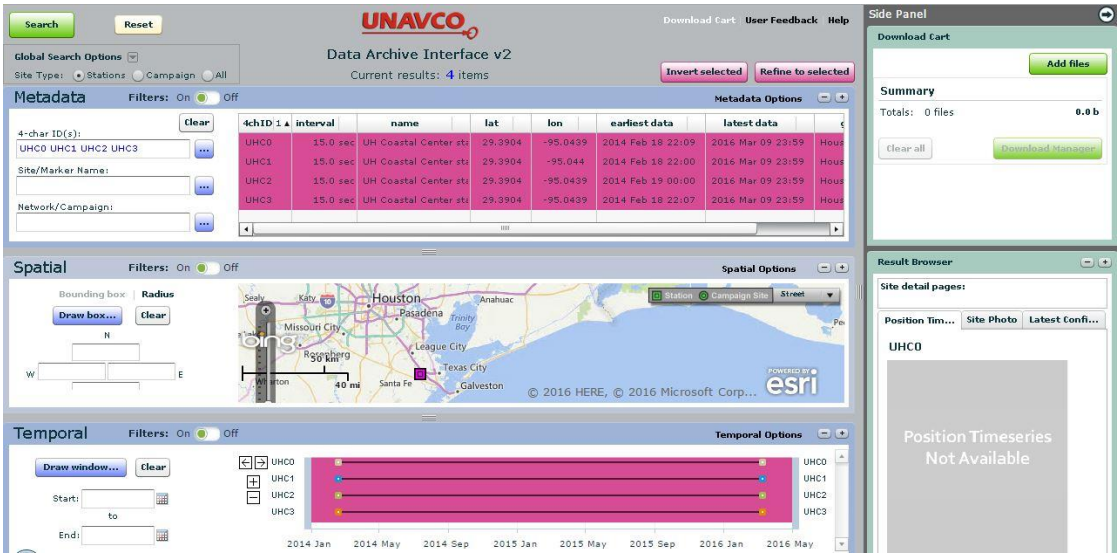

Figure 2.1.3.2: UNAVCO's Data Archive Interface v2 at http://www.unavco.org/data/gps-gnss/data-access-methods/dai2/app/dai2.html# where UHCC's GPS data can be downloaded.

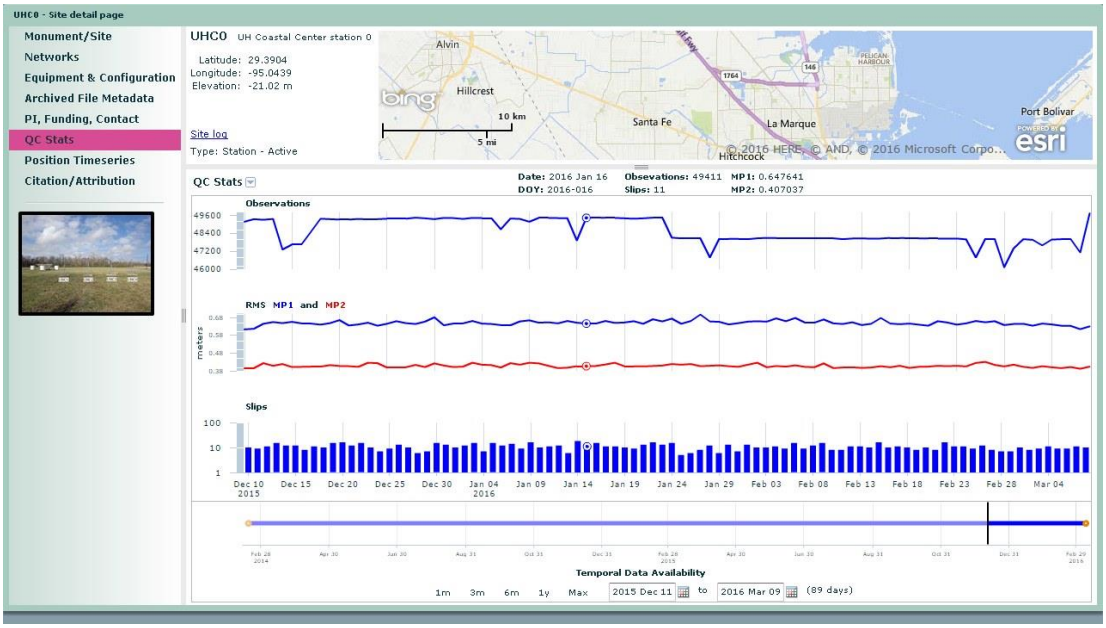

Figure 2.1.3.3: DAI v2's Quality Control/Check (QC) statistics for UHC0.

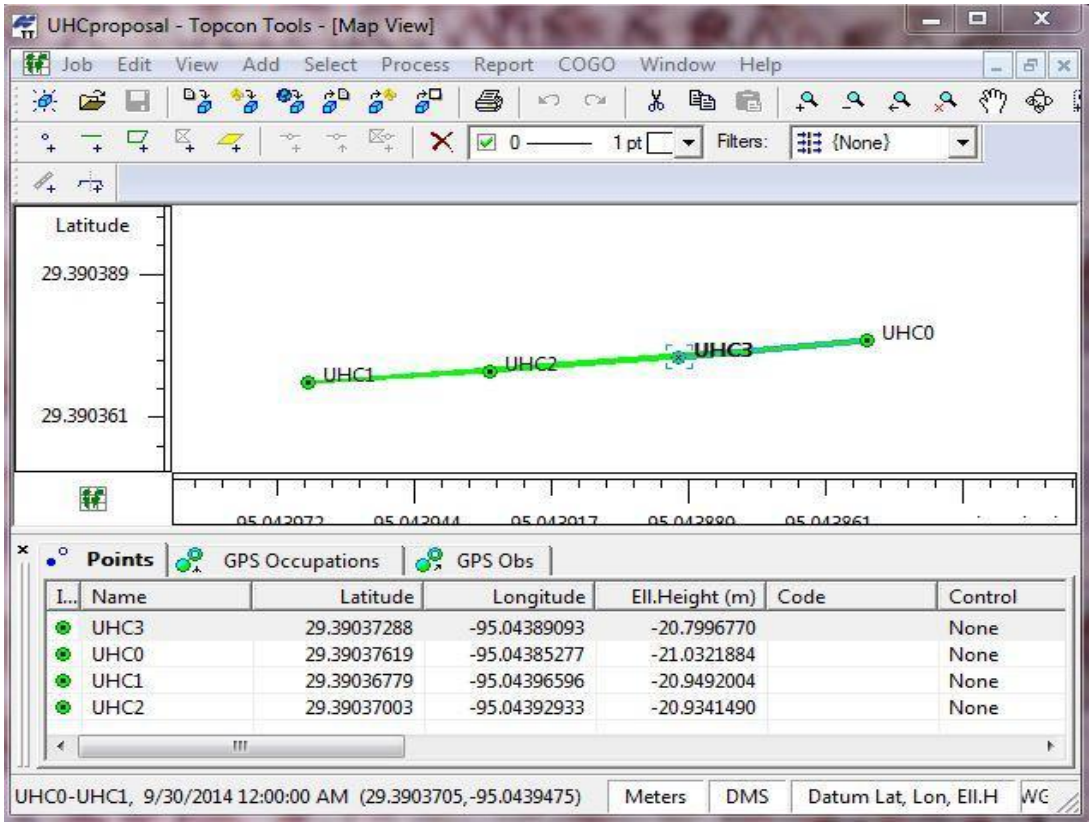

Figure 2.1.3.4: A Map View representation of the Topcon Tools program ver. 8.2.3.

Both the converted RINEX .n and .o files are first imported into Topcon Tools, and categorized according to the antenna the data would correspond to. Checking on Map View (Fig 2.1.3.4) to ensure that the points can be organized only to the antennae meant to be measured from, GPS PostProcess+ is performed on the .n and .o files for final exporting. The third and last step is to export a comma-separated-value (CSV) report that contains northing, easting, and height measurements, horizontal RMS, vertical RMS, distance, duration, and time (date) data for every row of daily measurement. Topcon Tools outputs data according to pairs of antenna measurements (e.g. UHC0-UHC1, UHC0-UHC2, UHC0-UHC3). The control for this study is UHC0, the antenna, station, and receiver which measures surficial movement. It is used to measure the relative movements of UHC1 at 10 feet below UHC0, UHC2 at 20 feet below UHC0, and UHC3 at 30 feet below UHC0.

This data report exported to Excel must first be separated into columns, then sorted by date. The *displacement* data is used to ultimately plot over time in CoPlot for a visual understanding of the trends in the three orthonormal directions of displacement, north-south (northing), east-west (easting), and elevation or height (up-down). These positional data are thus zeroed according to a value set at a particular date (row) in the column—and multiplied by a thousand to obtain millimeter measurements—for northing, easting, or height. A similar procedure to graph well-water-level displacement time series was performed.

2.2 Weather Sensor

The weather sensor (Vaisala WXT520, Figure 2.2.1, left) measures various weather phenomenon data, which are recorded as .m files in UHC0's GPS receiver. The weather sensor was initially placed at UHC3 (Figure 2.1.2.9, bottom right), but the antenna's distance from the UHCC main building where the receivers are sheltered required a longer cable that contributed significant attenuation and noise issues to the data. Thus, the sensor was moved to the roof of the UHCC building (Figure 2.2.1, right) in order to use a shorter cable that minimized outside interference for data collection.

Figure 2.2.1: (left) The Vaisala WXT520 Weather Sensor Antenna. (middle) Said sensor antenna fixed atop the UHCC main building. (right) Same picture as middle taken with larger sight radius.

The meteorological .m files recorded by the weather sensor contain weather data collected on intervals of one minute for 24 hours per file. These files can be viewed with any text editor such as Notepad++, a more robust word editor than standard Microsoft Notepad (Figure 2.2.2). From each .m file, the seven categories of data measured for that particular date can be found.

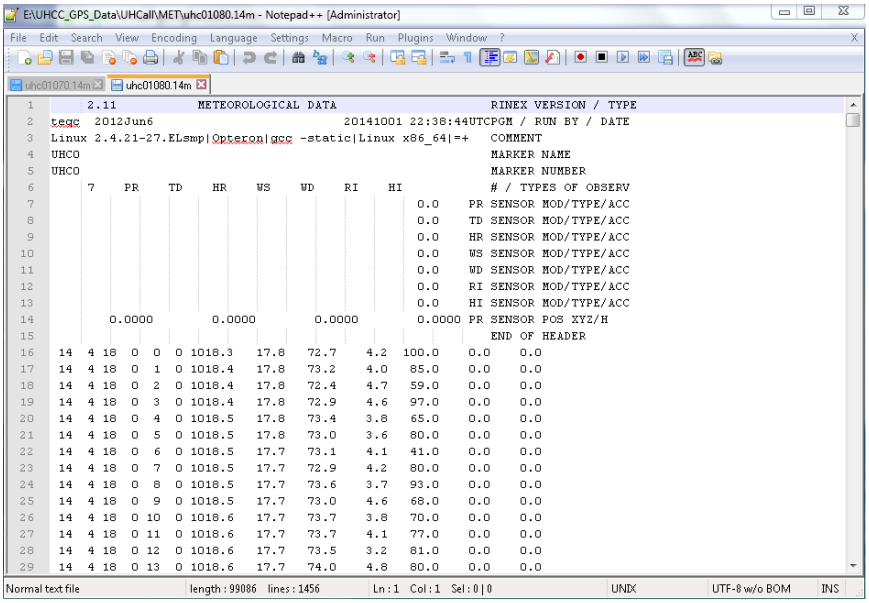

Figure 2.2.2: The content of meteorological .m files opened on a text editor, Notepad++.

The first six columns are Year (only the last two digits), Month, Day, Hour, Minute, and Second, respectively. The header categories are “PR TD HR WS WD RI HI”, which are, respectively: Pressure (millibar), Dry Temperature (degrees Celsius), Relative Humidity (%), Wind Speed (m/s), Wind Direction (degrees, from where the wind blows, zeroed at North, clockwise), Rain Increment (per 0.1 mm, accumulated), and Hail Indicator (Boolean) (IGS 2013). Discarding hail, wind direction, and wind speed was done as it is assumed those factors have negligible effect on UHCC’s ground layer movement or groundwater

depth. Only rainfall, pressure, humidity, and temperature were considered, as shown in Section 5.

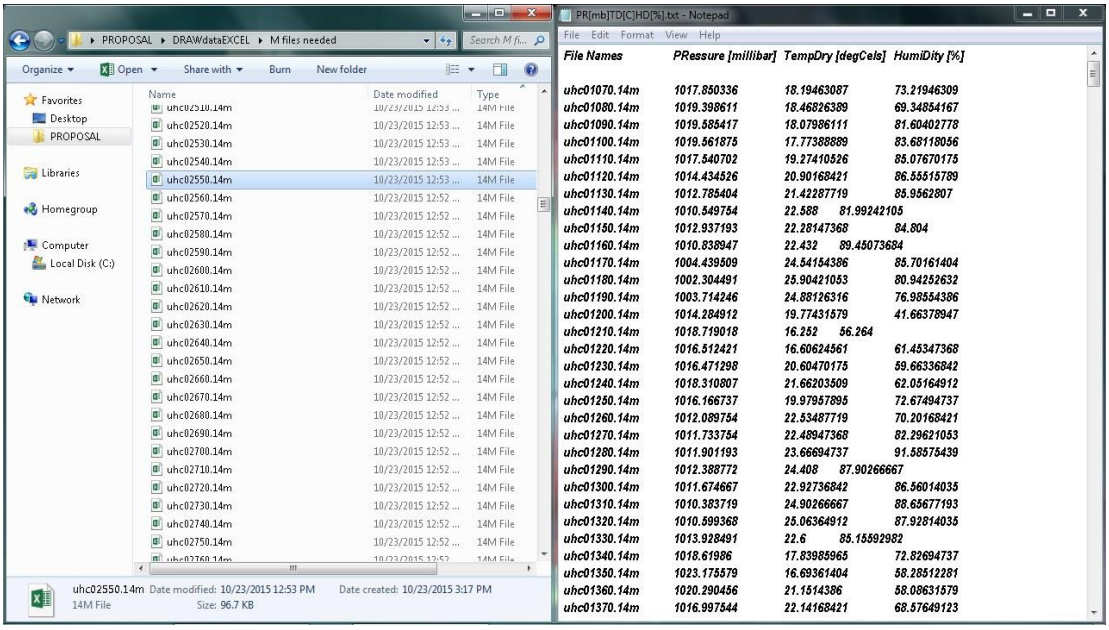

Figure 2.2.3: Setup used to manually extract calculated quantities from individual .m files. Only two windows were left open for a macro-specific workaround.

In order to make use of these data, and since TopCon Tools does not process .m files, rainfall and averaged pressure, humidity, and temperature were individually summed for every .m file and tabulated them in a .txt file to collect the calculated data into an Excel spreadsheet. This required a keystroke macro program called AutoHotKey (AHK) that makes use of keyboard macros. A workaround for Alt+Tab was used because AHK cannot stack Alt+Tab inputs, so Alt+Esc was used instead and the active windows were reduced to two on the desktop (Figure 2.2.3).

2.3 Groundwater wells

In addition to the four antennae are three wells used to measure groundwater levels (Figure 2.3.1). One is right at the antenna array, designated the “Gray well” (Figure 2.3.1, left), and measures the groundwater level of the UHC antennae array site. The other two are set a distance of about 100 m away to the east on a separate but adjacent aquifer; these wells are aptly named “Red well” and “Blue well” (Figure 2.3.1, middle and right, respectively).

Figure 2.3.1: Wells located at the vertical GPS array area – (left) “Gray well” – and at a separate well site that rests on an adjacent aquifer, with the (middle) “Red well” 10 meters closer to the array than the (right) “Blue well”.

The latter two groundwater wells have depths of 100 m below the surface, which measures the groundwater head within the Chicot aquifer, a major shallow aquifer that provides industrial and civilian water usage. The Red well is 10

meters closer to the antenna array than the Blue well, and has its surface well situated slightly higher than the latter, by about 34.9 cm (Table 5.1.1).

Figure 2.3.2: (left) The Solinst water level meter Model 102 measures in decimal feet, the measuring cord juxtaposed to a yardstick found in situ (right) to show each numbered unit is 1/10th of a foot, not an inch (Solinst 2016).

The wells were measured with the Solinst Water Level Meter Model 102 which measures in decimal inches (Figure 2.3.2). The Model 102 Water Level Meter is designed to measure groundwater levels, especially in small diameter tubes, piezometers, and where flexible instrumentation is needed (Solinst 2016). It uses a pair of small diameter probes attached to a narrow coaxial cable, fitted on a reel powered by a standard 9 volt battery. If the probe becomes submerged in water, the electrical circuit at the end of the cable is completed and sends a signal back to the reel where a light and noisy buzzer are activated (Figure 2.3.2, left).

The water level is then measured directly from the cable's markings (Figure 2.3.2, right) at the top of the internal well piping. A sensitivity control allows the buzzer to be scaled back or turned off while in both high- and low-conductivity conditions, such as cascading water, and ensures a clear signal; stationary-well water depth was measured instead, and not a more dynamic open system such as "cascading water."

As later defined in Table 5.1.1, the water level is not measured at the colored-metal outer casing as in Figure 2.3.3, but rather at the lip of the white PVC pipe on the inside (Figure 2.3.4, right). All are accounted for by the end-resultant absolute well-water depth values (Section 5.1) and thus also their displacements (Section 5.2). A diagram of the two wells is given by Stephen Potter (2014), explaining the situation regarding well surface levels, slight water table gradient (from east to west, or Blue to Red wells), and well depths (Figure 2.3.5). It must be noted that the quantities in this figure were not considered for this study and that this study has its own methods to ascertain well-surface and well-water altitudes and displacements.

Figure 2.3.3: Same in-situ yardstick (Figure 2.3.2, right) used to measure height of outer protective metal casing in both inches (top) and in metric, down to the millimeter (bottom). The inner PVC pipe's height is where the water meter was read, however.

Figure 2.3.4: Dr. Guoquan Wang et al. at the Blue well (left) demonstrating how to measure with the water meter, where the lip of the inner PVC pipe is measured (right).

The well's absolute coordinates were instead determined via GPS measurement and OPUS processing. The pipe lip's orthometric height, according to the North American Datum 1983 (NAD_83) is found by submitting onsite GPS coordinate data to OPUS (Figure 2.3.6). This finds ground elevation at the well site, and allows onsite measurement of added lip height above ground level. This orthometric well lip height is subtracted by measured well water depth levels to give absolute water level altitudes, catalogued in Section 5.1.

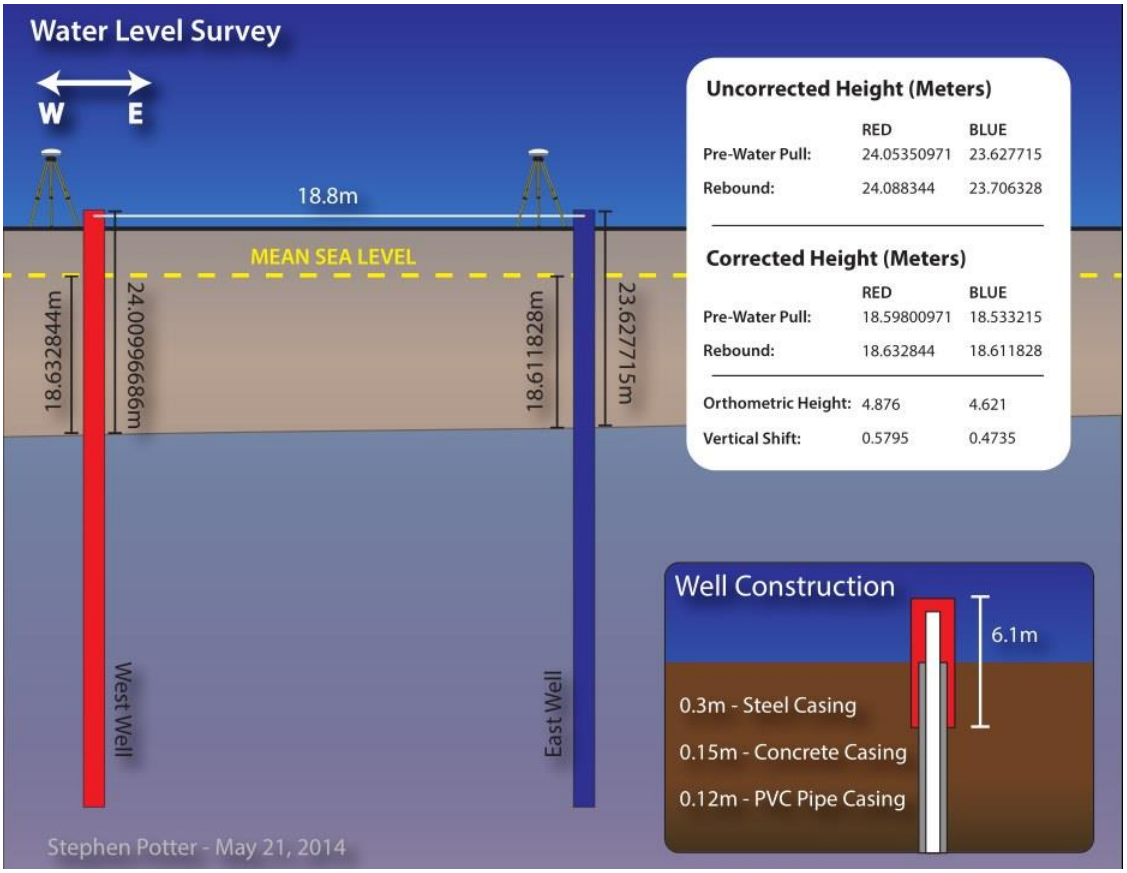

Figure 2.3.5: Well diagram, not to scale (Potter 2014). Note the height of well surface above mean sea level.

Regarding the automated well water data collection, an In-Situ Inc. Level TROLL 700 (Figure 2.3.7) is used at UHC3 for continuous monitoring of water level, water pressure, and temperature of the Gray well (In-Situ Inc. 2013). Well water depth is found by differencing barometric pressure of the air above water level and the water pressure underneath to determine water level above where the troll is placed. The entire instrument is housed and protected by a desiccant pack (Fig 2.3.7, bottom) that records groundwater-level data.

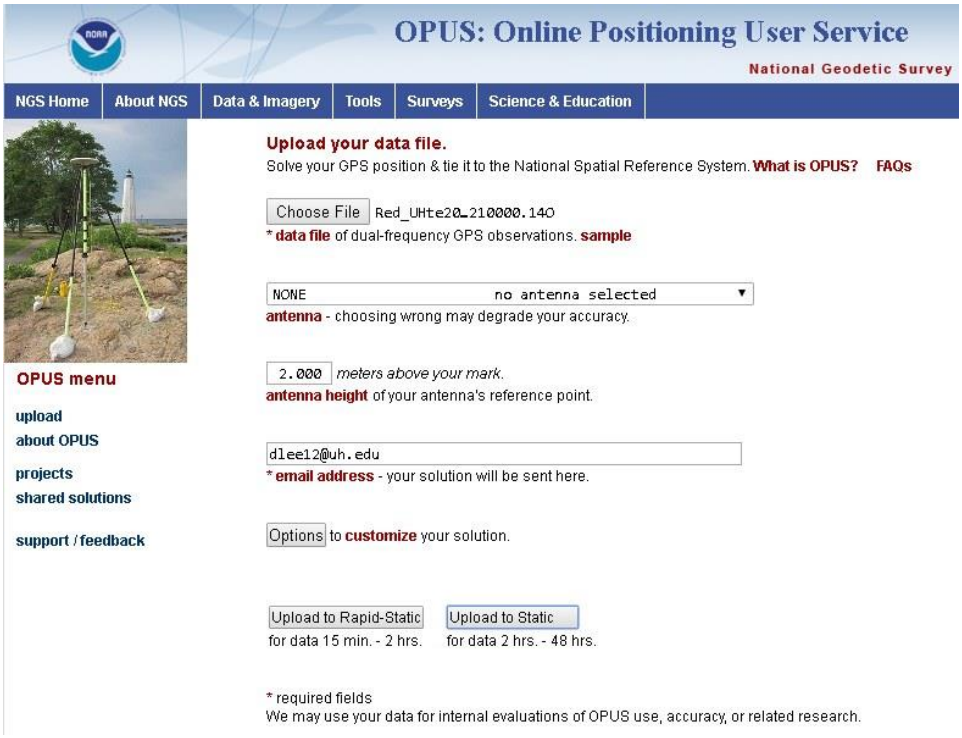

Figure 2.3.6: Online Positioning User Service (OPUS) website interface for uploading .o files for absolute positional GPS data (NGS 2016).

These measurements were all differenced by a set value on May 20th, 2014 for the manual measurements, and October 17th, 2015 for the automated well measurements; this creates the displacement time series to be juxtaposed with GPS displacement data (Section 5.2).

Figure 2.3.7: (top left) White metal cabinet placed at UHC3 to shelter the Level 700 TROLL components (top right) weighed down by concrete blocks. (bottom) The desiccant pack at left protects and houses the troll instrumentation.

3 GPS Measurements of Ground Displacement

3.1 Introduction

UHCC's antenna array has measured ground movement at 10, 20, and 30 feet below surface, with respect to a predefined 0 feet level; the antennas responsible for their respective layer positional measurements are designated UHC1, UHC2, UHC3, and UHC0. Using OPUS to unpack and convert the DAI catalogued data to RINEX, absolute latitudinal (northing), longitudinal (easting), and altitudinal (height) coordinates for each antenna at the array were compiled. Post-processing with TopCon Tools, a master table was saved in Microsoft Excel 2013, and the GPS displacement data were graphed on CoPlot to measure change over time in the position of one subsurface layer with respect to the surface layer.

Almost all subsurface displacements in this thesis are with respect to surface level (UHC0) itself shown to be moving. Figures 3.1.1 and 3.1.2, respectively, show the horizontal and vertical precise point positional (PPP) displacement time series of all four UHCC antennae. Thus for measurements in the following sections, "UHC1" is actually UHC1-UHC0, "UHC2" is actually UHC2-UHC0, and "UHC3" is actually UHC3-UHC0. As mentioned in Section 1.5, setting the most varying UHC0 as the reference frame allows us to more readily compare horizontal and vertical movements of the relatively closely behaving underground layers.

We have also tabulated the overall, two-year averaged coordinates and their standard deviations in Table 3.1.1. UHCC ground movement for every depth was monitored from February 18th, 2014, to February 1st, 2016. OPUS has processed horizontal positions in the Universal Transverse Mercator (UTM) geographic coordinate system, and vertical positions in the North American Datum, Year 1983 (NAD_83) Orthometric height. Vertical NAD83 Orthometric height in Table 3.1.1 is the height of the antenna head itself, not that of the concrete plug at each antenna's base (cf. Figure 2.1.2.10).

Table 3.1.1: GPS absolute coordinates of UHCC antennae (averaged 02/2014 – 02/2016).

Averages of	North(m)_UTM	East(m)_UTM	Vertical(m)_NAD83_OR
UHC1	3252972	301649	7.227
UHC2	3252973	301653	7.238
UHC3	3252973	301657	7.374
UHC0	3252973	301660	7.146
Averages of	Sigma-N(m)	Sigma-E(m)	Sigma-V(m)
UHC1	0.00868	0.0128	0.0140
UHC2	0.00857	0.0127	0.0138
UHC3	0.00842	0.0125	0.0134
UHC0	0.00803	0.0121	0.0136

From Figure 3.1.2, a downward trend of 1.5 ± 0.5 mm/yr of UHC0 at the surface, 1.9 ± 0.5 mm/yr of UHC1 at 10 feet bls, 2.6 ± 0.4 mm/yr of UHC2 at 20 ft bls, and 3.4 ± 0.4 mm/yr of UHC3 at 30 feet bls were observed. This inflating of the top layer whilst the entire aquifer is lowering in overall height may be cause for concern.

Although the overall positions of the layers are generally important, it is not the focus of this study; the aim of this study is to compare positional displacement (Section 3.2), especially vertical displacement trends (Section 3.3), with weather (Section 4) and groundwater (Section 5) data to determine the existence of any correlations amongst the three.

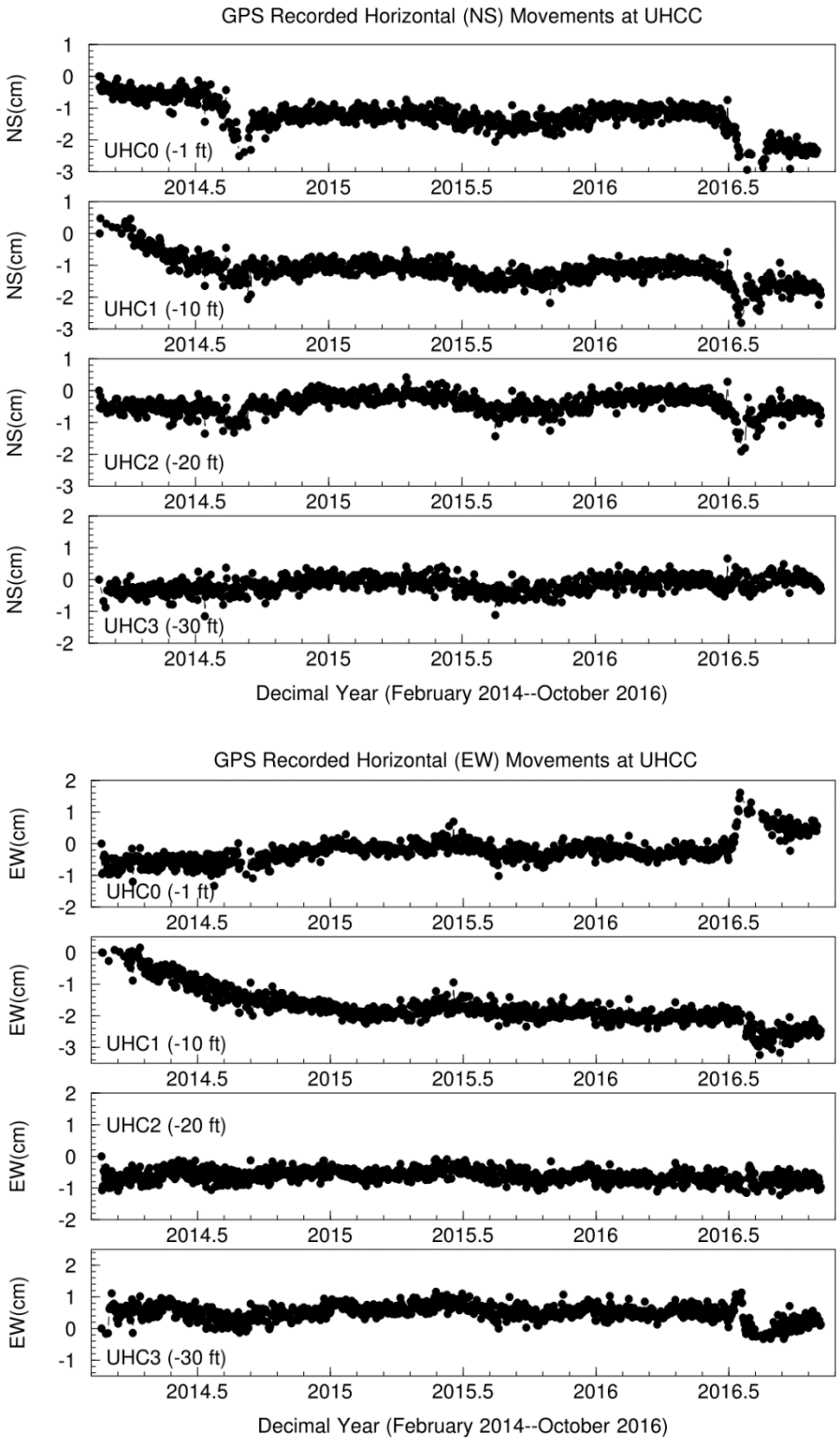

Figure 3.1.1: Horizontal movements of all four UHCC antennae over time (02/2014 – 10/2016). All measurements are precise point positioning (PPP). (top) North-South displacements where positive values are north. (bottom) East-West displacements where positive values are east.

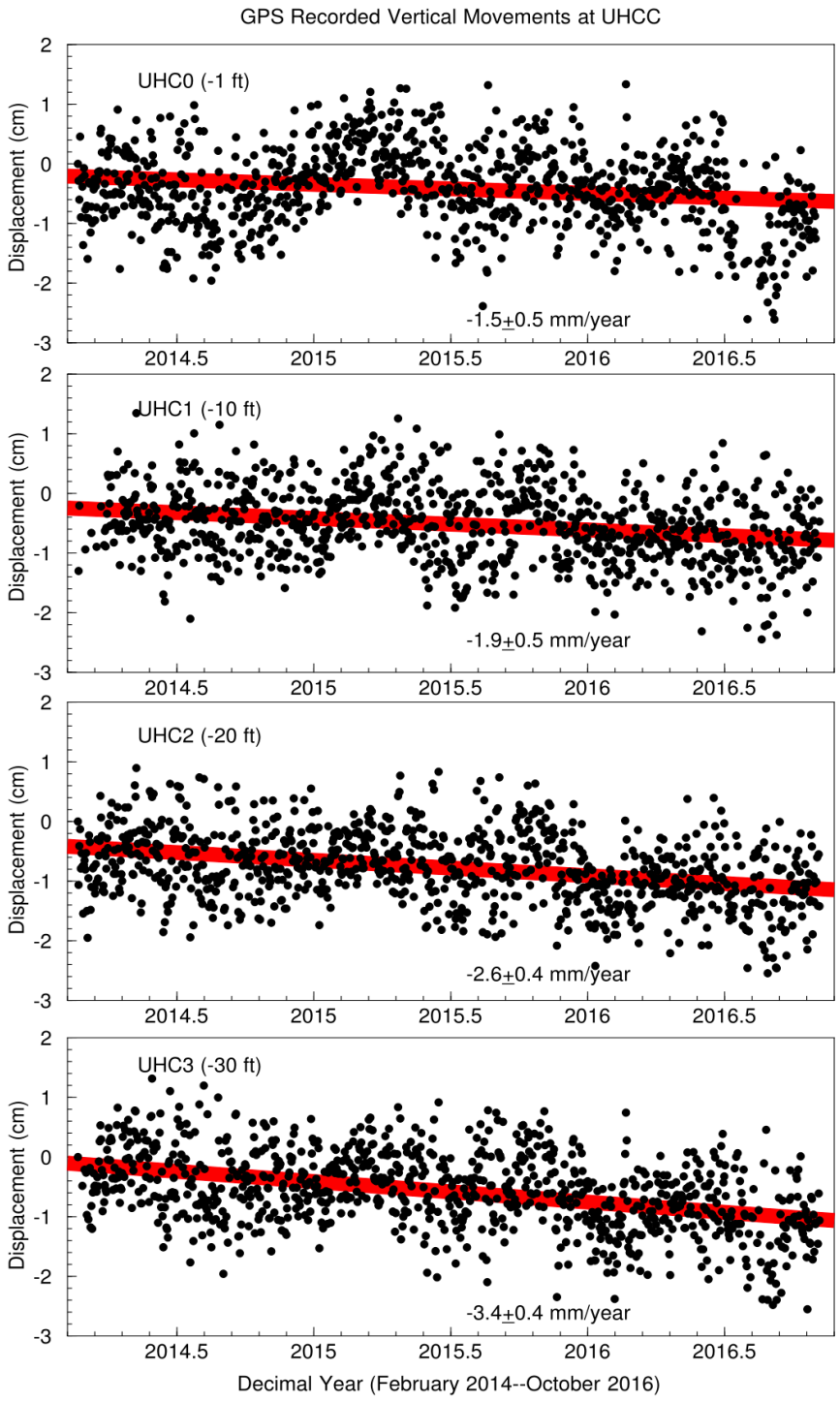

Figure 3.1.2: Vertical movement of all four UHCC antennae over time (02/2014 – 10/2016). All measurements are precise point positioning (PPP). Setting UHC0 as the reference point for the other three antennae throughout this thesis will provide a closer comparison of the differences between the subsurface layers' movements.

3.2 Displacement – Horizontal and Vertical

Before presenting and detailing the main body of data, some overlying quantities must be acknowledged, tabulated in Table 3.2.1. Here the calculated Northing, easting and height trends of each depth with respect to surface (dN, dE, and dH, respectively), and the horizontal (dN and dE) and vertical (dH) Root-Mean-Square values have been collected. In the following page in Figure 3.2.1, the full two-year northing-, easting-, and height-displacement time series have been plotted for all three stations. Movement trends under 2 mm/yr are disregarded. These displacement trends are with respect to UHC0 at ground surface level; thus a negative dH value of a subsurface layer means an equal positive dH value of the surface.

Table 3.2.1: UHC GPS measurement variables relative to UHC0 (02/2014 – 02/2016)

	dN (mm/yr)	dE (mm/yr)	dH (mm/yr)	Horz RMS (mm)	Vert RMS (mm)
UHC1	-1.1315	-11.461	-1.387	0.528979356	0.873694436
UHC2	4.7815	-2.336	-2.8835	0.52841662	0.87332507
UHC3	4.2705	-1.752	-3.65	0.535733617	0.890597163

At 10 feet underground (UHC1) linear analysis showed negligible southward and downward movement and an 11 mm/yr trend of westward movement relative to ground surface. Northing and easting RMS is 0.53 mm while height RMS is 0.87 mm. At 20 feet underground (UHC2) linear analysis showed a 5 mm/yr northward, 2 mm/yr westward, and 3 mm/yr downward (surfi-

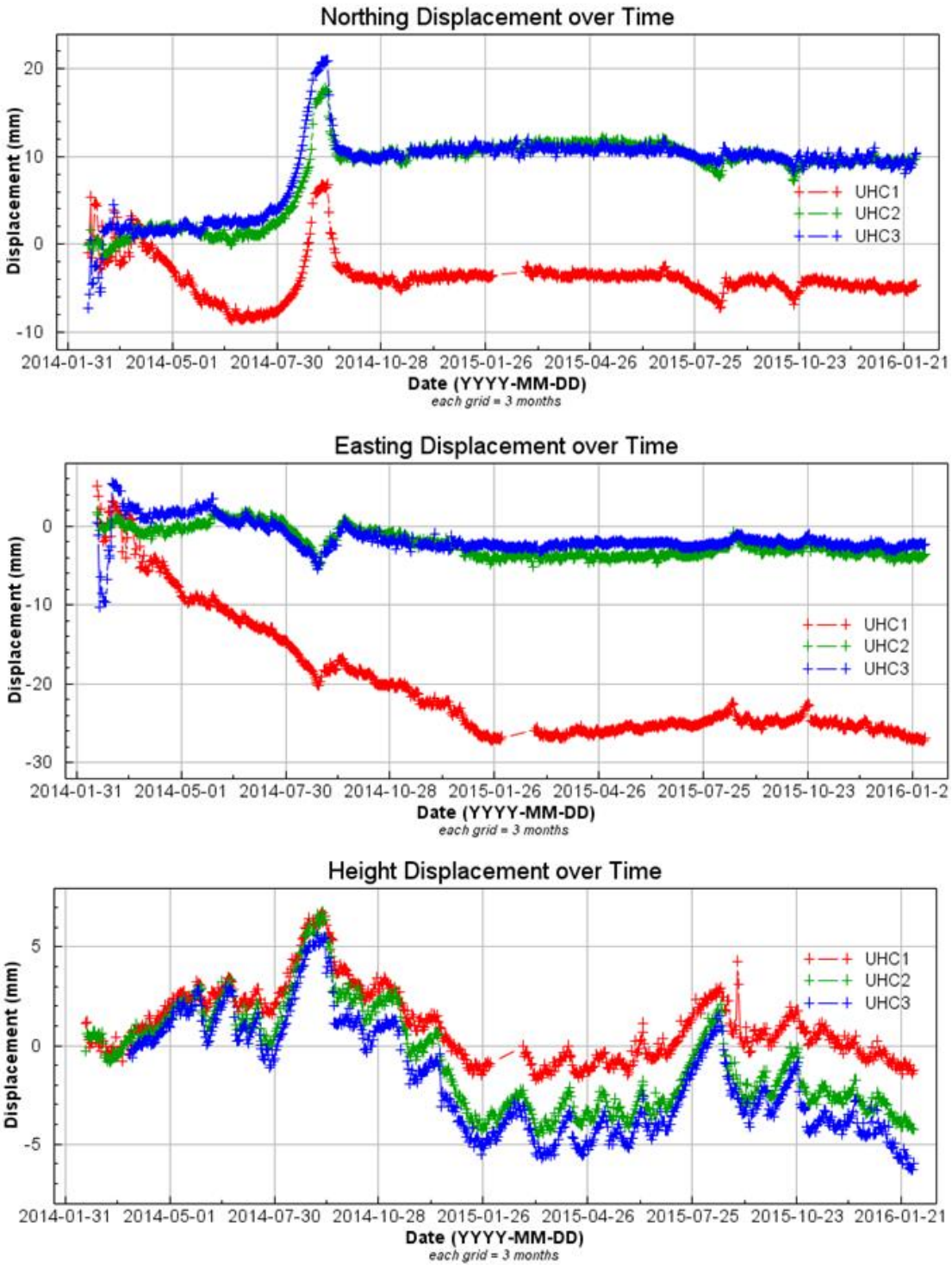

Figure 3.2.1: Northing-, easting-, and height-displacements over time. Measurements run for two years, from February 18, 2014, to Feb 1, 2016. Each antenna's measurement of displacement is with respect to UHC0, defined as "0 feet" (Table 3.2.1).

cial inflation) movement trends relative to the surface. Northing and easting RMS is 0.53 mm while height RMS is 0.87 mm. At 30 feet underground (UHC3) linear analysis showed 4 mm/yr trend of northward movement, negligible westward movement, and a 4 mm/yr trend of downward movement relative to surface, meaning inflation of the surface. Northing and easting RMS is 0.53 mm while height RMS is 0.87 mm.

However, horizontally, after the first year of the study, the three subsurface layers show almost no movement north- or southward from October of 2014 on, and likewise only negligible east-west movement after February of 2015. Vertically, between 0 to 20 ft the overall movement is 4 mm; between 0 to 30 ft, 7 mm. Thus, 0 to 10 ft, there is less than 2 mm inflation, 10 to 20 ft shows 3 to 4 mm inflation, and 20 to 30 ft has 3 mm inflation.

From February 18, 2014, to Feb 1, 2016, ground displacements from GPS data have been calculated and a set of graphs for each axis of movement have been created (Figure 3.2.1). Some points are missing for UHC1 from Feb 1st to Feb 28th, 2015, due to equipment error. For all directions, a similar behavior with UHC2 and UHC3's deeper foundation layers have been observed; however, in elevation change (Figure 3.2.1, bottom) the smaller Y-axis scale helps one more easily distinguish between the two readings. With horizontal movements (Figure 3.2.1, top and middle), two trends are made known: UHC1 deviating 15 mm more southward and 24 mm more westward than UHC2 and UHC3, and a common series of movement spikes through August and September 2014, and in August and October 2015. UHC1's unique southerly and westerly trends end by July

2014 and February 2015, respectively. From March of 2015, UHC1's displacement behaves much like those of UHC2 and UHC3.

Although there are many possible causes for this eccentric behavior for the first seven months of measurement, such as nearby shallow fluid extraction (within UHCC there are active hydrocarbon pumps less than a kilometer away from the array) and other projects and scientific investigations (conducted at the UHCC main building set on the same ground stratum as the UHC antenna array), the cause is more likely short-term natural ground deformation at the top level of the subsurface that have shearing action with the nearest layer at 10 feet. Some of the more negligible horizontal motions may not be real ground motions but instead the shift of the antennae poles within the pipe, which is much less constrained horizontally than vertically. What is more likely to effect the jumps common to all three layers is the reference layer itself—ground level—moving (Figures 3.1.1 and 3.1.2).

We differenced the UHC1, 2, and 3 displacements from each other (Figure 3.2.2), taring UHC1 displacement for northing at July 1, 2014 and easting at March 1, 2015. The northing spike still exists in August 2014, yet here UHC2 with respect to UHC1 (red) is more normalized, the difference between the two nearing zero. In fact, relative northing movements cease by November 2014, and relative easting movements become very stable from mid-January 2015 onward. More important than these horizontal anomalies, however, are the vertical changes (next subsection).

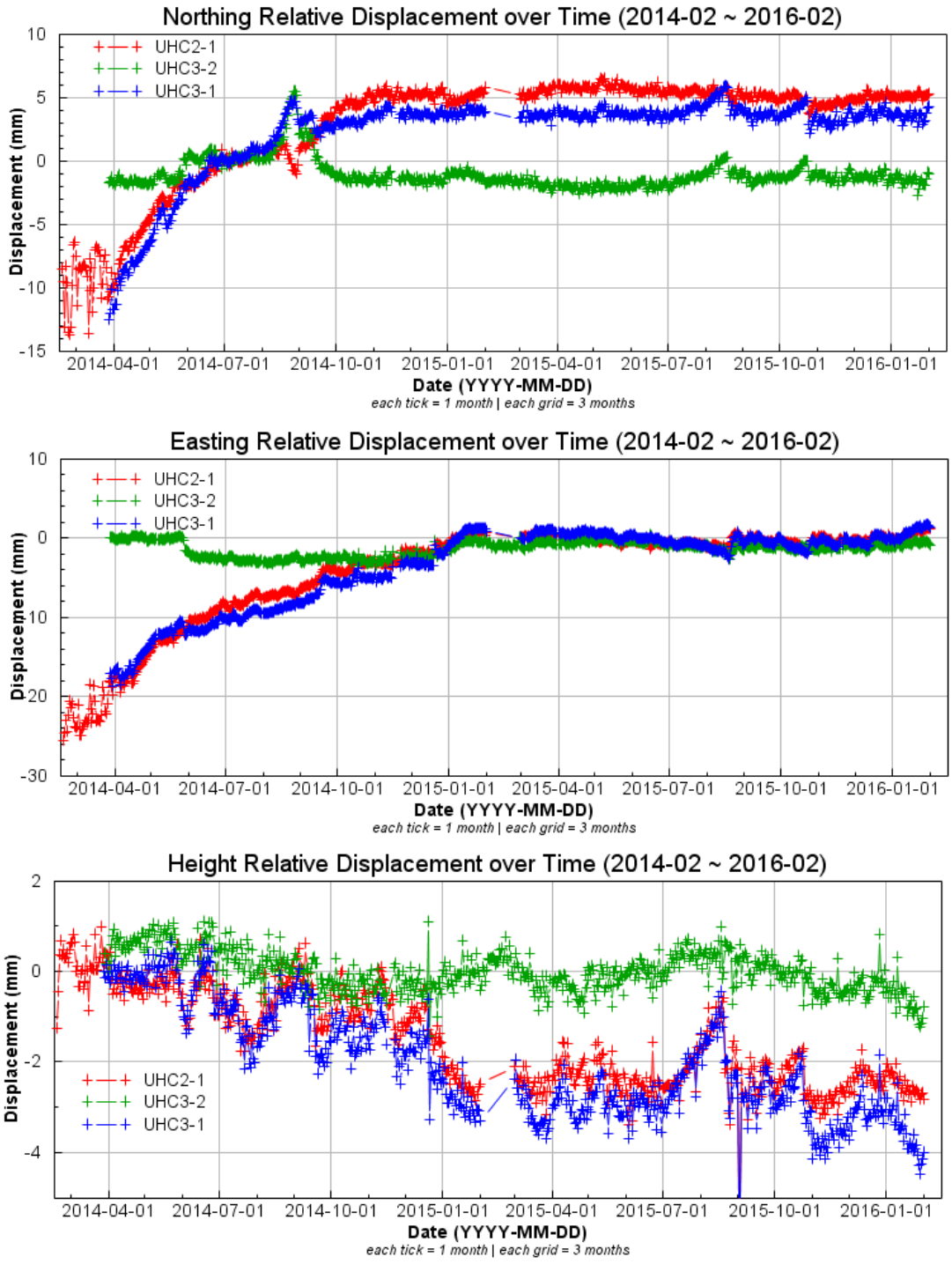

Figure 3.2.2: Northing-, easting-, and height-displacement time series for subsurface layer movements relative to one another. Measurements run from February 18, 2014, to Feb 1, 2016. (Table 3.2.1). N is zeroed at the northing measurement of each station on Jul 1, 2014; E is zeroed at the easting measurement of each station on at Mar 1, 2015; H is tared at the height measurement of each station on Apr 1, 2014.

3.3 Vertical Displacement

With Figure 3.3.1, the focus is more on height and elevation changes of the subsurface layers only; the top graph shows the entire 2-year set of vertical displacements from February 2014 to February 2016, the middle graph shows the first year's movements from February 2014 to February 2015, and the bottom graph shows those of the second year of observation from February 2015 to February 2016.

We want to focus on two features of UHC1's, UHC2's, and UHC3's graphs: where there are sudden drops in elevation, and where there are higher magnitudes of vertical change. In Figure 3.3.2, the focus is on the first year (top) looking at different parts: a relatively high magnitude uplift (with respect to the surface) from July 15th to September 15th, 2014 (Figure 3.3.2.I), the first month of that timeframe (Figure 3.3.2.II), a five month subsurface drop relative to surface from September 1st, 2014, to Febrary 1st, 2015 (Figure 3.3.2.III), and a 50 day section from Dec 17, 2014, to Feb 5, 2015 (Figure 3.3.2.IV).

With Figure 3.3.2.I, a 5 to 7 mm positive change in relative height is shown. Error for each double-differenced data point (UHC1-UHC0, UHC2-UHC0, UHC3-UHC0) is sub-millimeter. At this point, the numerous details are simply taken note of and assumptions are left for after all the findings are catalogued. Within that time, Figure 3.3.2.II looks more closely at the initial minima in displacement, where concavity is less severe at 10 than 20 or 30 feet.

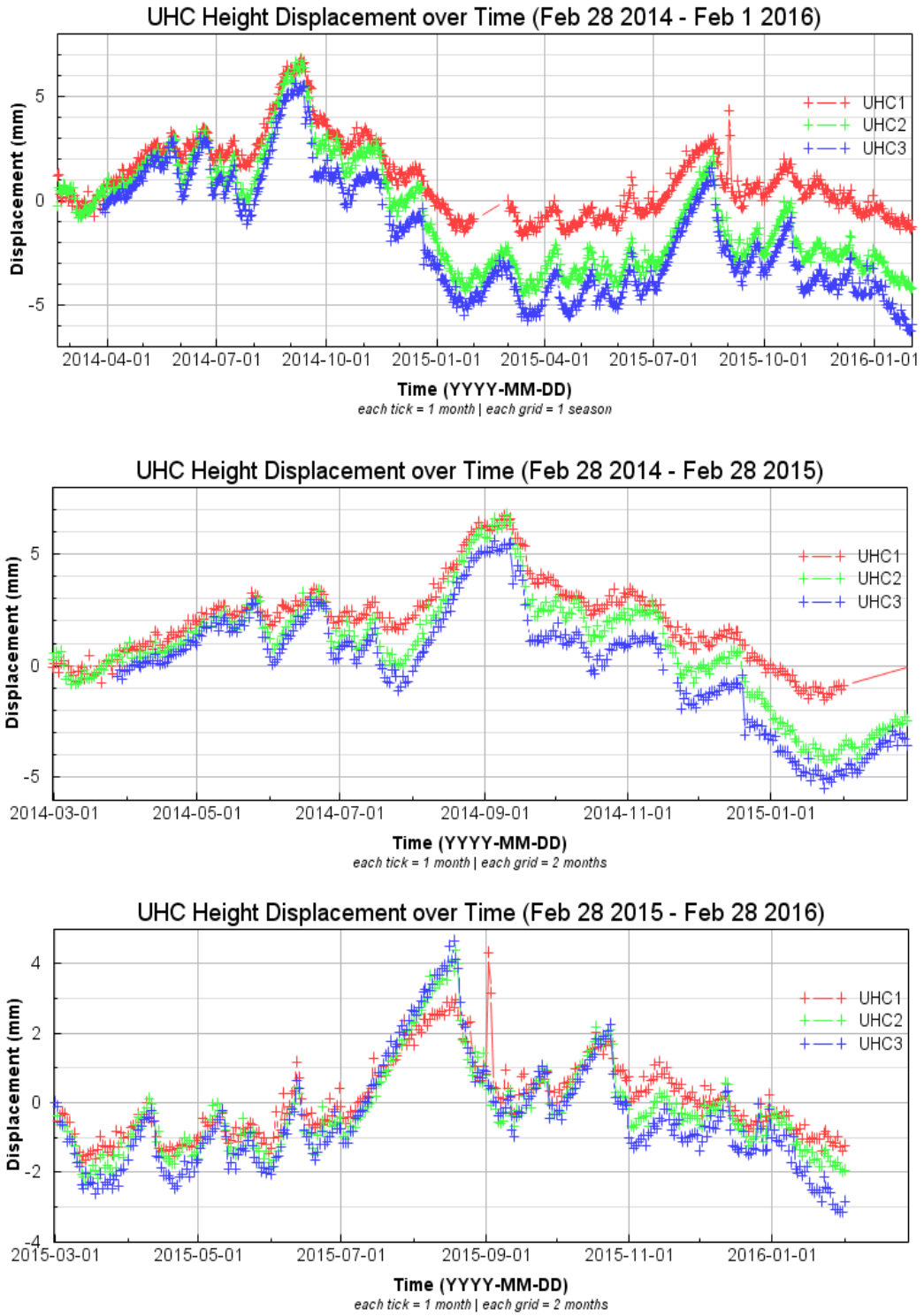

Figure 3.3.1: Height displacements only, over two years at the UHC antenna array. (top) Displacement over Feb 2014 - Feb 2016. (middle) Displacement from Feb 28, 2014, to Feb 28, 2015. (bottom) Displacement measured from and tared at Mar 1, 2015 to Feb 1, 2016.

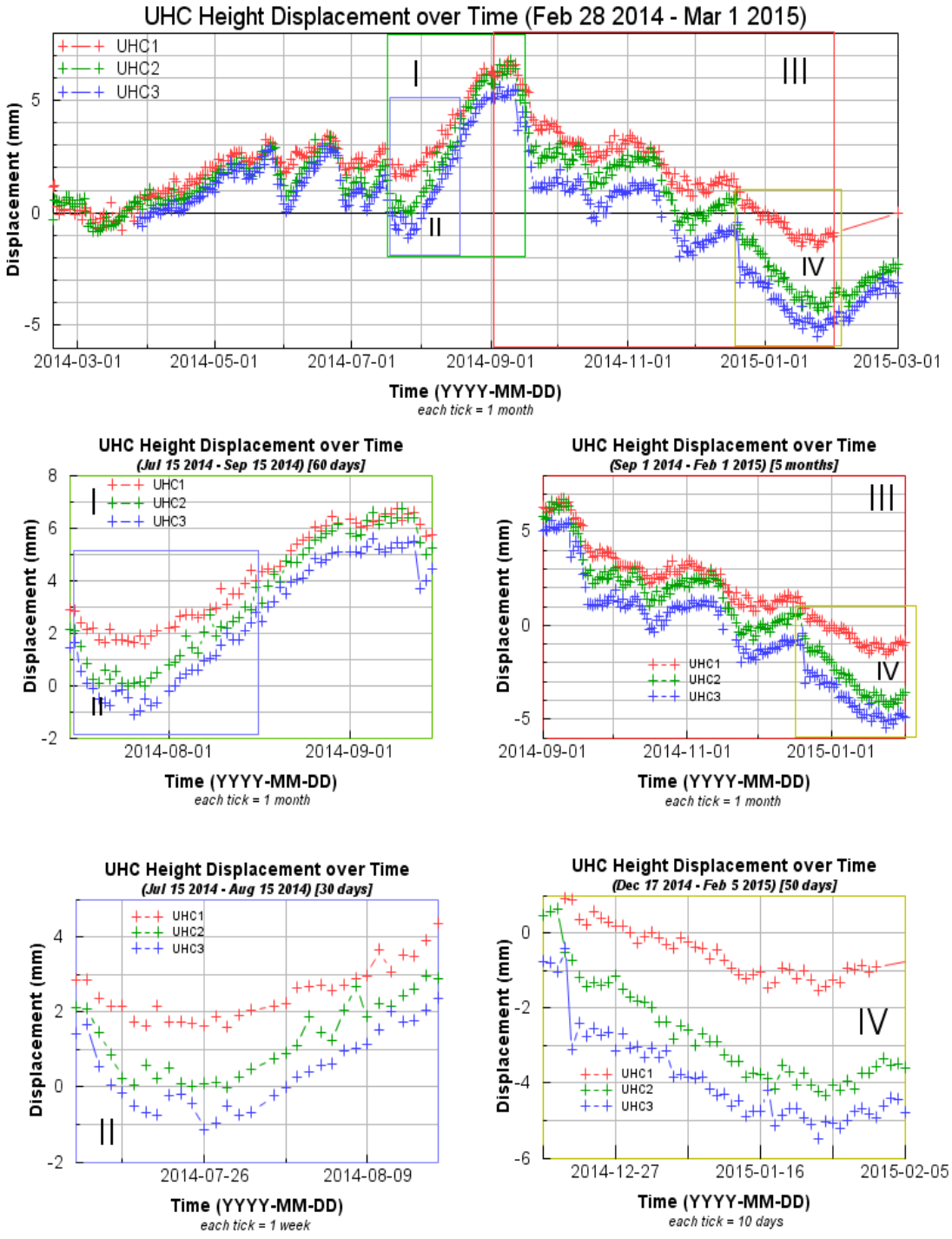

Figure 3.3.2: (top) Height displacement measurements of the UHCC antenna array over the first year, from Feb 28, 2014, to Mar 1, 2015. (middle left, I, green outline) A two month section of 2014, from Jul 15 to Sep 15, (bottom left, II, blue outline) a one month section of 2014, from Jul 15 to Aug 15, (middle right, III, red outline) a five month section, from Sep 2014 to Feb 2015, (bottom right, IV, gold outline) and a 50-day section from Dec 17, 2014, to Feb 5, 2015.

Figure 3.3.2.III was chosen for not only the displacement range of 8-11 mm, but also the regularity of sudden drops, at around Sep 15, Nov 15, Dec 15, and arguably Oct 15; in other words, on the ides of September through December of 2014. Yet again in Figure 3.3.2.IV, the most noticeable elevation change is in the middle layer of UHC2. From a local maximum around December 21st, 2014, to the local minimum around January 24th, 2015, UHC1 encounters a 2 mm drop, UHC2 encounters a 3 mm drop, and UHC3 also encounters a 3 mm drop.

Looking into the second year of displacement, Figure 3.3.3 rezeroes at March 1st, 2015, to finish off the data ending at February 1st, 2016. The top graph shows height displacement over the entire second year. This year's data has three distinct seasons: (Figure 3.3.3, middle, cyan) a 4-month "spring" season from March 1st to July 1st in 2015, (Figure 3.3.3, bottom left, magenta) a 3-month "summer" season from July 1st to October 1st in 2014, and (Figure 3.3.3, bottom right, yellow) a 3-month "autumn" season from Oct 15, 2015, to Jan 15, 2016.

"Spring" experienced four sudden drops almost invariably in the middle of each month.These elevation displacement drops of 1 to 2.5 mm occur in a span of 4 to 13 days (Figure 3.3.3, middle). This almost consistent, relatively high occurrence of sudden drops could prove fruitful in correlating with rainfall data during this wet spring season. "Summer" experienced a 3.5 to 6 mm rise in elevation of the subsurface layers with respect to ground layer (Figure 3.3.3, bottom left); the two outlier UHC1 data points for Sep 2 and 3 are too different for consideration. This "uplift" may be summer temperatures evaporating and co-

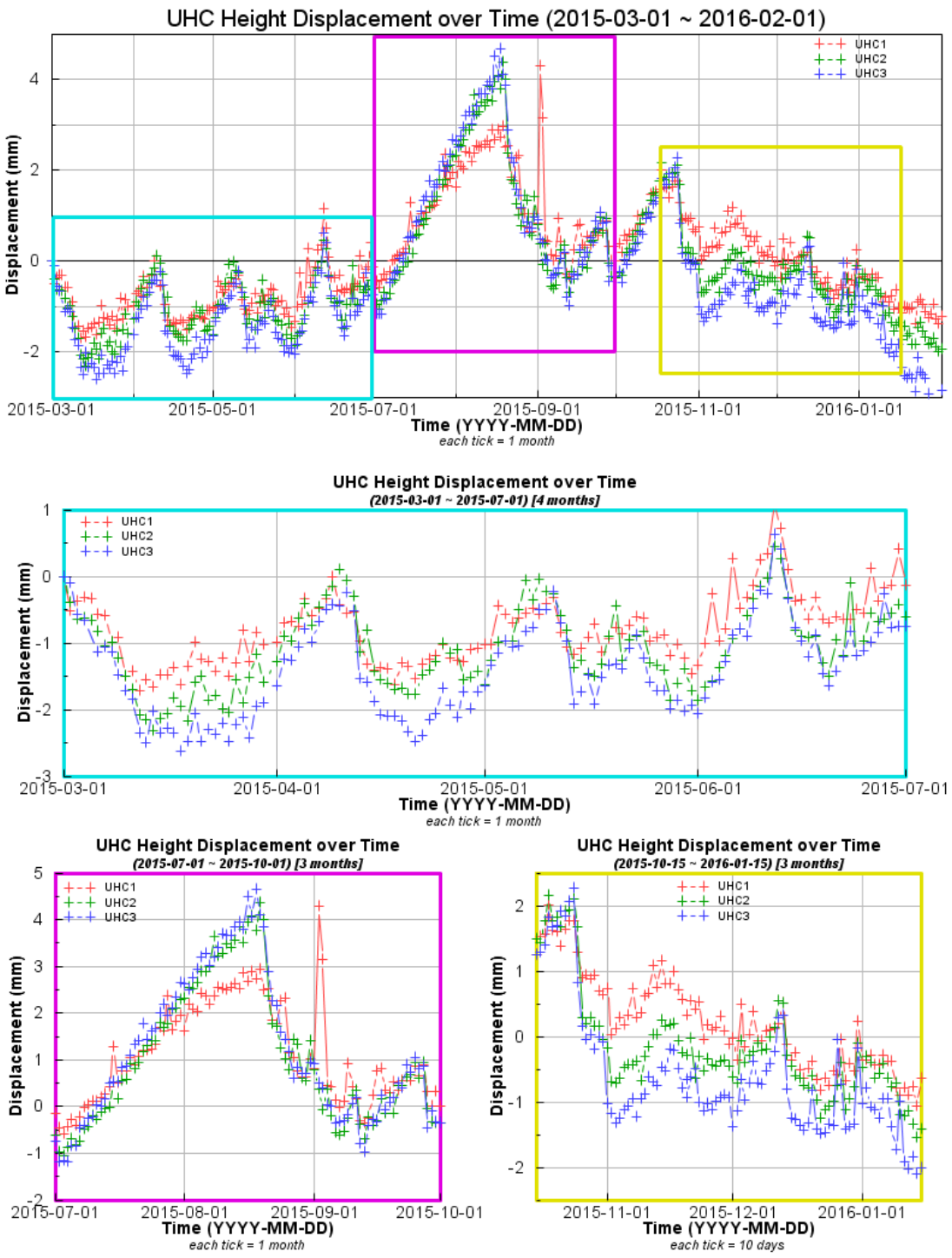

Figure 3.3.3: (top) Height displacement over the second year, from Mar 1, 2015, to Feb 1, 2016. (middle, cyan outline) A 4-month “spring” season of Mar-Jul 2015. (bottom left, magenta outline) A 3-month “summer” season of Jul-Oct 2014. (bottom right, yellow outline) A 3-month “autumn” season from Oct 15, 2015, to Jan 15, 2016.

mpacting shallower layers more so than with the deeper layers. Additionally, the sudden 2.5 to 4 mm drop in the second half of August 2015 is noted. Lastly, for “autumn” (Figure 3.3.3, bottom right) initially at the end of October a 2-step staggered height displacement drop of 2 to 3.6 mm over 10 days is seen. The rest of the season has a relatively steady rate of downward displacement of 1 mm per month.

In the next section, weather phenomena (specifically daily rain accumulation and day-averaged changes in air pressure, humidity, and dry temperature) is overlaid upon Figure 3.2.1’s NEH graphs among others to ascertain any correlations between weather and ground movement. In the subsequent section, well-groundwater level displacement data is in kind superimposed on Figure 3.3.1’s height displacement over the two year time period.

4 Weather and Rainfall

4.1 Introduction

Weather quantities were gathered at the UHC0 antenna site with the Vaisala WXT520 Weather Sensor Antenna (Figure 2.2.1, left), from April 17th, 2014, to February 1st, 2016. Among the different phenomena measured, air pressure, humidity, and dry temperature were retained, and rain accumulation was specially considered. Section 4.2 will show daily accumulated rainfall and compare them to both NEH graphs and height-only displacements. Section 4.3 will show the same displacement graphs with weather time series superimposed; these will show temporal changes in pressure, humidity, and temperature. In each section, it will be discussed whether or not there seem to be correlations with the appropriately scaled weather quantities and the ground layer displacement data.

All weather data were collected at one minute intervals for the entire day, listing 1440 total lines of measurements. Rain was measured cumulatively in units of 0.1 mm, whereas the other quantities of pressure (millibars or “mb”), dry temperature (degrees Celsius or °C), and humidity (% or 0.01) were measured for the corresponding minute. Keyboard macros were used to sum rainfall and to average pressure, humidity, and temperature for every .m file, and to collect each row of data into a single database. Pressure, humidity, and temperature are differenced by the first value to obtain the *change* in pressure (dPR), humidity (dHD), and dry temperature (dTD) and matched with NEH displacements.

4.2 Rainfall

As introduced in Section 4.1, rain data was accumulated for each day per file and added to a compilation of precipitation over a time series (Figure 4.2.1). Daily rainfall in millimeters for all three graphs is shown, and yet a sizeable portion of the data has rainfall on the order of centimeters (Figure 4.2.1, top), so the rainfall dataset has been scaled before contrasting it with that of ground layer displacement in later sections. The cutoff of 0.1 mm in the bottom graph of Figure 4.2.1 was done to hide dry days of 0 mm rain. It is easier to recognize periods of rain absence rather than rain presence, so Aug. 2014, Feb. 2015, Jul. 2015, and Oct. 2015 distinguish themselves as months of little precipitation.

Once a histogram of rain has been emplaced on top of the displacement time series (Figure 4.2.2), it became evident that the precipitation series had to be rescaled to compare with the sub-centimeter height displacements (Figure 4.2.2, bottom); thus rainfall is graphed in unit centimeter (for each day), and shown on both sides of the horizontal axis by including negated precipitation data (-cm/day). This effort was made to allow better visual understanding of the relation between ground movement on both positive and negative values and rainfall accumulation.

Northing (Fig 4.2.2, top) and easting (Fig 4.2.2, middle) displacements seem largely unaffected by rainfall, though in mid-September of 2014, sustained rainfall corresponded to a 20 cm southward jump. The more promising relationship seems to be vertical movements in accordance with sessions of sus-

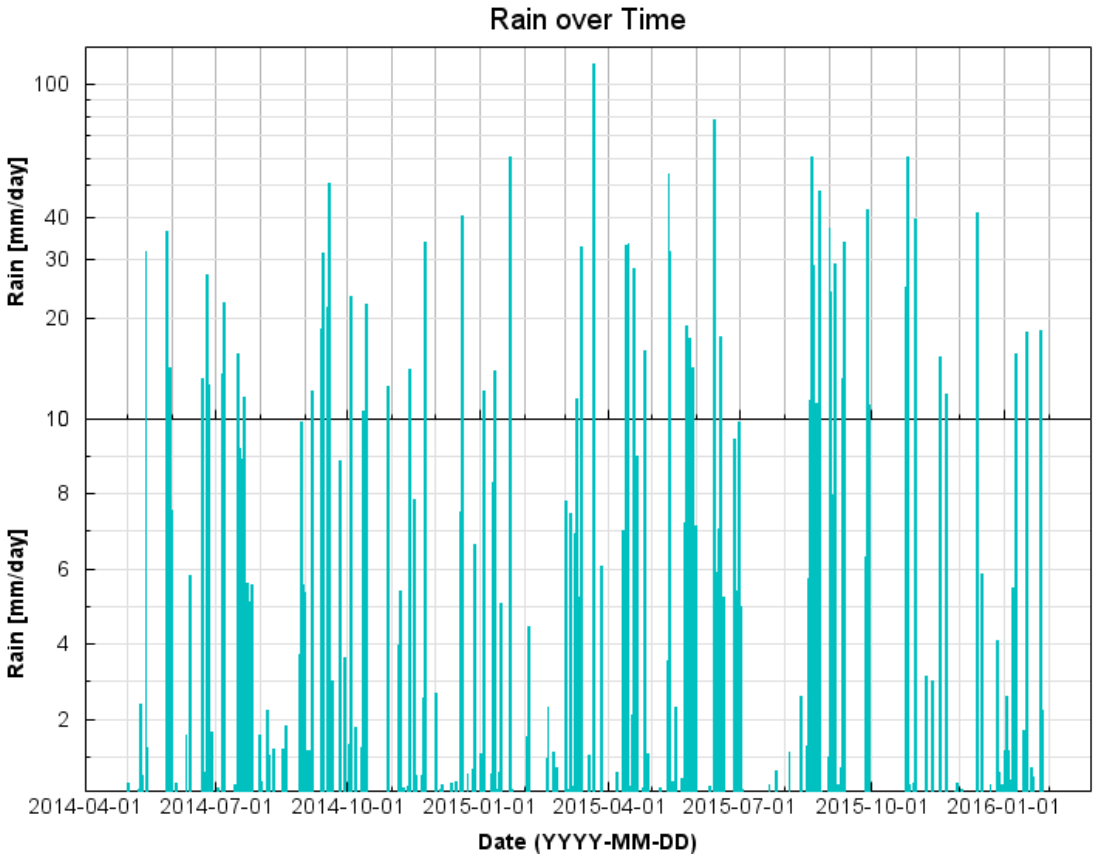

Figure 4.2.1: Accumulated precipitation in mm per day, from April 2014 to February 2016. Cutoff at 1 cm, (top) >1cm log scale graph and (bottom) <1cm linear scale graph.

tained rain (Fig 4.2.2, bottom). This height displacement graph is highlighted at the top of Figure 4.2.3, and unevenly divided into the first year (middle), and the second (end), the latter of which is re-tared at March 1st, 2015.

For every sudden drop in relative elevation displacement there is a significant accumulation of rain, represented by black bars in the top graph of Figure 4.2.3. No matter the magnitude of the height displacement, every one of its notably sudden shifts correspond to substantial precipitation dates. From Figure 4.2.3 the two-year height change (top), the first year (middle), and the second, re-zeroed year (bottom) are shown. The first year is examined more clo-

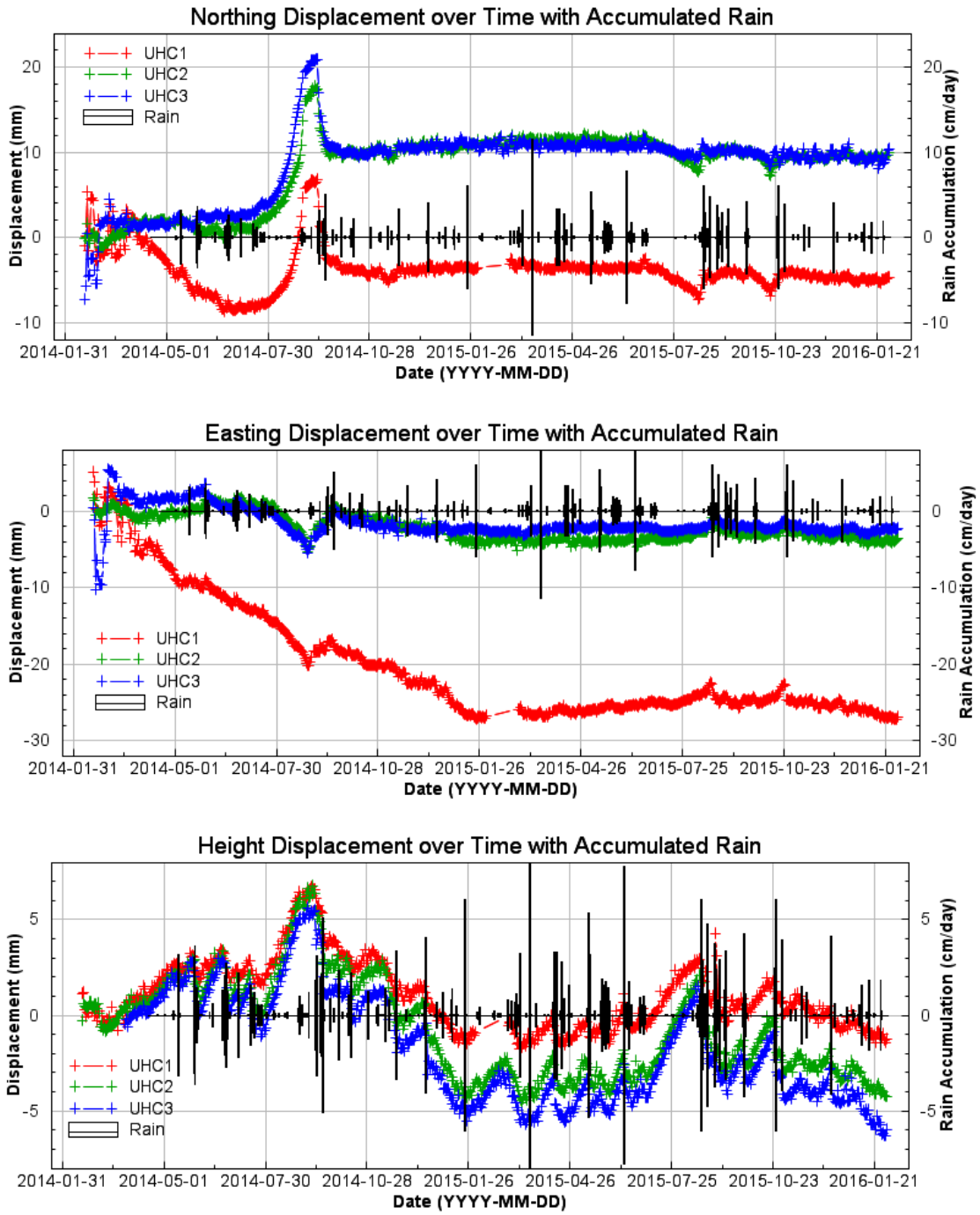

Figure 4.2.2: Double-sided daily rain accumulation histogram, overlaid upon Figure 3.2.1's (top) northing, (middle) easting, and (bottom) height displacements, measured from April 17th, 2014, to February 1st, 2016. Note that positional displacement is in millimeters while rain accumulation is in centimeters per day for scale; shown on both sides of axis for easier comparison with negative ground displacement values.

sely in Figure 4.2.4, and likewise the second year is stressed in Figure 4.2.5.

Figure 4.2.4 is simply the rainfall histogram on top of Figure 3.3.2. Over the same span of February 2014 to March 2015, a two month section of 2014, from Jul 15 to Sep 15 (middle left, I, green outline) and a five month section, from Sep 2014 to Feb 2015 (middle right, III, red outline), are shown. From those two sections, a one month sub-section of 2014, from Jul 15 to Aug 15 (bottom left, II, blue outline) and a 50-day section from Dec 17, 2014, to Feb 5, 2015 (bottom right, IV, gold outline) were examined, respectively.

In Figure 4.2.4.I, a lack of rain occurs during the local uplift of the subsurface. In Figure 4.2.4.II, the <2 cm rainy days that preceded the focal point of relative vertical movement can be seen. In Figure 4.2.4.III, rainfall greater than 2 cm a day generally is seen to correlate well to inflation of the surface. Note the continual rainfall in the middle of September 2014 where the greatest drop in height occurred. This graph also features a subsection shown in Figure 4.2.4.IV, where a high magnitude of rain accumulation on January 22nd, 2015, caused no relative change in ground layer height. This single rainy day may support the notion that although in general over 2 cm of rain a day induces a sudden height change, the magnitude of rain accumulation for a given day is less important than the sustained length of days that experience precipitation, which coincide with noticeable inflation of the surface. It is both substantial magnitude of rainfall (>2 cm/day) and sustained continuity of precipitation that can expectedly cause ground deformation.

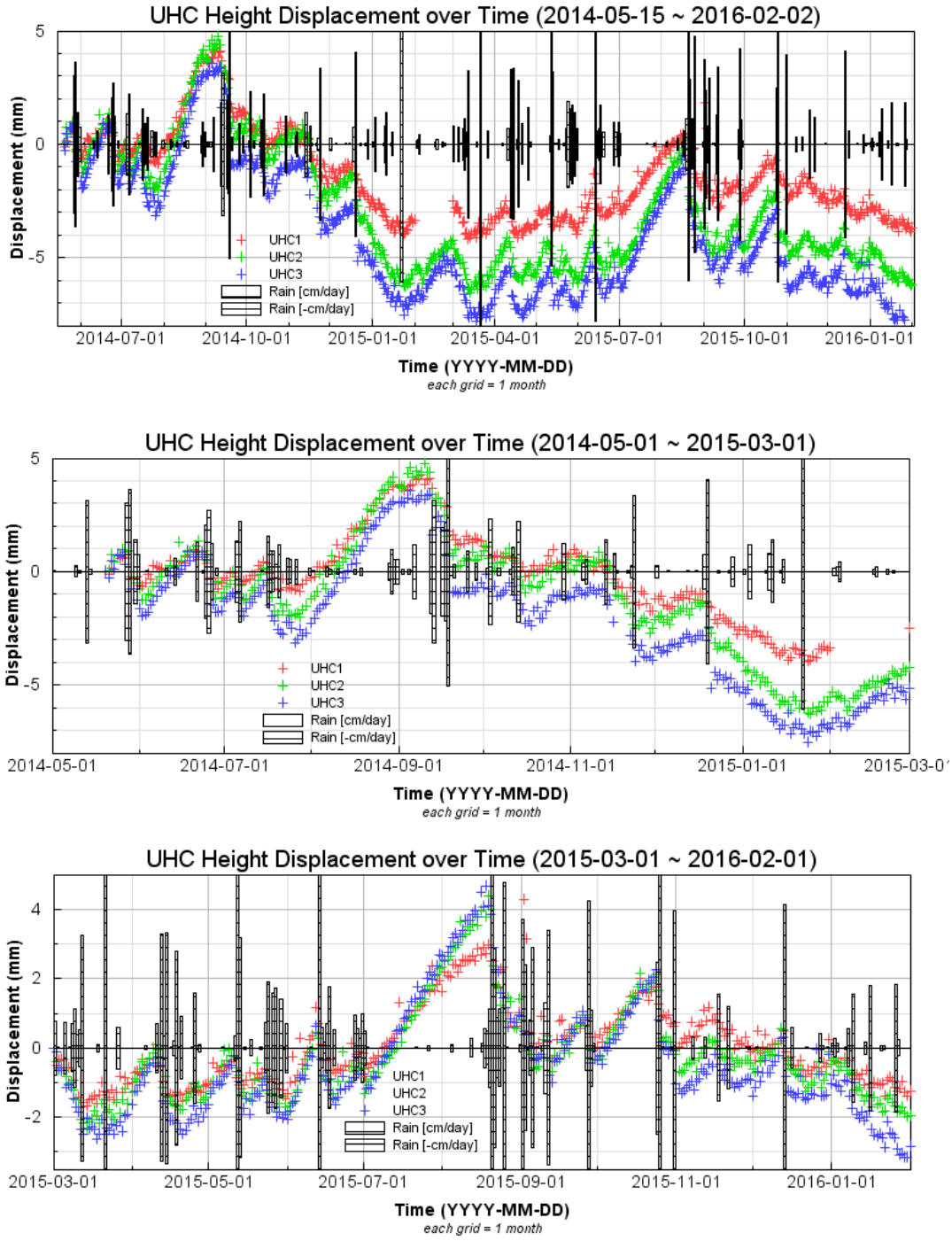

Figure 4.2.3: Daily precipitation histogram superimposed on Figure 3.3.1's Height-only displacement data. The histogram juts out of both sides of the horizontal axis for the entirety of the measurement timeframe (top), the first 12-month period of 2014-2015 (middle), and the last 12-month period of measurement in 2015-2016 (bottom).

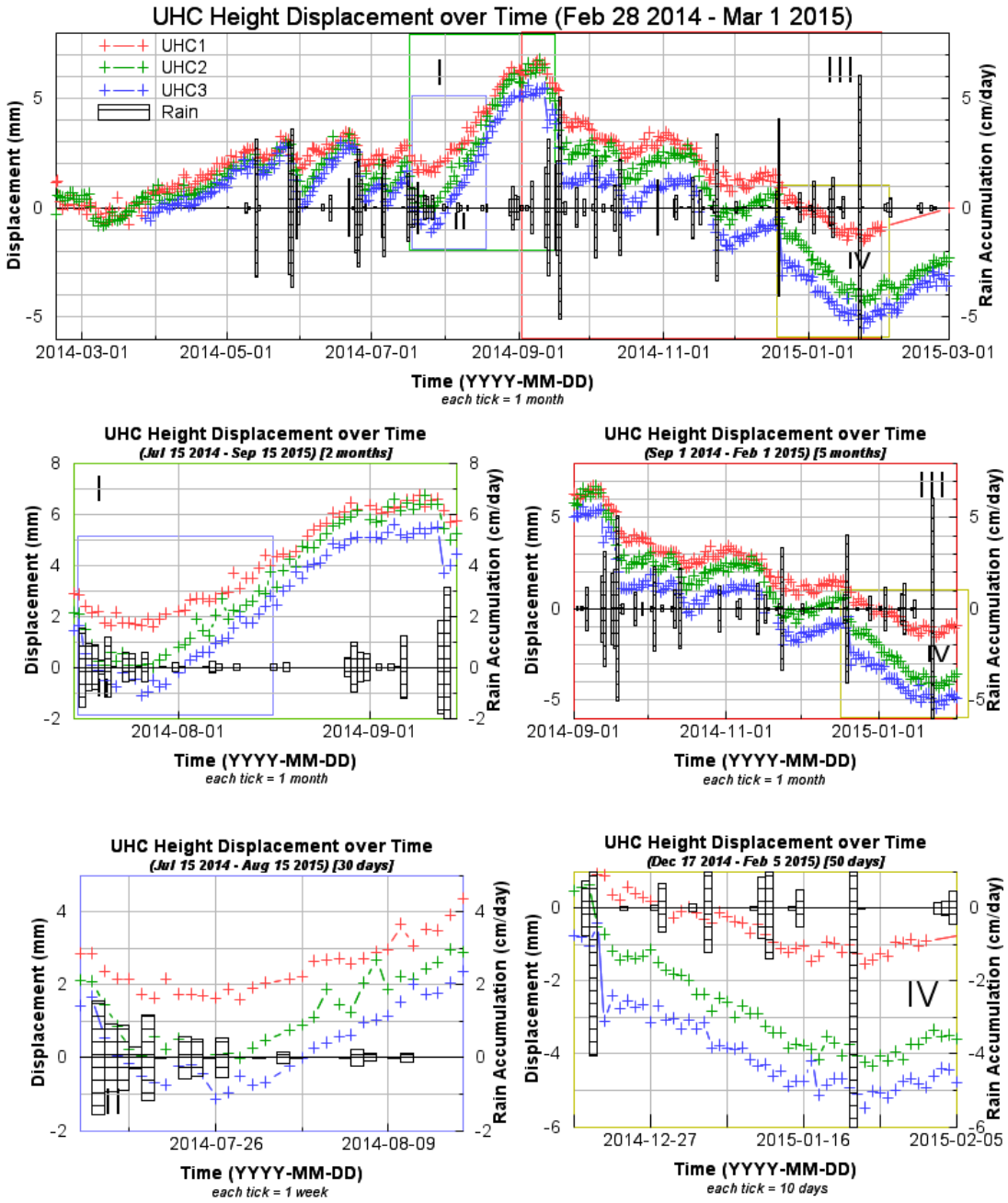

Figure 4.2.4: Daily accumulated precipitation in cm/year overlaid on Figure 3.3.2 over the first year of measurements from Feb 28, 2014, to Mar 1, 2015. (middle left, I, green outline) A two month section of 2014, from Jul 15 to Sep 15, (bottom left, II, blue outline) a one month section of 2014, from Jul 15 to Aug 15, (middle right, III, red outline) a five month section, from Sep 2014 to Feb 2015, (bottom right, IV, gold outline) and a 50-day section from Dec 17, 2014, to Feb 5, 2015.

For the second half of the two-year study of ground movement versus rainfall, Figure 4.2.5 was created by adding daily accumulated rainfall data in cm/yr over Figure 3.2.4. Top graph still shows height displacement over the second year, from Mar 1, 2015, to Feb 1, 2016; middle graph in the cyan outline has the 4-month “spring” season of March to July 2015; bottom left in a magenta outline is the 3-month “summer” season of July to October 2014; and at bottom right, the yellow-outlined graph is of the 3-month “autumn” season from Oct 15, 2015, to Jan 15, 2016.

Figure 4.2.5's "spring" exhibits both high rainfall (2 to 12 cm/day) and high continuity (up to 4 days of near-continual, >1 cm/day of rain). Nevertheless, from this it is still difficult to obtain a concrete relation between the number of near-continuous >1 or >2 cm/day precipitation dates and inflation of the surface. All that is certain is the general trend that periods of rainfall cause the surface to rise, and that dry periods permit surface compaction. This trend is true with Figure 4.2.5's "summer" where the 3.5 to 6 mm of underground uplift transpires in the drought period, and expected lowering of the subsurface relative to ground level subsequently follows during the rainy week in the middle of October 2015. Lastly, the "autumn" of 2015-2016 at the tail end of this study timeframe shows high-magnitude rainfall on dates of abrupt-surficial inflation.

To reiterate a previous point, substantial rainfall of over two centimeters per day causes abrupt changes in ground layer height, and sustained precipitation causes greater overall subterranean level change relative to the surface. In the next subsection, displacement versus other weather phenomena

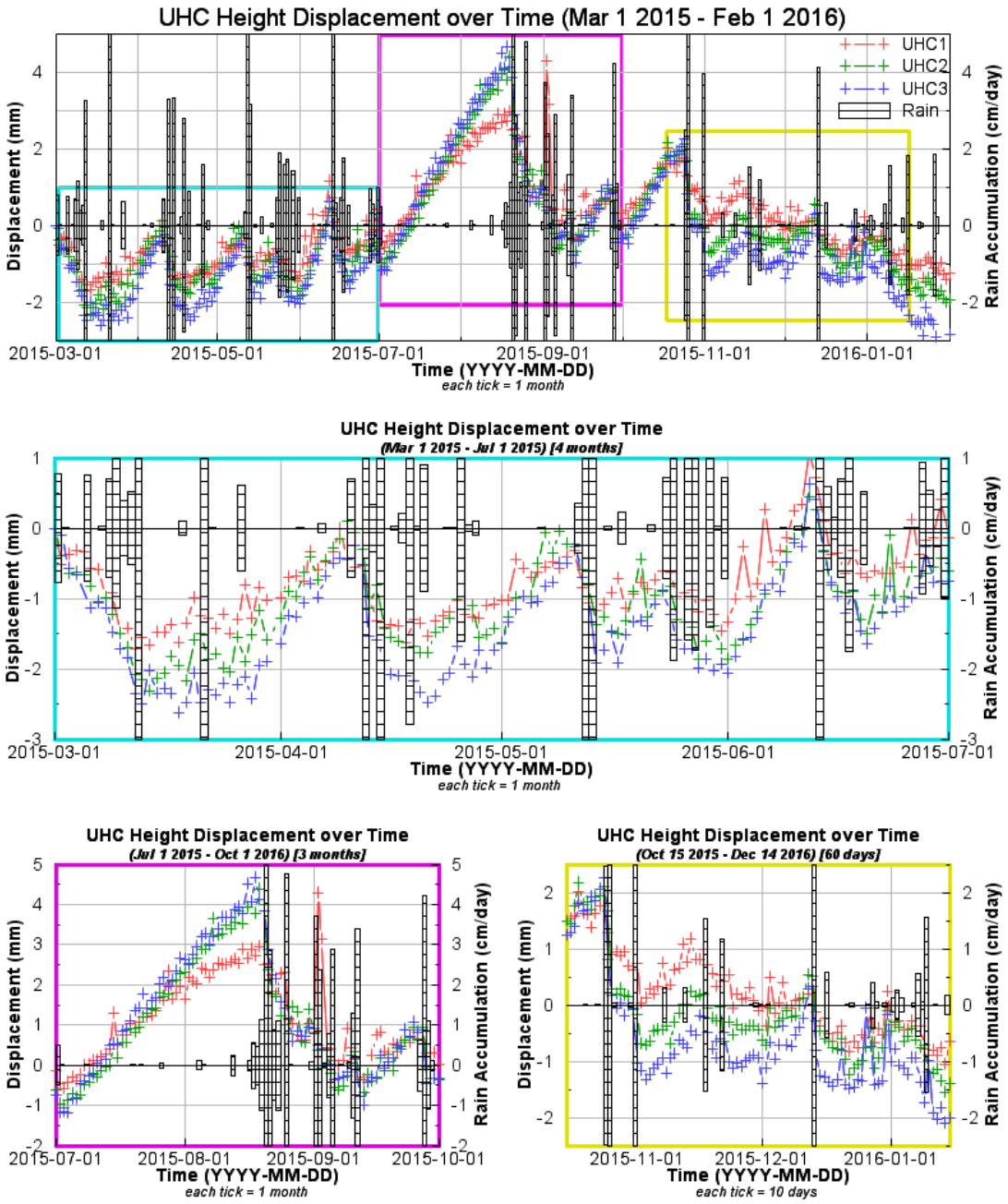

Figure 4.2.5: Daily accumulated precipitation in cm/yr emplaced over Figure 3.3.3. (top) Height displacement over the second year, from Mar 1, 2015, to Feb 1, 2016. (middle, cyan outline) A 4-month “spring” season of Mar-Jul 2015. (bottom left, magenta outline) A 3-month “summer” season of Jul-Oct 2014. (bottom right, yellow outline) A 3-month “autumn” season from Oct 15, 2015, to Jan 15, 2016.

trends will be shown, specifically pressure, humidity, and temperature of the air.

4.3 Pressure, Humidity, Temperature

Figure 4.3.1 shows northing-, easting-, and height-displacements matched to changes in pressure (left) and humidity (right) over time, from February 2014 to February 2016. Figure 4.3.2 shows the same NEH subsurface movement juxtaposed to dry temperature of the air over the same time period. As with rain, the values for pressure, humidity, and dry temperature were measured and recorded by the Vaisala Weather Sensor at UHC0's antenna site.

To match magnitudes for comparison, every unit in the Y-axis corresponds to 1 millimeter for relative ground layer displacement (all three figures), to 3 millibar for pressure change (Figure 4.3.1, left), to 10% for humidity change (Figure 4.3.1, right), and to 2 degrees Celsius for dry temperature change (Figure 4.3.2). This highlighted the lack of correlation between the notable changes of horizontal or vertical position of underground layers with respect to surface, and both pressure and humidity changes in the air; only temperature has a trend that even resembles the raising and lowering of the subsurface depths with respect to the top ground layer. Because the temperature time series expectedly follows northern hemispherical seasonal patterns, the nominal correlation gathered from the other weather data is that falling temperatures bring rain, thus relative lowering of the subsurface (which is inflation of the surface), and rising temperatures bring dry periods, thus relative subsurface rising (which is compaction of the surface).

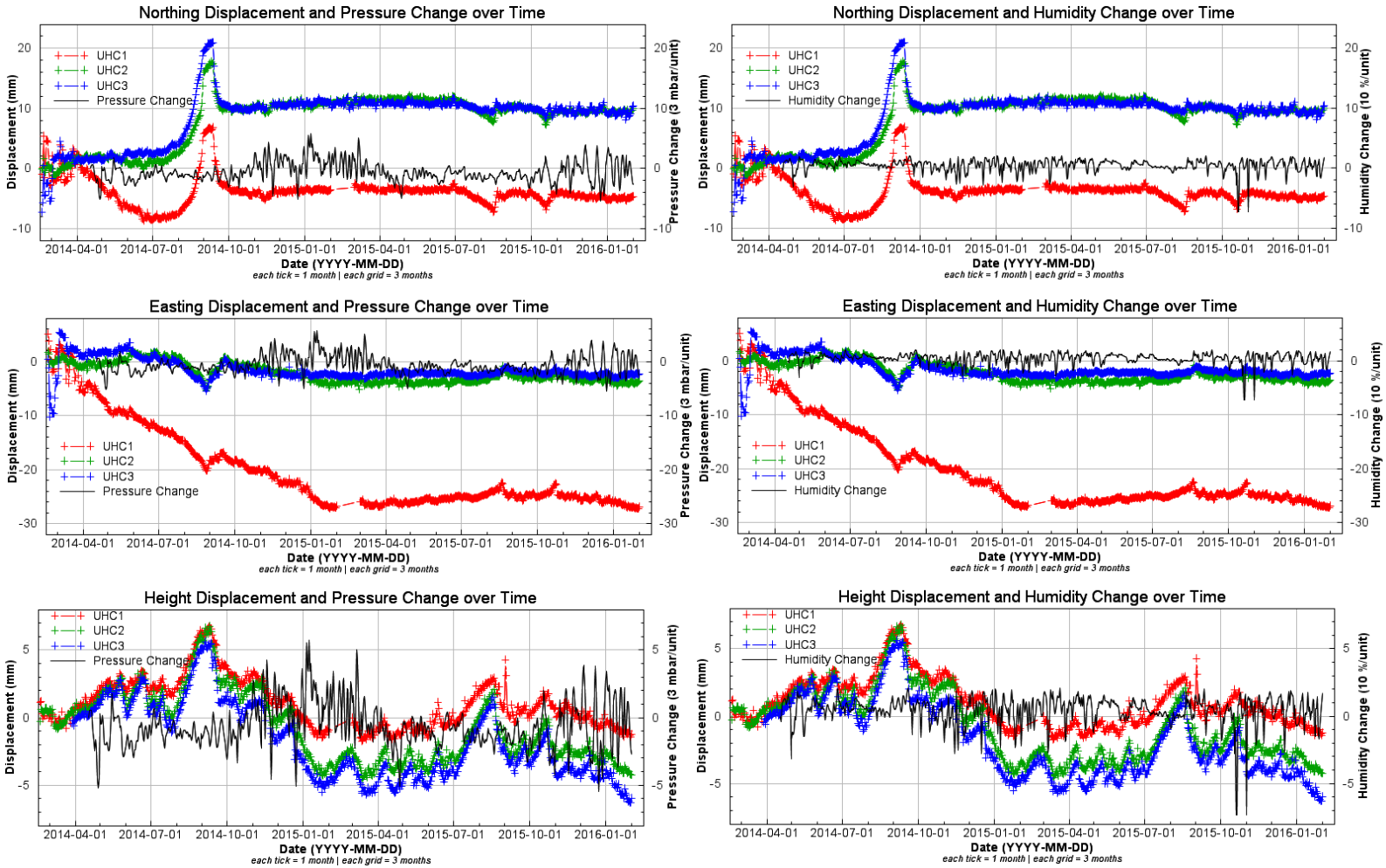

Figure 4.3.1: (left) Pressure and (right) humidity change and NEH spatial displacement vs time. Note the unit measurement of displacement for all three UHC stations is in millimeters, whereas every Y-axis unit equates to 3 millibars of pressure and 10% of humidity in the air.

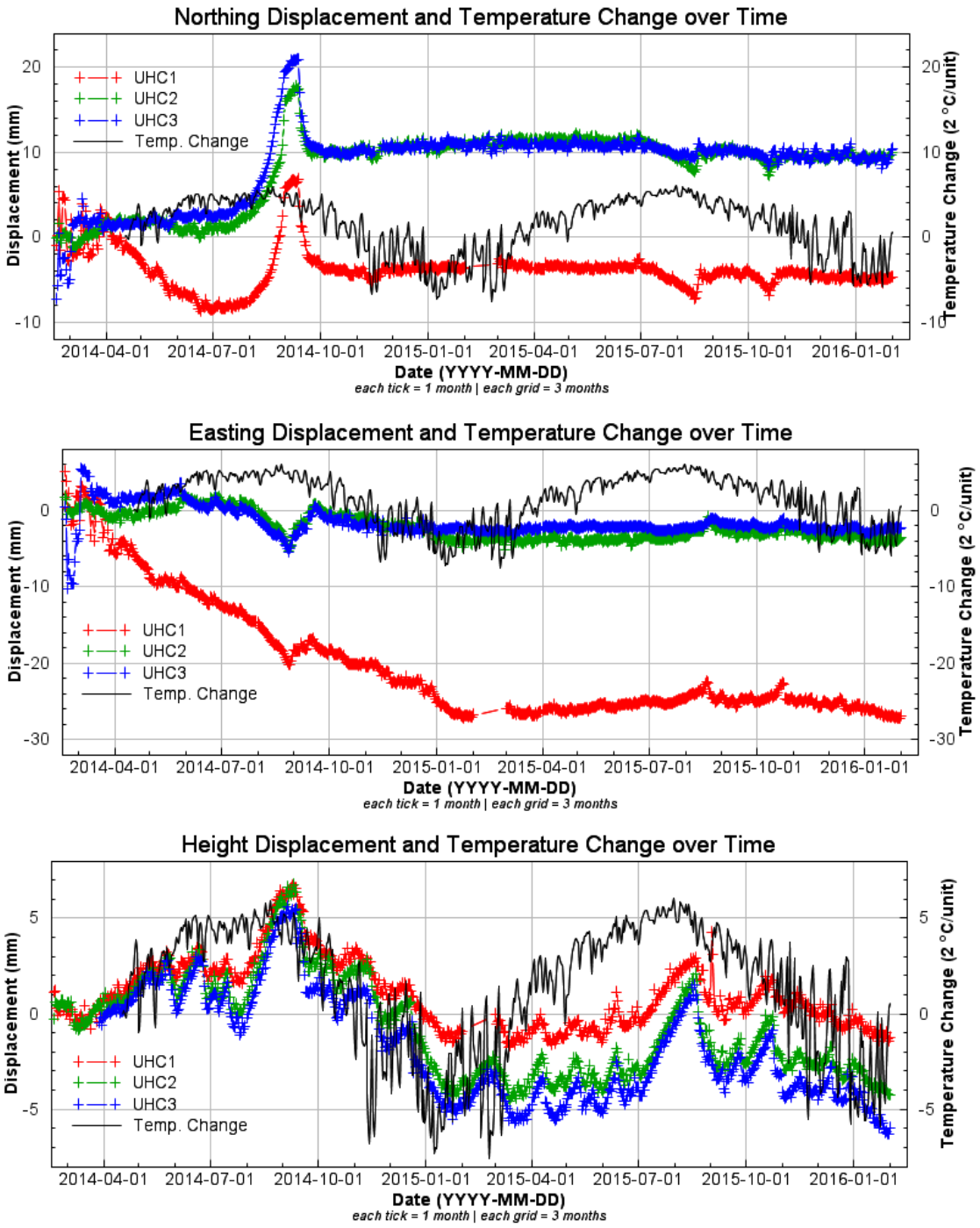

Figure 4.3.2: Temperature change and NEH spatial displacement vs time. Note the unit measurement of displacement for all three UHC stations is in millimeters, but every Y-axis unit equates to 2 degrees Celsius.

5 Groundwater Wells

5.1 Introduction

As mentioned in Section 2.3, three wells at the UHCC were used to measure groundwater levels: the “Gray well” located at UHC3 (Figure 2.3.1, left), and the “Red well” and “Blue well” set about 100 m away to the east on a separate but adjacent aquifer (Figure 2.3.1, middle and right, respectively).

Table 5.1.1 gives the absolute coordinates of the three wells, processed with OPUS. Small but conspicuous height differences between the three wells’ absolute coordinate lip heights were calculated by adding onsite lip height above ground and adding to NAD_83 orthogonal height measurements. Table 5.1.2 catalogues the original measurements (in decimal feet) of water levels at the three wells. These measurements were taken on a near-monthly basis by numerous people, but lack consistent readings from February to August of 2015. In the table, one should note the maximal respective depths of 11.41, 79.96, and 78.62 ft of the Gray, Red, and Blue wells; thus the Gray well is anticipated to resemble UHC1’s 10-foot-deep layer in vertical movement. The deeper-groundwater head of nearly 80 ft at Red and Blue are due to their being on the separate, but adjacent Chicot aquifer.

Table 5.1.1: UHCC well coordinates: OPUS.

Well Lip	UTM_Northing (m)	UTM_Easting (m)	NAVD88_ORTHO_HGT (m)
Gray Lip	3252973	301656.72	5.7355234
Red Lip	3253057	301791.02	5.528
Blue Lip	3253056	301809.9	5.179

Table 5.1.2: UHCC groundwater measurements from 2014 to 2016.

Date	Gray (ft)	Or.Hgt (m)
3/27/2014	8.310	*3.203*
5/6/2014	10.500	*2.535*
5/20/2014	10.840	*2.431*
6/5/2014	7.980	*3.303*
6/19/2014	10.130	*2.648*
7/10/2014	8.010	*3.294*
8/5/2014	8.830	*3.044*
9/5/2014	11.410	*2.258*
9/16/2014	10.500	*2.535*
10/3/2014	7.450	*3.465*
10/25/2014	8.110	*3.264*
11/21/2014	7.900	*3.328*
12/12/2014	7.780	*3.364*
1/9/2015	6.260	*3.827*
5/2/2015	6.060	*3.888*
9/7/2015	6.000	*3.907*
11/20/2015	6.800	*3.663*
1/23/2016	6.180	*3.852*
2/20/2016	7.520	*3.443*
Average	8.241	*3.224*

Date	Red (ft)	Or.Hgt (m)	Blue (ft)	Or.Hgt (m)
5/20/2014	78.870	*-18.512*	77.690	*-18.501*
6/19/2014	78.930	*-18.530*	77.630	*-18.483*
8/5/2014	78.885	*-18.516*	77.550	*-18.458*
9/16/2014	79.960	*-18.844*	78.620	*-18.784*
10/3/2014	77.120	*-17.978*	77.080	*-18.315*
10/25/2014	78.990	*-18.548*	77.670	*-18.495*
12/12/2014	78.580	*-18.423*	78.210	*-18.659*
1/9/2015	77.270	*-18.024*	76.900	*-18.260*
5/2/2015	77.140	*-17.984*	75.850	*-17.940*
9/7/2015	79.100	*-18.582*	76.800	*-18.230*
10/17/2015	78.475	*-18.391*	77.190	*-18.349*
11/20/2015	79.400	*-18.673*	78.500	*-18.748*
1/23/2016	77.060	*-17.960*	75.740	*-17.907*
2/20/2016	76.910	*-17.914*	75.640	*-17.876*
Average	78.335	*-18.349*	77.219	*-18.357*

Graphing the absolute orthometric well-water heights (positive being “up,” negative being “down” into the Earth) for all three wells of Table 5.1.2, it is notable that only Gray’s water table sits above NAD_83 defined sea level (Figure 5.1.1, top). The Chicot-aquifer-situated Red and Blue wells have water tables well below it (Figure 5.1.1, bottom). This study asserts that the UHC antennae and Gray well are situated on a different top aquifer separate from the Chicot aquifer, where the Red and Blue wells reside. Also, despite the Red well situated 10 meters closer to the top aquifer of the antenna array than the Blue well, neither water level was consistently above the other (Fig 5.1.1, bottom).

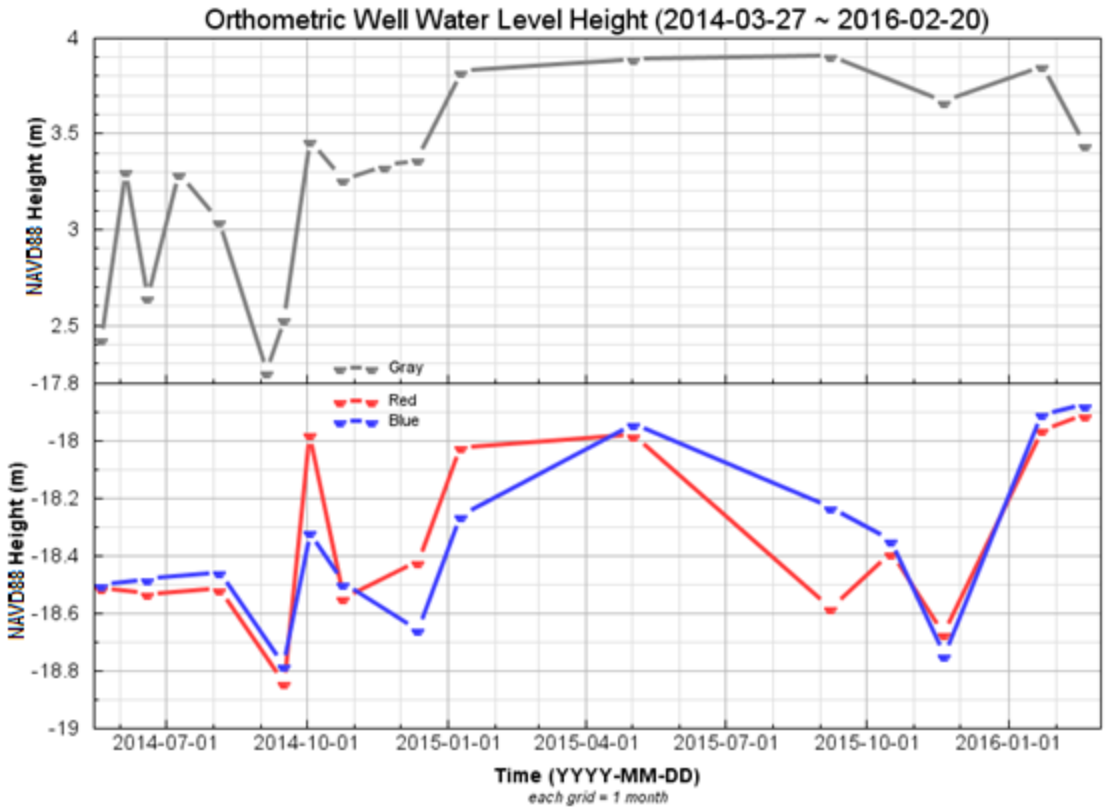

Figure 5.1.1: UHCC absolute groundwater orthometric height according to the NAVD88 for the Gray well (top) and Red and Blue wells. Positive values are pointing up and away from the center of the Earth.

These absolute water-level heights are within the correct order of magnitude with nearby well-water level time series in the region (Figure 5.1.2) such as KH-65-48-502 and KH-65-48-204 (Figure 5.1.3, top and bottom, respectively); UHCC is shown in between the two for comparison (Fig 5.1.3, middle).

With the context of absolute well water levels in the general area in mind, the displacement of UHCC's well-water levels is discussed in the next subsection, and compared with Section 3's GPS displacements.

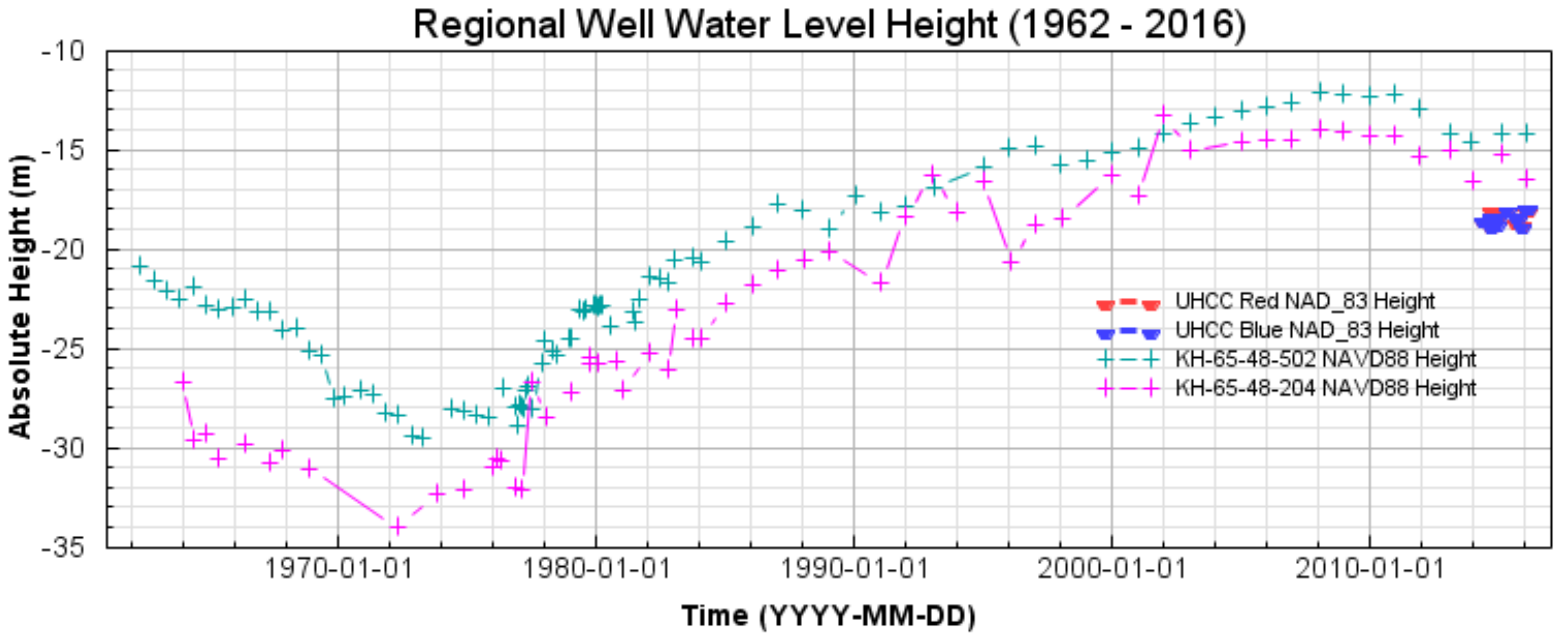

Figure 5.1.2: Graph of absolute height coordinates of groundwater level of the region around UHCC over time from 1962 to 2016. Note the short two-year data of UHCC's Red and Blue well measurements.

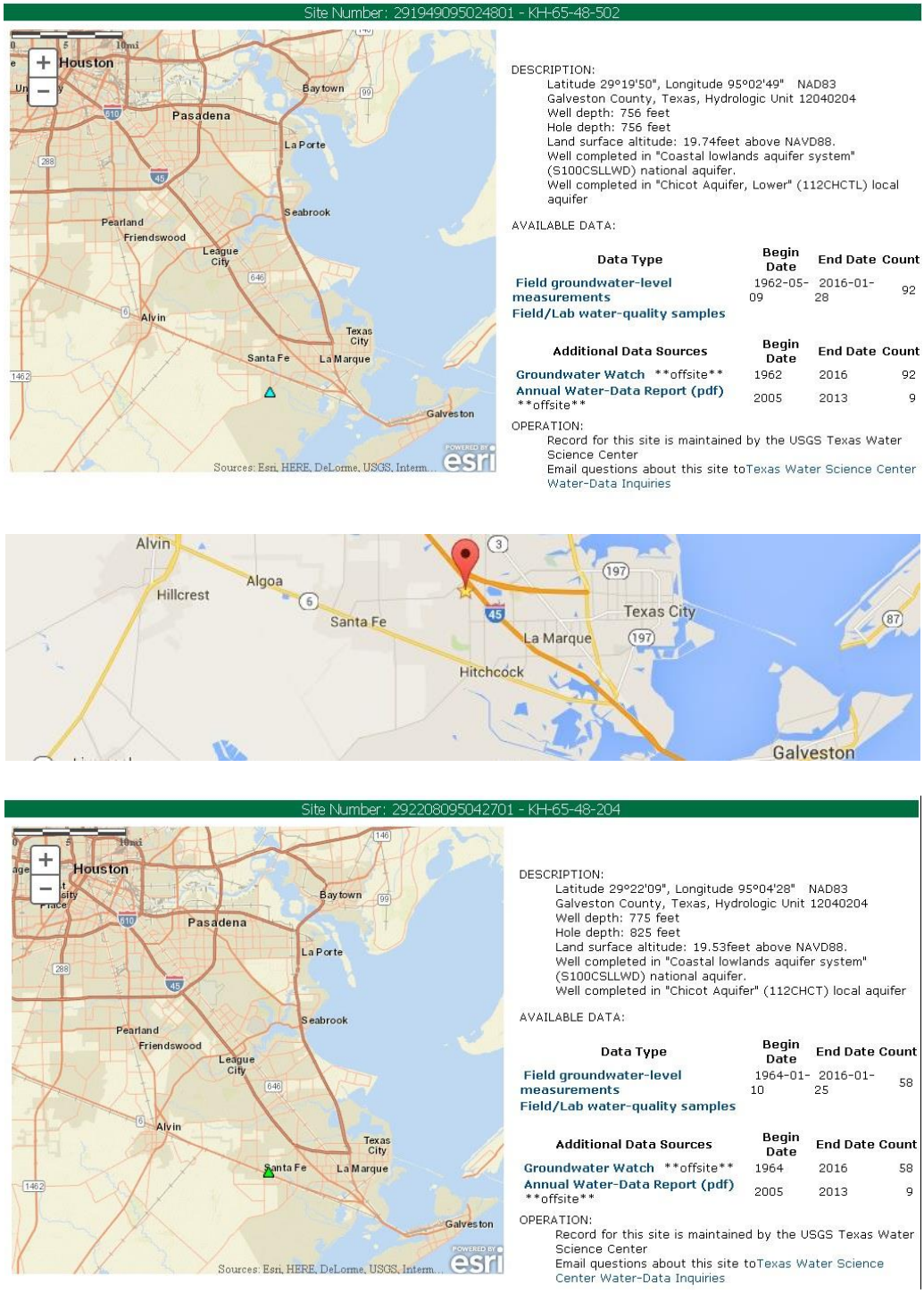

Figure 5.1.3: KH-65-48-502 (top) and KH-65-48-204 (bottom) via USGS Groundwater Watch, with UHCC (middle) via Google Maps.

5.2 Groundwater Well Depth Levels

Figures 5.2.1, 5.2.2, and 5.2.3, respectively show the Gray, Red, and Blue wells' water-level displacements (after scaling) matched to the GPS-height displacement. The well-water depths are zeroed by each respective value on May 20th, 2014, the first common date when all three wells were measured. The numerical correlation exhibited shows that for every two decimeters (0.2 m) of Gray well water level drop (Fig 5.2.1) and a possible decimeter of Red and Blue well-water level drop (Fig 5.2.2 and 3), there is one millimeter of underground compaction.

Only around three of the eighteen well-depth displacements shown scaled for each well are not within the range of antenna-base displacements from UHC1 to UHC3. All three well-water level points are plotted one-to-one with the three subsurface stations (Fig 5.2.4). Table 5.2.1 shows the correlation coefficients for each station to each well, and on average shows 0.88 for the Gray well, 0.54 for the Red well, and 0.70 for the blue well. This is promising, especially for the co-located Gray well, for what automated-groundwater measurements could show with their higher consistency, accuracy, and quantity.

Lastly, the water-level displacement (10/17/2015 - 2/1/2016) is juxtaposed to UHC displacement data (Figure 5.2.5). Scaling 1:200, ground-layer displacement fits to onsite groundwater-level displacement with a correlative coefficient average of 0.61. Much like with horizontal-GPS data, it is hoped that hereafter the automated data will be more consistent.

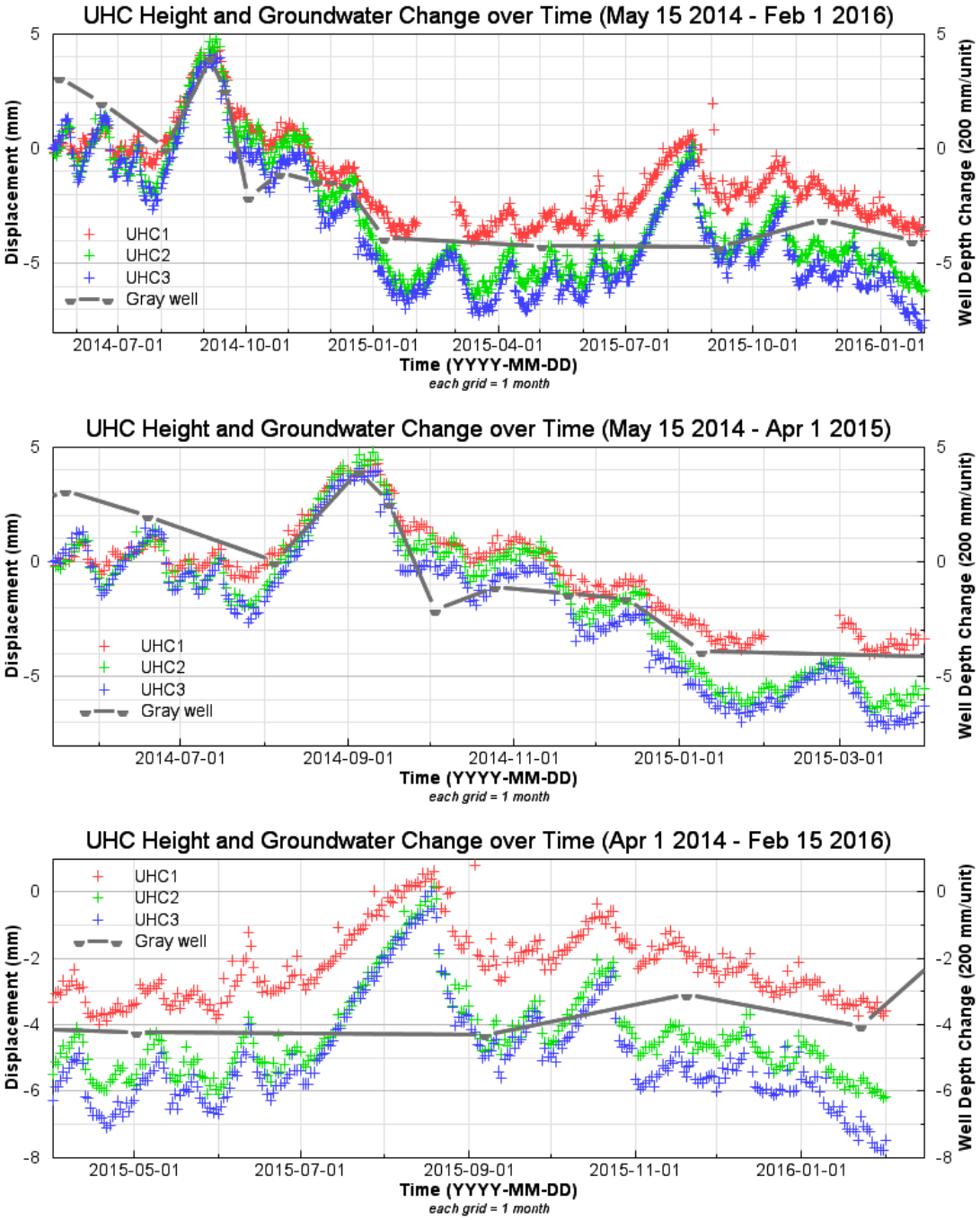

Figure 5.2.1: (top) Gray well water level displacement and UHCC height displacements over two years. Note well-level change is per 2 decimeters. (middle) Groundwater- and ground-layer displacements from May 15th, 2014, to Apr 1st, 2015, and (bottom) from Apr 1st, 2015, to Feb 15th, 2016; each half is 10.5 months long.

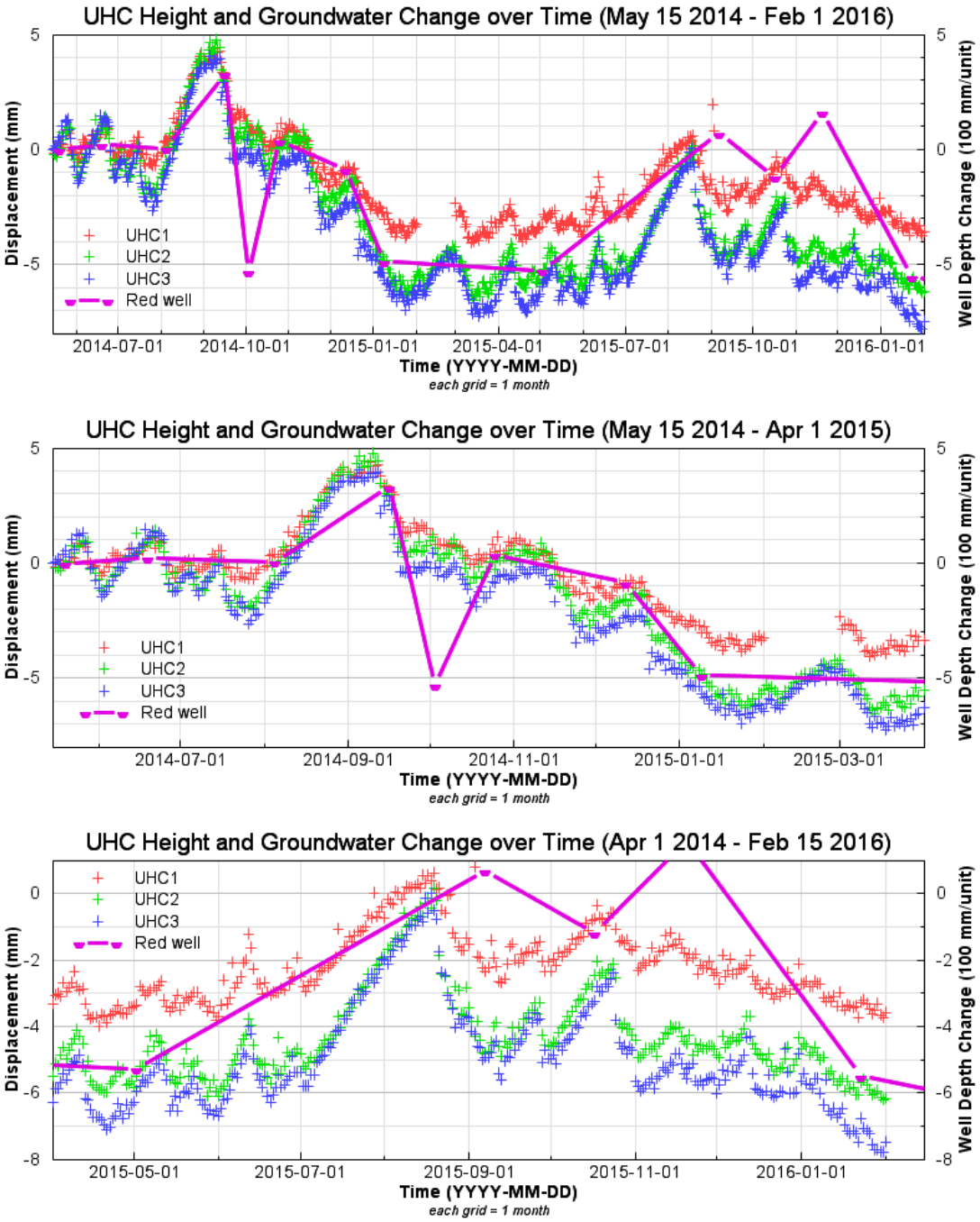

Figure 5.2.2: (top) Red well water level displacement and UHCC height displacements over two years. Note well-level change is per decimeter. (middle) Groundwater- and ground-layer displacements from May 15th, 2014, to Apr 1st, 2015, and (bottom) from Apr 1st, 2015, to Feb 15th, 2016; each half is 10.5 months long.

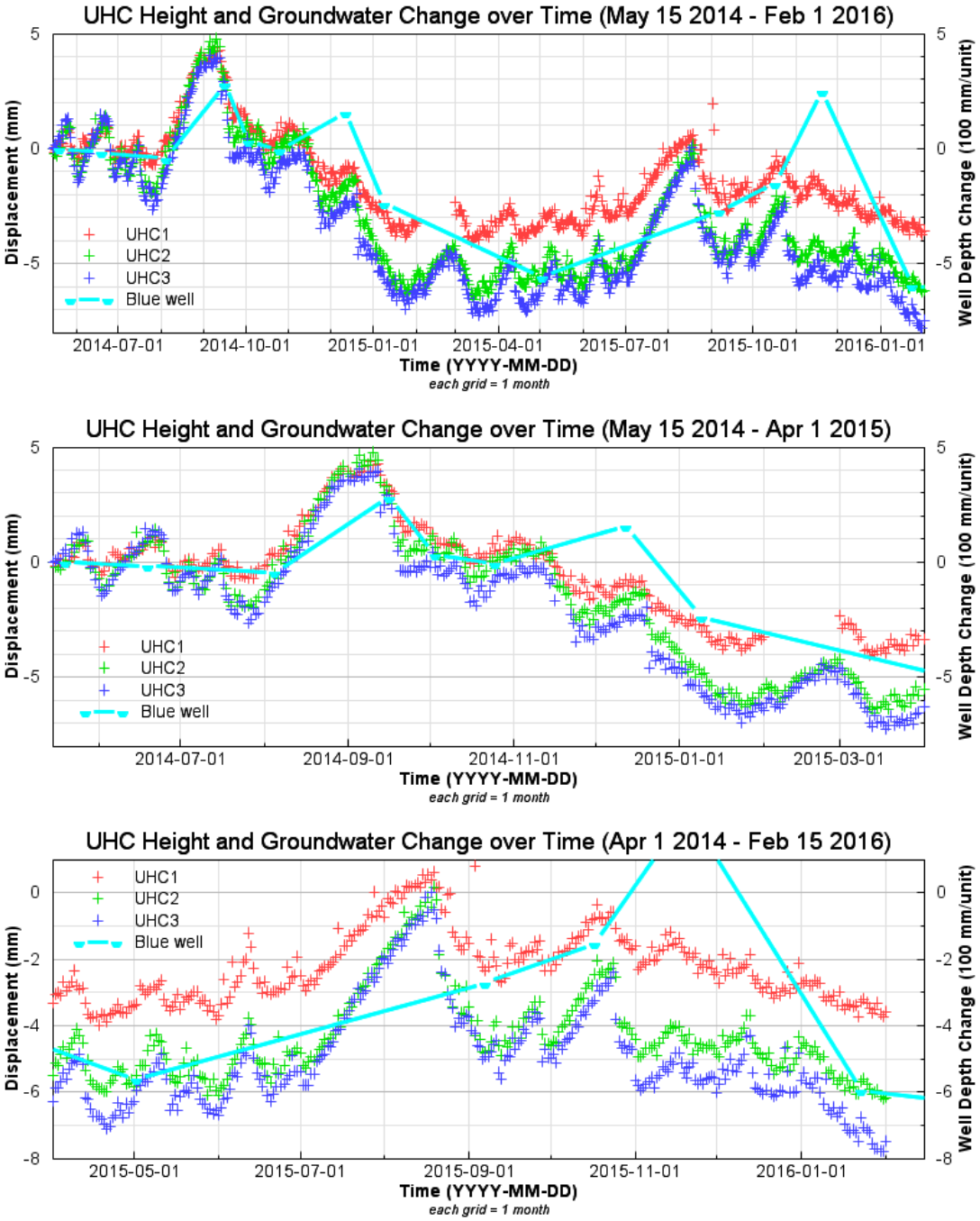

Figure 5.2.3: (top) Blue well water-level displacement and UHCC height displacements over two years. Note well level change is per decimeter. (middle) Groundwater- and ground-layer displacements from May 15th, 2014, to Apr 1st, 2015, and (bottom) from Apr 1st, 2015, to Feb 15th, 2016; each half is 10.5 months long.

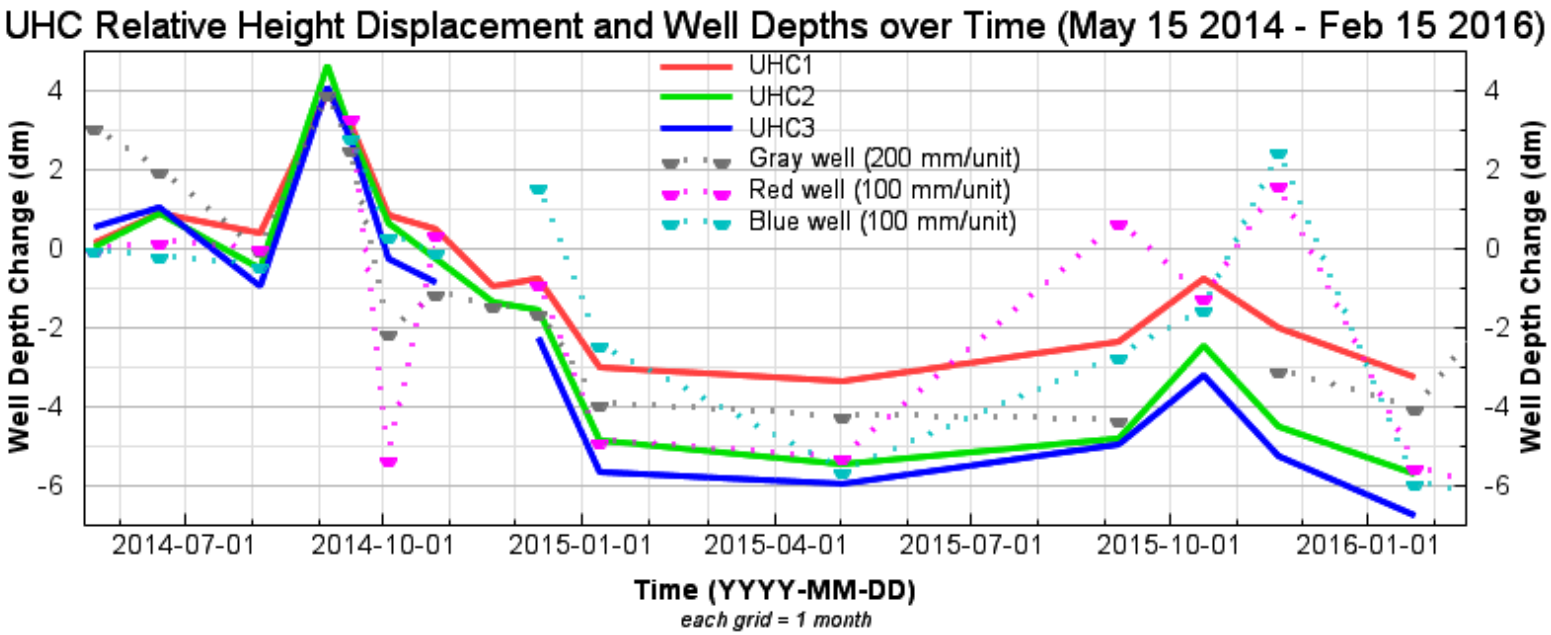

Figure 5.2.4: A combination of Figures 5.2.1, 5.2.2, and 5.2.3. All three well level displacements are overlaid on the vertical subsurface ground-layer displacement.

Table 5.2.1: Correlation coefficients for each well to each station.

	dh1 (mm)	dh2 (mm)	dh3 (mm)
dGray (2dm)	0.85	0.88	0.91
dRed (dm)	0.59	0.50	0.54
dBlue (dm)	0.73	0.70	0.68
dAuto (2dm)	0.44	0.69	0.71

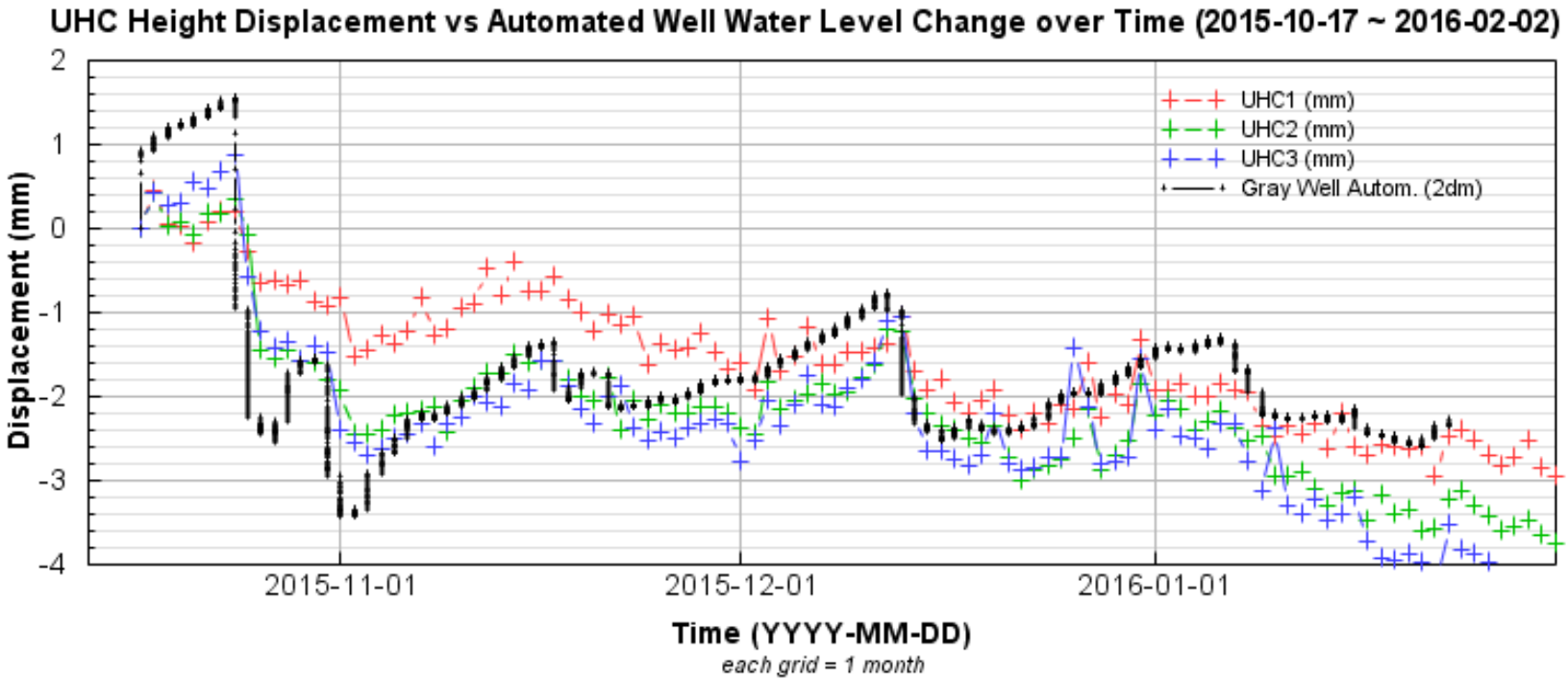

Figure 5.2.5: Graph of UHCC height displacement vs automated well water-level displacement over time period from October 17th, 2015, to February 2nd, 2016. The points follow the earlier hypothesized correlation of 1 mm ground layer displacement to 2 dm of well water level displacement.

6 Conclusions and Discussions for Further Study

In this study, GPS data, weather data, and well data have been compared to find correlations between the three datasets at UHCC, and to answer the question of how the shallow (<10 m) subsurface, at least for UHCC, impact overall subsidence of the surrounding area. What is seen is that the upper layer of about 3 meters is generally inflating as the lower layers continue to subside. The inflation of the surface—decreasing in height by 1 to 2 mm/yr—mitigates the lowest level's decline of 3 to 4 mm/yr. At an almost linear 1:200 correlation at the UHCC top aquifer, applications of this factor are limited to translating vertical ground deformation to groundwater displacement and vice versa.

For these conclusions, horizontal- and vertical-positional displacement data at 10, 20, and 30 feet below the surface with respect to 0 feet, rain accumulation, and weather change data, and well-water depth data at aquifers both co-located and adjacent to the GPS antenna array have been processed and presented. All three sets of data were compared to find qualitative and quantitative correlations.

Section 1 introduced the issue of ground movement in the Harris-Galveston Subsidence District, the context of the local geologic history, the theory behind the Global Positioning System, and the convention of terms used throughout this document. Section 2 discussed the GPS antenna array design, installation, and implementation, GPS data processing, weather sensor data collection, and groundwater well setup.

Section 3 laid the foundation of the February 2014—February 2016 observational period by presenting absolute horizontal and vertical coordinates and their displacement measurements of the subsurface layers at UHCC's antenna array.

Section 4 discussed how accumulated rain measurements were compiled and juxtaposed to Section 3's positional displacement figures. A general relation was found that substantial rainfall of over two centimeters per day caused abrupt changes in ground-layer height, and that sustained precipitation effected noticeable overall subterranean-level change relative to the surface. Although pressure, humidity, and temperature do not have a direct correlation with ground movement, they are still factors to consider when understanding the precipitation time series.

Lastly, Section 5 showed 1 mm of UHC array vertical movement of the subsurface approximately correlates to 200 mm water-level displacement for the co-located Gray well, and less so to 100 mm of groundwater-head displacement for the Red and Blue wells in the adjacent Chicot aquifer. This was with a correlative coefficient confidence on average of about 0.71. We also tried matching the relatively short automated well-level dataset with ground-layer displacements, but will have to wait for further measurements for a more confident confirmation or denial of the approximate 1:200 ratio.

Future work to be conducted for studies of this kind would be to continue measuring ground deformation with the antenna array, precipitation with the weather sensor, and groundwater with the automated well troll. With more data

added to what is presented here, more definitive implications of the nature of subsidence occurring in the La Marque area can be inferred by future scholars.

References

AAPG (American Association of Petroleum Geologists). (2011). “Salt tectonism of the U.S. Gulf Coast Basin.” (CD-ROM), *GIS-UDRIL* (*Geographic Information System-Upstream Digital Reference Information Library*).

Ashworth JB and Hopkins J. (1995). “Aquifers of Texas.” *Rep. No. 345, Texas Water Dev Board, Austin, TX.* https://www.twdb.state.tx.us/publications/reports/numbered_reports/doc/R345/R345Complete.pdf (Dec. 1, 2014).

Baker E. (1979). “Stratigraphic and Hydrogeologic Framework of Part of the Coastal Plain of Texas.” *USGS Open-File Rep 77-712*. *Rep No. 236, Texas Dept of Water Resources,* Austin, TX. https://www.twdb.state.tx.us/publications/reports/numbered_reports/doc/R236/R236.pdf Accessed Dec 1, 2014.

Bawden GW, Johnson MR, Kasmarek MC, Brandt J, Middleton CS. (2012). “Investigation of Land Subsidence in the Houston-Galveston Region of Texas by Using the Global Positioning System and Interferometric Synthetic Aperture Radar, 1993–2000.” *U.S. Dept of the Int U.S. Geol Surv Sci Inv Rep 2012–5211*.

BCGCD (Brazoria County Groundwater Conservation District). (2012). “Groundwater management plan, December 13, 2012.” http://www.bcgroundwater.org/images/bcg/documents/BCGCD_Groundwater_Management_Plan_2012 1213.pdf Accessed Dec 1, 2014.

Bird DE, Burke K, Hall SA, Casey JF. (2005). “Gulf of Mexico Tectonic History: Hotspot Tracks, Crustal Boundaries, and Early Salt Distribution.” *AAPG Bulletin 89(3):* 311–328.

Blewitt G. (1989). “Carrier phase ambiguity resolution for the Global Positioning System applied to geodetic baselines up to 2,000km.” *J Geophys Res 94(B8):* 10,187–10,203.

Bruckl E, Brunner FK, Kraus K. (2006). “Kinematics of a deep-seated landslide derived from photogrammetric, GPS and geophysical data.” *Eng 88:* 149–159.

Buckley SM, Rosen P, Hensley S, Taplay BD. (2003). "Land subsidence in Houston, Texas, measured by radar interferometry and constrained by extensometers." *Geophys Res, 108(B11).*

Capuano RM and Lindsay SV. (2012). "Chicot/Evangeline Aquifer of the Texas Gulf Coast, Groundwater Age and Pathways for Saltwater Contamination." *Environmental Institute of Houston, 2004 Annual Report*.

http://prtl.uhcl.edu/portal/page/portal/EIH/publications/annual_reports/ar_2004/04capuano/04capuano.pdf Accessed Feb 13, 2012.

Chowdhury AH and Turco MJ. (2006). “Geology of the Gulf Coast aquifer, Texas. Texas Water Development Board Report 365.” http://www.twdb.state.tx.us/publications/reports/numbered_reports/doc/R365/ch02-Geology.pdf Accessed Feb 13, 2012.

Coleman JM, Roberts HH, and Bryant WR. (1991). “Origin and Development of the Gulf of Mexico Basin.” *The Geol of N Am, Vol J: Geol Soc of Am,* Boulder, Colorado: 325–352.

Coplin LS and Galloway D. (1999). “Houston-Galveston, Texas: Managing Coastal Subsidence.” s.l.: *USGS*. http://pubs.usgs.gov/circ/circ1182/pdf/07Houston.pdf Accessed Mar 25, 2015.

Dong D, Bock Y. (1989). “GPS network analysis with phase ambiguity resolution applied to crustal deformation studies in California.” *J Geophys Res 94(B4):* 3949–3966.

Eckl MC, Snay RA, Soler T, Cline MW, Mader GL. (2001). “Accuracy of GPS-derived relative positions as a function of interstation distance and observing-session duration.” *J Geophys Res 75(12)*: 633–640.

El-Rabbany A. (2006). “Introduction to GPS - The Global Positioning System 2nd Edition.” *Norwood: Artech House*.

Engelkemeir R, Khan SD, Burke K. (2010). “Surface Deformation in Houston, Texas Using GPS.” *Tectonophysics, 490(1-2)*: 47-54.

ESRI (Environmental Systems Research Institute). (2012). “ArcGIS online world topographic map final updates for 2012.” http://blogs.esri.com/esri/arcgis/2012/12/28/arcgis-online-world-topographic-map-final-2012-updates Accessed Mar 25, 2015.

Ewing TE. (1983). "Growth Faults and Salt Tectonics in the Houston Diapir Province—Relation, Timing and Exploration Significance." *Gulf Coast Assoc of Geol Soc Transactions, 33:* 83-90.

Ewing TE. (1991). "Structural framework: The Gulf of Mexico Basin." *Geol Soc of Am, The Geol of N Am, Vol J:* 31-52.

FBSD (2013). “Fort Bend Subsidence District Regulatory Plan.” http://www.fbsubsidence.org/docs_reports/2014/20130828%20FBSD%20Regulatory%20Plan%20ADOPTED%20-%20(FINAL).pdf Accessed Apr 1, 2014

Gabrysch R. (1984a). “Ground-water Withdrawals and Land-Surface Subsidence in the Houston-Galveston Region.” *Rep. No. 287, Texas Dept of Water Resources,* Austin, TX.

Gabrysch R. (1984b). “Subsidence in the Houston-Galveston region, Texas, U.S.A.” *Guidebook to Studies of Land Subsidence due to Ground-water Withdrawal, J. F. Poland, ed., UNESCO*, Paris: 253–262.

Gabrysch RK and Bonnet CW. (1975). “Land-Surface Subsidence in the Houston-Galveston Region, Texas.” *Texas Water Dev Board*, Austin, Tex, USA.

Galloway D, Copland LS. (1999). “Houston-Galveston Texas: Managing Coastal Subsidence.” *USGS:* 36-49.

Galloway D, Jones D, Ingebritsen S. (1999). “Land subsidence in the United States,” *U.S. Geol Surv, U.S. Dept of the Int,* Reston, VA, USA.

Galloway DL, Burbey TJ. (2011). “Review: Regional land subsidence accompanying groundwater extraction.” *Hydrogeol J, 19*: 1459–1486.

Gili JA, Corominas J, Rius J. (2000). “Using Global Positioning System techniques in landslide monitoring.” *Eng Geol, 55(3)*: 167–192.

Goad C. (1985). “Precise relative positioning determination using global positioning system carrier phase measurements in a nondifferenced mode.” *Proc, 1st Int Symp on Precise Positioning Sys with the Glob Positioning Sys, U.S. Dept of Commerce, Nat Oceanic and Atmos Admin*, Silver Spring, MD: 347–356.

Grinter T, Roberts C. (2011). “Precise point positioning: where are we now?” *Int Glob Nav Satellite Sys Soc IGNSS Symp 2011*, Sydney, Australia: 15–17.

Gurtner W. (2009). “RINEX - The Receiver Independent Exchange Format Version 3.01.” *Astro Instit, Univ of Bern.* https://igscb.jpl.nasa.gov/igscb/data/format/rinex301.pdf Last modified June 22, 2009. Accessed Sep 2013.

Hastaoglu KO, Sanli DU. (2011). “Monitoring Koyulhisar landslide using rapid static GPS: a strategy to remove biases from vertical velocities.” *Nature Hazards 58(3):* 1275–1294.

Herring T, King RW, McCluskey SM. (2009). “Introduction to GAMIT/GLOBK.” Release 10.35. *Mass Instit of Tech, Cambridge*.

HGCSD. (1999). “HGCSD Regulatory Plan.” http://www.hgsubsidence.org/assets/pdfdocuments/HGRegPlan.pdf Accessed Dec 1, 2014.

HGSD (Harris-Galveston Subsidence District). (1999). “Harris-Galveston Subsidence District Regulatory Plan.” Adopted April 14, 1999, amended September 12, 2001, and June 9, 2010. http://www.hgsubsidence.org/assets/pdfdocuments/HGRegPlan.pdf Accessed Dec 1, 2014.

HGSD (Harris-Galveston Subsidence District). (2013). “Harris-Galveston Subsidence District Regulatory Plan.” Adopted January 9, 2013; amended May 8, 2013. http://hgsubsidence.org/wpcontent/uploads/2013/07/HGSD-2013-Regulatory-Plan-with-Amendment.pdf Accessed Dec 1, 2014.

Holzer TL and Bluntzer RL. (1984). “Land subsidence near oil and gas fields, Houston, Texas.” *Groundwater, 22(4):* 450–459.

Holzer TL and Gabrysch RK. (1987). "Effect of Water-Level Recoveries on Fault Creep, Houston, Texas." *Groundwater, 25(4):* 392-397.

Huffman AC, Kinney SA, Biewich LR, Mitchell HR, Gunther GL. (2004). "Salt Diapirs in the Gulf Coast." *U.S. Geol Surv, DS 90-A, version 1.0- Miocene of S Louisiana*. http://pubs.usgs.gov/ds/2004/90/A/about.htm Accessed Apr 3, 2013.

In-Situ Inc. (2013). “Operator’s Manual: Level TROLL® 400, 500, 700, 700H Instruments.” https://in-situ.com/wp-content/uploads/2014/11/Level-TROLL-400-500-700-700h_Manual.pdf 0052210 | Rev. 009 | Accessed Sep 2013.

International GNSS Service (IGS). (2013) “RINEX: The Receiver Independent Exchange Format.” *RINEX Working Group and Radio Tech Commission for Maritime Serv Spec Committee 104 (RTCM-SC104).* ftp://igs.org/pub/data/format/rinex302.pdf Accessed Apr 3, 2013.

Jia X. (2015). “Current ground deformation along the east coastal region of China derived from GPS observations (2010-2014).” *Dept of Earth and Atmos Sci, Univ of Houston.*

Jorgensen DG. (1975). “Analog-model studies of ground-water hydrology in the Houston District, Texas.” *Texas Water Dev Board Rep 190*: 84.

Kasmarek MC and Strom EW. (2002). “Hydrogeology and Simulation of Ground-Water Flow and Land-Surface Subsidence in the Chicot and Evangeline

Aquifers, Houston Area, Texas." *U.S. Geol Surv Water-Resources Inv Rep 02–4022*. Austin, TX.

Kasmarek MC, Gabrysch RK, Johnson MR. (2009a). "Estimated land-surface subsidence in Harris County, Texas, 1915–17 to 2001." *USGS Sci Inv Map 3097*, USGS, Reston, VA.

Kasmarek M, Houston N, Ramage J. (2009b). "Water-level altitudes 2009 and water-level changes in the Chicot, Evangeline, and Jasper aquifers and compaction 1973–2008 in the Chicot and Evangeline aquifers, Houston-Galveston region, Texas: U.S." *U.S. Geol Surv Sci Inv.*

Kasmarek M, Johnson M, Ramage J. (2010). "Water-level altitudes 2010 and water-level changes in the Chicot, Evangeline, and Jasper aquifers and compaction 1973–2009 in the Chicot and Evangeline aquifers, Houston-Galveston region, Texas." *U.S. Geol Surv Sci Inv.*

Kearns TJ, Wang G, Bao Y, Jiang J, Lee D, (2015). "Current Land Subsidence and Groundwater Level Changes in the Houston Metropolitan Area, Texas (2005–2012)." *Am Soc of Civ Eng*.

Kenny J et al. (2009). "Estimated use of water in the United States in 2005." s.l.: *USGS*.

Kouba J. (2005). "A possible detection of the 26 December 2004 great Sumatra-Andaman Islands earthquake with solution products of the int. GNSS service." *Stud Geophys Geod 49(4):* 463–483.

Kouba J, Springer T. (2001). "New IGS station and satellite clock combination." *GPS Soln 4(4):* 31–36.

Kummu M, de Moel H, Ward PJ, Varis O, Perc M. (2011). "How Close Do We Live to Water? A Global Analysis of Population Distance to Freshwater Bodies." *PLoS One*. 6(6): e20578. http://www.ncbi.nlm.nih.gov/pmc/articles/PMC3110782/ Accessed Dec 1, 2014.

Lohse EA. (1955). "Dynamic geology of the modern coastal region, northwest Gulf of Mexico, in finding ancient shorelines." *Soc Econ Paleontologists and Mineralogists Spec Pub No. 3*: 99–105.

LSGCD (Lone Star Groundwater Conservation District). (2003). "Groundwater management plan." http://lonestargcd.org/wp-content/uploads/2014/09/031014-Final-Adopted-Management-Plan-BS.pdf Accessed Dec 1, 2014.

McFarlan E and Menes LS. (1991). “Origin and Development of the Gulf of Mexico Basin.” *The Geol of N Am, Volume J: Geol Soc of Am*, Boulder, Colorado: 181–204.

Meyer WG. (1939). "Stratigraphy and Historical Geology of Gulf Coastal Plain in Vicinity of Harris County, Texas." *AAPG Bulletin, 23:* 145–211.

National Geodetic Survey. (2016). “OPUS: Online Positioning User Service.” http://www.ngs.noaa.gov/OPUS/ Last modified by *NGS OPUS V 2.3*, Accessed Feb 11, 2016.

Neighbors RJ, Mitchell GJ. (2010). “A Plan to Use Continuously Operating GPS Stations to Monitor Subsidence in The Harris-Galveston Coastal Subsidence District.”

Neill R. (2015). “Spatial and Temporal Variability of Subsidence: Fort Bend County, Texas.” *Univ of Houston.*

Nelson TH. (1991). “Origin and Development of the Gulf of Mexico Basin.” *The Geol of N Am, Volume J: Geol Soc of Am,* Boulder, Colorado: 73–90.

Ortega J. (2013). “Land Surface Subsidence and Aquifer Compaction: A Comparison of Surficial and Deep-Monument GPS Data, Northwest Harris County, Texas.” *Univ of Houston, Earth and Atmos Sci.*

Peyret M, Djamour Y, Rizza M, Ritz JF, Hutrez JE, Goudarzi MA, Nankali H, Chery J, Le Dortz K, Uri F. (2008). “Monitoring of the large slow Kahrod landslide in Alboz mountain range (Iran) by GPS and SAR interferometry.” *Eng Geol 100(3–4):* 131–141.

Poland JF, Yamamoto S, and Working Group. (1984). “Field measurement of deformation.” *Guidebook to Studies of Land Subsidence due to Ground-water Withdrawal*, *J. F. Poland, ed., UNESCO*, Paris: 17–35.

Potter S. (2014). “Seismic Sensing, Subsidence and Groundwater.” *Univ of Houston.*

Pratt W and Johnson D. (1926). “Local subsidence of the Goose Creek Oil Field.” *The J of Geol*, 34(7): 577–590.

Ray J, Dong D, Altamimi Z. (2004). “IGS reference frames: status and future improvements.” *GPS Soln 8(4):* 251–266.

Reid WM. (1973). "Active Faults in Houston, Texas." *Univ of Texas at Austin*: 1–143.

Rizos C, Janssen V, Roberts C, Grinter T. (2012). “Precise Point Positioning: Is the Era of differential GNSS positioning drawing to an end?” *TS09B, FIG Working Week 2012*, Rome, Italy: 6–10.

Rocken C, Meertens C, Stephens B, Braun J, VanHove T, Perry S, Ruud O, McCallum M, Richardson J. (1995). “UNAVCO academic research infrastructure (ARI) receiver and antenna test report.” http://www.unavco.org/projects/project-support/development-testing/publications/ari_test.pdf Accessed Jul 27, 2015.

Salvador A. (1991). “Origin and Development of the Gulf of Mexico Basin.” *The Geol of N Am, Volume J: Geol Soc of Am,* Boulder, Colorado: 131–180, 389–444.

Schomaker M, Berry R. (1981). “Geodetic leveling. NOAA Manual NOS NGS 3.” *Rockville: U.S. Dept of Commerce*.

Serna J. (2015). “Current Ground Motions Along the Long-Point Fault Derived from Continuous GPS Observations (2012–2014).” *Univ of Houston.*

Shah SD and Lanning-Rush J. (2005). “Principal Faults in the Houston, Texas, Metropolitan Area.” *U.S. Geol Surv Sci Invs Map* 2874. Reston, VA. http://pubs.usgs.gov/sim/2005/2874/ Accessed Mar 30, 2016.

Solinst. (2016). “Water Level Indicator Model 102 Laser Marked Water Level Indicators.” http://www.solinst.com/products/level-measurement-devices/102-water-level-indicator/datasheet/ Accessed Mar 30, 2016.

SOPAC. (2015). “Hatanaka file compression; Hatanaka Conversion Program.” http://sopac.ucsd.edu/hatanaka.shtml Accessed Mar 30, 2016.

Tagliavini F, Mantovani M, Marcato G, Pasuto A, Silvano S. (2007). “Validation of landslide hazard assessment by means of GPS monitoring technique—a case study in the Dolomites (Eastern Alps, Italy).” *Nat Hazards Earth Syst Sci 7(1):* 185–193.

TSARP. (2002). “Off The Charts.” 2001 Tropical Storm Allison Recovery Project. s.l.: *FEMA; HCFCD*.

Topcon Totalcare. (2016). “Topcon Tools Ver. 8.2.3.”

UNAVCO. (2013). “GPS Data - Data Archive Interface Version 2.” https://facility.unavco.org/data/dai2/dai2.html Last modified: Tuesday, 05-Nov-2013 17:04:04 UTC, http://www.unavco.org/data/gps-gnss/data-access-methods/dai2/app/dai2.html Accessed Apr 6, 2016.

USGS. (2014). “USGS groundwater watch.” http://groundwaterwatch.usgs.gov (Dec. 1, 2014).

Van Siclen DC. (1961). "Geologic Framework of Gulf Coastal Plain of Texas." *Houston Geol Soc*: 18–20.

Van Siclen DC. (1968). "The Houston Fault Problem." *Am Ins of Prof Geologists, Texas Sect*. Dallas, TX.

Wang G. (2013). “Teaching High-Accuracy Global Positioning System to Undergraduates Using Online Processing Services.” National Association of Geoscience Teachers. *J of Geosci Edu 61:* 202–212.

Wang G, Kearns TJ, Yu J, Saenz G. (2013). “A stable reference frame for landslide monitoring using GPS in the Puerto Rico and Virgin Islands region.” *Landslides: J of the Int Consortium on Landslides*.

Wang G and Soler T. (2013). “Using OPUS for Measuring Vertical Displacements in Houston, Texas.” *Am Soc of Civ Eng*.

Wang G, Yu J, Kearns TJ, Ortega J. (2014). “Assessing the Accuracy of Long-Term Subsidence Derived from Borehole Extensometer Data Using GPS Observations: Case Study in Houston, Texas.” *Am Soc of Civ Eng*.

Wang G and Soler T. (2014). “Measuring Land Subsidence Using GPS: Ellipsoid Height versus Orthometric Height.” *Am Soc of Civ Engs*.

Wang G, Welch J, Kearns TJ, Yang L, Serna J Jr. (2015). “Introduction to GPS geodetic infrastructure for land subsidence monitoring in Houston, Texas, USA.” Gottingen: Copernicus GmbH. Proceedings of the International Association of Hydrological Sciences 372: 297-303.

Waters JA, McFarland PW, Lea JW. (1955). "Geologic Framework of Gulf Coastal Plain of Texas." *J of Sedi Res, 39(5):* 1821–1850.

Wesselman JB. (1972). "Ground-water resources of Fort Bend County, Texas." *Texas Water Dev Board Rep 155*.

Winker CD. (1982). "Cenozoic Shelf Margins, Northwestern Gulf of Mexico." *Gulf Coast Assoc of Geol Socs Transactions, 32:* 427448 .

Yang L, Wang G, Bao Y, Kearns TJ, Yu J. (2015). “Comparisons of Ground-Based and Building-Based CORS: A Case Study in the Region of Puerto Rico

and the Virgin Islands." ISSN (print): 0733-9453, ISSN (online): 1943-5428, Publisher: *Am Soc of Civ Eng*.

Yu J, Wang G, Kearns TJ, Yang L. (2014). "Is There Deep-Seated Subsidence in the Houston-Galveston Area?" Hindawi Publishing Corporation, *Int J of Geophys, Vol 2014*, Article ID: 942834: 11. http://dx.doi.org/10.1155/2014/942834

Zumberge J, Heflin M, Jefferson D, Watkins M, Webb F. (1997). "Precise point positioning for the efficient and robust analysis of GPS data from large networks." *J Geophys Res 102*: 5005–5017.